

**UCSF**

**UC San Francisco Electronic Theses and Dissertations**

**Title**

Roles of Mafb and c-Maf in MGE-derived cortical interneuron development and maturation

**Permalink**

<https://escholarship.org/uc/item/1f66d86v>

**Author**

Pai, Ling-Lin

**Publication Date**

2019

**Supplemental Material**

<https://escholarship.org/uc/item/1f66d86v#supplemental>

Peer reviewed|Thesis/dissertation

Roles of Mafb and c-Maf in MGE-derived cortical interneuron development and maturation

by  
Ling-Lin Pai

DISSERTATION

Submitted in partial satisfaction of the requirements for degree of  
DOCTOR OF PHILOSOPHY

in

Neuroscience

in the

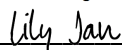
GRADUATE DIVISION

of the

UNIVERSITY OF CALIFORNIA, SAN FRANCISCO

Approved:

DocuSigned by:



Lily Jan

394456D87457494...

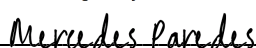
Chair

DocuSigned by:



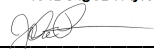
Sam Pleasure

DocuSigned by:



Mercedes Paredes

DocuSigned by:



John Rubenstein

44A19A16E413450...

Committee Members

Copyright 2019

by

Ling-Lin Pai

## **Acknowledgements**

I'm extremely grateful to my advisor, Dr. John Rubenstein, for his mentorship throughout my PhD training. He acknowledges my medical background and understands that clinical medicine to basic research could be a sharp turn, hard transition for me. He patiently taught me how to think and solve problems as a scientist, and helped guiding my project toward publications. Working with John, who is a world well-known developmental neurobiologist, was indeed an invaluable experience.

I thank my committee members, Dr. Sam Pleasure for his encouragement and advice that helps me to not give up on my PhD, Dr. Lily Jan for her kind and supportive insights for my project and for the support when I was struggling for a work-life balance as a new mother, and Dr. Benjamin Cheyette for his positive attitudes and guidance toward my PhD completion, although Ben left UCSF in the middle of my training. I also would like to thank two close mentors in UCSF, Dr. Mercedes Paredes and Dr. Xin Duan. Dr. Paredes and Dr. Duan support me during times when I was doubting my capabilities and when I was frustrated about my scientific progress. They reinforce my confidence and entrust my abilities by granting direct lab collaborations with me. I enjoy working with their labs and see their ways to building successful labs as my goal and fuel to keep fighting.

I am indebted to my mentors from the east coast, Dr. Valina Dawson, Dr. Ted Dawson and Dr. King-Wai Yau. Without their inspiration, encouragement and recommendation letters, finishing a PhD at prestigious UCSF Neuroscience program would never come true.

During my training, I was very lucky to be mentored by an incredible postdoc, Dr. Daniel Vogt. Daniel was always there for me, ups and downs, and whenever I had questions and stupid ideas. I was very happy and sad at the same time when Daniel took on his new assistant professorship in Michigan around 2 years ago, but even when Daniel is physically in Michigan, he calls in periodically to make sure I am still on the right track for PhD completion both scientifically and mentally. I owe this PhD achievement to Daniel in many ways and he will forever be a mentor to me.



Thank you, Jia Sheng Hu, Siavash Fazel Darbandi, Carol Kim, Ramon Pla and Magnus Sandberg, for your help, encouragement, generous insights and contributions to my *Maf* project. I specifically want to thank Carol for being such a loving lab mother to me. She helps making sure I get all the correct supplies and that my mice are well taken care of for my experiments. She cares for me so much as a friend and as a mother when I was facing frustration from work and during times when I was pregnant and suffering from physical discomforts. Without Carol, I could not have gotten this far.

Thank you, Dr. Jeanne Paz, Dr. Tomasz Nowakowski, Dr. Anirban Paul, Dr. Lisa Goodrich and Dr. Jin Chen for your electrophysiology work, computational analyses on single-cell RNA-sequencing data and precious *Maf* mouse lines. Your fabulous collaborative work helped turning my thesis into great scientific publications.

Lastly, I want to thank my family for their unconditional love and support before and during my PhD training. My mother, Su-Ching, is not traditional. She was never disappointed when I told her I decided to give up medicine and pursue science. She understands the importance of scientific advancement and fully supports my mission. She gives up her retirement and fly half the world over to help taking care of my baby, so I can be 100% focused on my research work. My husband, Jason, is not an enthusiast of basic research, but he supports me in every way to power me through the PhD training with his love and optimism. My son, Maxwell, is my medicine. Despite hard times taking care of a baby and doing PhD at the same time, both physically and financially, his happiness and giggly laughs are my best medicine to leading a hopeful life.

## **Contributions**

The majority of this thesis is a reproduction of my recently published material and contains contributions from collaborators. Pai ELL, Vogt D, Clemente-Perez, McKinsey GL, Cho FS, Hu JS, Wimer M, Paul A, Fazel Darbandi S, Pla R, Nowakowski TJ, Goodrich LV, Paz JT and Rubenstein JLR. (2019). Mafb and c-Maf have prenatal compensatory and postnatal antagonistic roles in cortical interneuron fate and function. Cell Reports, 26(5), 1157-1173.

Daniel and I contributed to all the immunostaining, fate-mapping and birthdating experiments. I contributed to all the *in vitro* culture work and helped generated all the animals needed for electrophysiology collaborations.

## **Abstract**

### **Roles of *Mafb* and *c-Maf* in MGE-derived cortical interneuron development and maturation**

**Ling-Lin Pai**

An imbalance of excitation and inhibition in key neural circuits is hypothesized to underlie some epileptic disorders and neuropsychiatric diseases, such as schizophrenia and autism spectrum disorder (ASD) (Lim et al., 2018a; Rubenstein and Merzenich, 2003; Sohal and Rubenstein, 2019; Yizhar et al., 2011). Inhibition in the cortex is primarily generated by cortical interneurons (CINs). CINs are produced by the medial and caudal ganglionic eminences (MGE and CGE). 70% of CINs are MGE-derived and primarily express Parvalbumin (PV<sup>+</sup>) or Somatostatin (SST<sup>+</sup>). CINs become postmitotic in the MGE, then tangentially migrate to the cortex, where they mature and integrate into local cortical circuits (Lim et al., 2018a). Great gaps remain in our understanding of the cellular and molecular mechanisms regulating CIN generation, migration and maturation.

My thesis work is to focus on elucidating the function of *Mafb* and *c-Maf* in MGE-lineage CIN development and maturation. Using conditional *Maf* knockout animal models together with immunohistochemistry, *in vitro* primary neuronal culture, *in vivo* MGE transplantation assay, electrophysiology and single-cell RNA-sequencing techniques, we profiled the expression pattern of *Mafb* and *c-Maf* (Chapter 2), and identified that *Mafb* and *c-Maf* function together prenatally in the MGE to control SST<sup>+</sup> CIN neurogenesis (Chapter 3), while postnatally they function antagonistically in the CINs to control CIN synaptogenesis, morphogenesis and firing properties (Chapter 4). On-going pursuit is to try to figure out the molecular mechanism that is downstream of *Mafb* and *c-Maf* to lead to the phenotypes we have observed in the conditional mutants (Chapter 6).

## Table of Contents

<b>Chapter 1. Introduction and Background.....</b>	<b>1</b>
<b>Chapter 2. Elucidation of <i>Mafb</i> and <i>c-Maf</i> expression patterns in developing and mature CINs....</b>	<b>4</b>
2A. Prenatal and perinatal expression of <i>Mafb</i> and <i>c-Maf</i> in the MGE and its lineage.....	4
2B. Postnatal expression of <i>Mafb</i> and <i>c-Maf</i> in the mature CINs.....	6
2C. Validation of <i>Mafb</i> and <i>c-Maf</i> expression pattern using histochemistry.....	7
<b>Chapter 3. <i>Mafb</i> and <i>c-Maf</i> function synergically to control MGE CIN neurogenesis.....</b>	<b>10</b>
3A. Combined loss of <i>Mafb</i> and <i>c-Maf</i> results in decreased MGE-derived CINs.....	10
3B. Cell autonomous role for <i>Mafb</i> and <i>c-Maf</i> in establishing normal numbers of PV <sup>+</sup> MGE-lineage.....	13
CINs.....	13
3C. cDKOs have reduced CINs and excess hippocampal interneurons at P0.....	14
3D. MGE proliferation and CIN apoptosis are not altered in cDKOs.....	17
3E. Early born MGE lineages are over represented in cDKO adult brains.....	20
3F. Excessive production of SST <sup>+</sup> CINs in cDKOs.....	22
3G. <i>Mafb</i> and <i>c-Maf</i> function in SVZ progenitors to control MGE-derived CIN production.....	26
3H. <i>c-Maf</i> controls CIN migration alone and together with <i>Mafb</i> .....	29
<b>Chapter 4. Postnatal function of <i>Mafb</i> and <i>c-Maf</i> in CIN action potential firing properties, ..... synaptic excitation and cortical excitability.....</b>	<b>32</b>
4A. Active and passive membrane properties of CINs in the controls and <i>Maf</i> mutants.....	32
4B. Excitatory synaptic properties onto CINs from the controls and <i>Maf</i> mutants.....	33
4C. <i>c-Maf</i> cKO CINs had an increased density of excitatory synapses and increased neurite complexity... <i>in vitro</i> .....	36
4D. Slice local field potential analyses showed that <i>Mafb</i> cKOs had increased neo-cortical circuit..... excitability unlike the <i>c-Maf</i> cKO and cDKOs.....	38
<b>Chapter 5. Discussion of main findings .....</b>	<b>41</b>
5A. <i>Mafb</i> and <i>c-Maf</i> control MGE CIN numbers .....	41

5B. <i>Mafb</i> and <i>c-Maf</i> provide a brake on neural differentiation .....	42
5C. <i>Mafb</i> and <i>c-Maf</i> repress SST CIN fate .....	42
5D. <i>Mafb</i> and <i>c-Maf</i> functions begin in SVZ2 of the MGE to control CIN fate.....	42
5E. Interneurons in <i>Maf</i> mutants show laminar and regional mislocalization.....	43
5F. <i>Mafb</i> and <i>c-Maf</i> have distinct roles in regulating fast-spiking CINs and neocortical circuit.....	
Function postnatally.....	44
<b>Chapter 6. Molecular mechanism downstream of <i>Mafb</i> and <i>c-Maf</i> regulation in MGE-lineage.....</b>	
<b>CIN development and maturation.....</b>	<b>47</b>

## List of Figures

Figure 1.1: MAFB and c-MAF protein expression pattern over time.....	2
Figure 2.1: Analysis of <i>Mafb</i> and <i>c-Maf</i> expression in single cells from the MGE and in MGE-derived..... developing CINs.....	5
Figure 2.2: Analysis of <i>Mafb</i> and <i>c-Maf</i> expression in single cells from P40 mature CINs.....	6
Figure 2.3: Analysis of <i>Mafb</i> and <i>c-Maf</i> expression in tissue sections from the MGE and in..... MGE-derived developing CINs.....	8
Figure 2.4: Analysis of <i>Mafb</i> and <i>c-Maf</i> RNA expression and the effect of <i>Maf</i> mutations on the..... expression of <i>Mafb</i> and <i>c-Maf</i> at E15.5.....	9
Figure 3.1: CINs in <i>Maf</i> cDKOs are reduced in numbers, have altered laminar positions and a ..... preferential loss of PV <sup>+</sup> subtype.....	12
Figure 3.2: CINs in <i>Maf</i> cDKOs cell autonomously have a decreased proportion of PV <sup>+</sup> CINs.....	13
Figure 3.3: <i>Mafb</i> / <i>c-Maf</i> cKO and cDKOs have gradual reduction of CINs by P35.....	15
Figure 3.4: Effect of <i>Maf</i> single and double conditional mutants ( <i>Nkx2.1-Cre</i> ) on the numbers of..... hippocampal tdTomato <sup>+</sup> interneurons at P0.....	16
Figure 3.5: MGE progenitors show no differences in proliferation indices in <i>Maf</i> cDKOs.....	18
Figure 3.6: Microglia does not account for the loss of CIN in <i>Maf</i> cDKO.....	19
Figure 3.7: EdU pulse chase experiments revealed that <i>Maf</i> cDKOs have increased early-born adult..... CINs and have precocious MGE neurogenesis.....	21
Figure 3.8: <i>Mafb</i> and <i>c-Maf</i> regulate the quantity and position (laminar and regional) of MGE-derived..... <i>somatostatin</i> <sup>+</sup> interneurons during cortical and hippocampal development.....	23
Figure 3.9: Increased numbers of SST <sup>+</sup> interneurons in developing (E15.5) cDKO neocortex.....	24
Figure 3.10: Increased numbers of SST <sup>+</sup> interneurons in developing (P0) cDKO neocortex.....	25
Figure 3.11: Schema showing where each Cre line initiates recombination.....	26
Figure 3.12: 799- <i>CreER</i> activity initiates in the late SVZ (SVZ2) of MGE.....	27
Figure 3.13: Fate mapping of <i>Sst-IRES-Cre</i> lineage CINs in the adult CINs.....	28

Figure 3.14: <i>Sst-IRES-Cre</i> generated cDKOs does not have CIN loss phenotype (unpublished).....	28
Figure 3.15: Effect of <i>Maf</i> single and double conditional mutants ( <i>Nkx2.1-Cre</i> ) on the expression of <i>Sst</i> ... RNA at E15.5.....	29
Figure 3.16: <i>In situ</i> hybridization for genes that regulate MGE and CIN development.....	31
Figure 4.1: Synaptic excitation and intrinsic excitability of Fast Spiking (FS) CINs in <i>Mafb</i> cKO, ..... <i>c-Maf</i> cKO and cDKO mice.....	34
Figure 4.2: (A-C) Synaptic excitation and intrinsic excitability of RS CINs in control, <i>Mafb</i> cKO,..... <i>c-Maf</i> ... cKO and cDKO mice. (D-H) Neurite complexity analysis on CINs from control, <i>Mafb</i> cKO,..... <i>c-Maf</i> cKO... and cDKO following 14 days of <i>in vitro</i> cortical culture.....	35
Figure 4.3: Excitatory synapse quantification and morphology analysis of <i>Nkx2.1-cre</i> -lineage CINs..... from <i>Mafb</i> cKO, <i>c-Maf</i> cKO and cDKO.....	37
Figure 4.4: Local Field Potentials (LFPs) and current source densities (CSDs) for neocortical slices..... illustrate cortical hyper-excitability in <i>Mafb</i> cKOs but not in <i>c-Maf</i> cKOs or DKO mice.....	39
Figure 5.1: Models of <i>Mafb/c-Maf</i> function in MGE CIN cell type specification and dendritic/ synaptic.... function maturation.....	46
Figure 6.1: Single-Cell RNA-seq analysis of P0 WT and cDKO neocortex.....	48
Figure 6.2: Representative differentially expressed genes in the cDKO.....	49
Figure 6.3: <i>Maf</i> cDKO has decreased expression of <i>Mef2c</i> and increased expression of <i>Sst</i> .....	51
Figure 6.4: <i>Maf</i> cDKO neurite outgrowth defect can be rescued by expression of <i>Mef2c</i> and <i>Snap25</i> .....	52

## List of Tables

Table S1: Genetic markers for single cell clusters .....	70
Table S2: Cumulative cell counts of <i>Nkx2.1-cre</i> -lineage cells in the neocortex and hippocampus .....	70
Table S3: Passive and active electric membrane properties of layer V CINs.....	72
Table S4: Properties of spontaneous excitatory post-synaptic currents (sEPSCs) of layer V CINs for all.... groups and mEPSCs of layer V CINs for control and <i>Mafb</i> cKO.....	73
Table S5: statistical analysis for local field potential measurement by layers.....	74
Table S6: Genotype information regarding the mice used for each Figure and analysis.....	75



## **Appendix**

<b>Appendix I: Methods.....</b>	<b>53</b>
Animal care and breeding.....	53
EdU injections and analysis.....	54
Immunofluorescence/Immunohistochemistry.....	54
RNA in situ hybridization.....	55
Fluorescent in situ hybridization.....	56
MGE transplantation assay.....	56
Primary neuronal culture for analysis of dendritic arborization (Sholl) and synapse using neonatal..... cortex.....	57
Image acquisition and processing .....	58
Single cell RNA-sequencing sample and library preparation.....	58
Processing of sequencing reads/data.....	59
Cell clustering, t-SNE visualization and marker-gene identification.....	59
Electrophysiology.....	60
Quantification and statistical analysis.....	61
 <b>Appendix II: References.....</b>	 <b>63</b>
 <b>Appendix III: Compilation of Supplementary tables .....</b>	 <b>70</b>

## **Chapter 1: Introduction and Background**

Disturbances in cortical development and maturation are thought to underlie some symptoms of neurological and neuropsychiatric disorders such as autism spectrum disorder (ASD), epilepsy and schizophrenia. One mechanism that is postulated to contribute to symptoms is a circuit imbalance in the excitation/inhibition (E/I) ratio (Chao et al., 2010; Han et al., 2012; Rubenstein and Merzenich, 2003b; Yizhar et al., 2011). While the majority of cortical excitation is generated by glutamatergic projection neurons and thalamic afferents, inhibition is largely generated by locally projecting GABAergic CINs. CINs exhibit diverse morphological, connectivity, molecular and electrophysiological properties (Huang et al., 2007; Kepecs and Fishell, 2014; Kessaris et al., 2014), which facilitate E/I balance in distinct cortical microcircuits.

CINs are derived from progenitor zones in the subpallial telencephalon called the medial and caudal ganglionic eminences (MGE and CGE, respectively), and the preoptic area (POA) (Gelman et al., 2011; Wonders and Anderson, 2006). The development of MGE and CGE-derived CINs are coordinated by a combination of TFs expressed in these progenitor zones (Hu et al., 2017; Lim et al., 2018a). Mature CINs express molecular markers that delineate four broad subgroups: MGE-derived SST<sup>+</sup> and PV<sup>+</sup>, and CGE-derived Vasoactive Intestinal Peptide (VIP<sup>+</sup>) and Reelin<sup>+</sup>; SST<sup>-</sup> (Lim et al., 2018a).

*Mafb* and *c-Maf* are part of the large *Maf* TF family, which bind to DNA through basic leucine zipper motif (Kataoka, 2007). *Mafb* and *c-Maf* function alone or together to control cell fate and differentiation in bone, epithelial cells, lens, macrophages and pancreas (Lopez-Pajares et al., 2015; Nishikawa et al., 2010; Soucie et al., 2016). In the nervous system *Mafb* and *c-Maf* have multiple functions. For example, *Mafb* controls embryonic hindbrain regional patterning (Cordes and Barsh, 1994), and promotes the formation of auditory ribbon synapses that are required to activate inner hair cells (Lu et al., 2011; Yu et al., 2013). *c-Maf* is involved in touch receptor differentiation in the peripheral nervous system (Wende et al., 2012).

*Mafb* and *c-Maf* are particularly intriguing in CIN development, as their MGE expression initiates in the MGE subventricular zone (SVZ) and persists in MGE-derived interneurons but not in MGE-derived projection neurons (Fig.1.1) (Cobos et al., 2006; McKinsey et al., 2013; Zhao et al., 2008). In addition, TFs that control MGE CIN development also regulate *Mafb* and *c-Maf* expression. For instance, *Zfhx1b* mutants have reduced *c-Maf* expression, *Lhx6* mutants have reduced *Mafb* expression, and *Dlx1/2* mutants have reduced *Mafb* and *c-Maf* expression (McKinsey et al., 2013; Zhao et al., 2008). Two recent reports provided evidence that (1) *Mafb* is preferentially expressed in a subtype of SST<sup>+</sup> CINs (Martinotti cells) where it regulates their migration and axonal projection (Lim et al., 2018b). (2) *c-Maf* promotes the generation of SST<sup>+</sup> CINs (Lim et al., 2018a; Mi et al., 2018), a finding that is in opposition to the combined functions of *Mafb* and *c-Maf* presented herein.

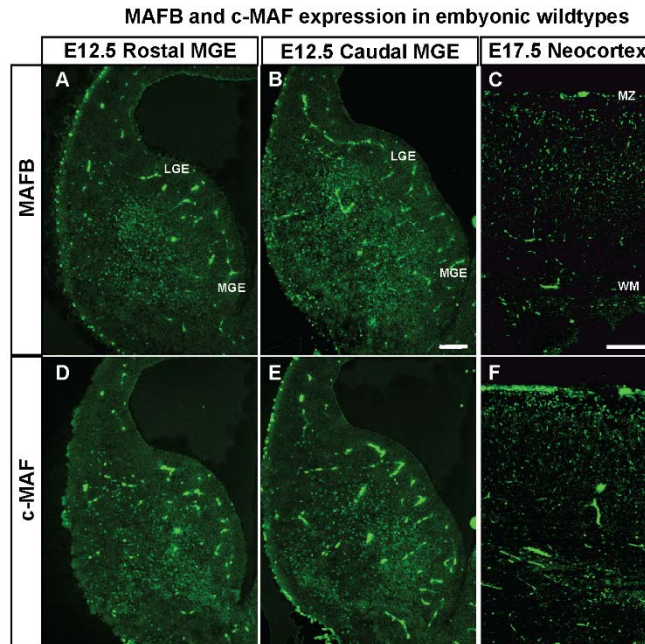


**Figure 1.1. MAFB and c-MAF protein expression pattern over time.** (A-B, D-E) Rostral and caudal expression of MAFB and c-MAF at E12.5 MGE sections. (C, F) MAFB and c-MAF expression in the E17.5 neocortex.

Here we report the individual and combined functions of *Mafb* and *c-Maf* after conditional deletion in the MGE lineages using *Nkx2.1-Cre* and *799-CreER*. *Mafb*; *c-Maf* conditional double knockout (cDKO) phenotypes provided evidence that *Mafb* and *c-Maf* compensate for each other. Notably, cDKOs generate excessive SST<sup>+</sup> at the expense of PV<sup>+</sup> CINs. Furthermore, cDKOs have reduced CIN numbers, probably due to a combination of mechanisms, including ectopic migration to the hippocampus and a progressive reduction in CINs during postnatal ages. However, our electrophysiological analyses of adult somatosensory cortices, and *in vitro* assays of neonatal CINs, provide evidence that *Mafb* and *c-Maf* have distinct postnatal functions in CIN maturation, synaptogenesis, and activity. Together these defects lead to alterations in neocortical circuit excitability and provide potential new mechanisms into how these TFs operate during CIN development and maturation.

## **Chapter 2: Elucidation of *Mafb* and *c-Maf* expression patterns in developing and mature CINs**

### **2A. Prenatal and perinatal expression of *Mafb* and *c-Maf* in the MGE and its lineage**

We compared *Mafb* and *c-Maf* gene expression in the MGE and at later stages of CIN maturation. First, we determined *Mafb* and *c-Maf* gene expression profiles and their cellular specificity in the MGE by reanalyzing single cell RNA-seq data derived from wildtype (WT) E11.5, E13.5 and E15.5 MGE tissue (Chen et al., 2017). We studied the dataset using Louvain clustering with Jaccard distance matrix, which revealed nine molecularly distinct clusters (Fig. 2.1A, 2.1B, Table S1)(Shekhar et al., 2016). *Mafb* and *c-Maf* were expressed in some MGE progenitor cells (clusters 1, 8 and 9; Table S1). In addition, *Mafb* and *c-Maf* mRNA were co-expressed in a subset of these progenitors. *Mafb* and *c-Maf* were significantly enriched in cluster “4”, which we propose corresponds to cells that will become CINs, based on their expression of multiple genes, including *Cux2* and *ErbB4* (Fig. 2.1C). The expression levels of *Mafb* and *c-Maf* in cluster “4” showed that these genes were largely co-expressed in immature CINs. Thus, *Mafb* and *c-Maf* expression initiates in progenitors and their co-expression increases in immature CINs (Fig. 2.1C).

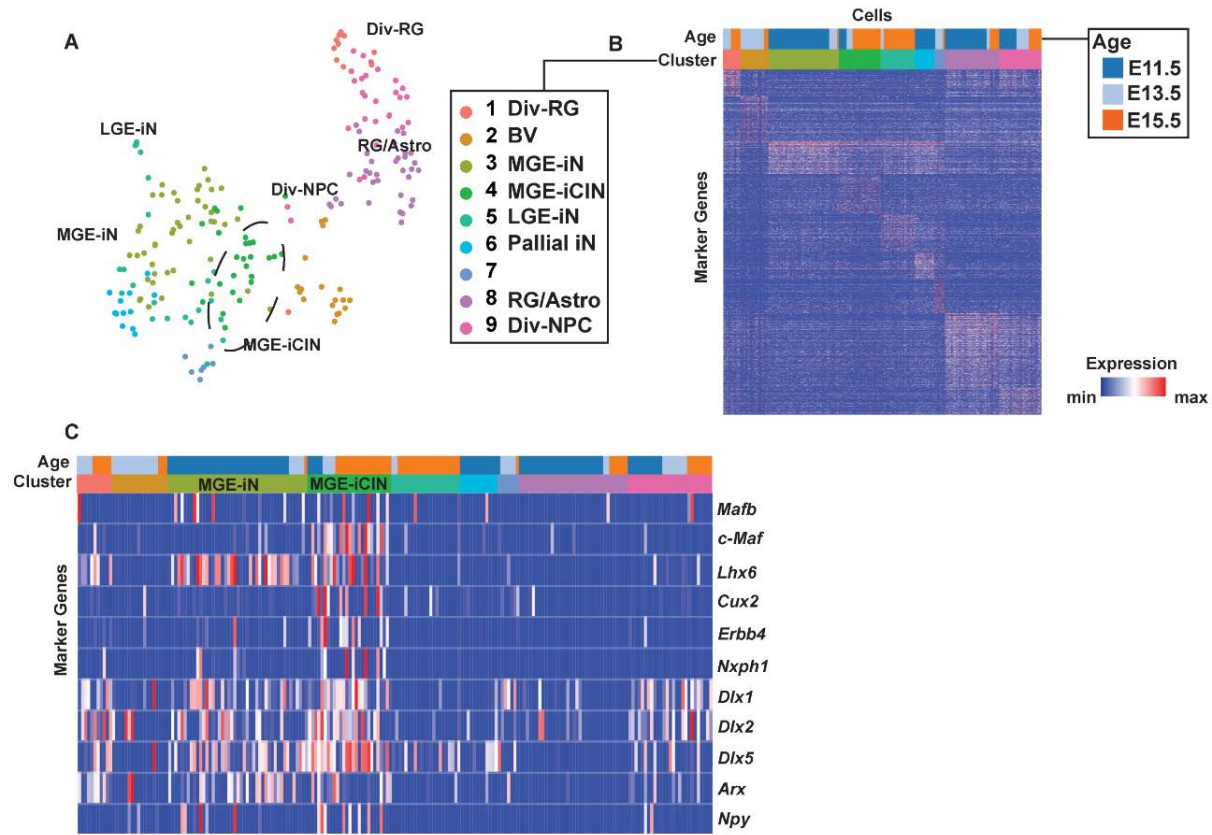


**Figure 2.1 Analysis of *Mafb* and *c-Maf* expression in single cells from the MGE and in MGE-derived developing CINs.** (A) T-stochastic neighbor embedding (t-SNE) plot representing MGE cells analyzed from age E11.5, E13.5 and E15.5, and colored by their cluster assignments. Cells with properties of MGE-derived immature CINs (iCIN) are encircled in cluster “4”. (B) Heatmap representation of cluster marker genes. Please see Table S1 for the gene list. (C) Heatmap representation of the 9 clusters; it shows enrichment of *Mafb* and *c-Maf* in cluster 4, and the expression of markers for MGE-derived CINs. Note that half of the cluster 4 CINs co-express *Mafb* and *c-Maf*. Expression feature plot of *Maf*. Abbreviations: Div-RG: dividing radial glia; MGE-iN/iCIN: MGE-derived immature neurons/cortical interneurons; LGE-iN: LGE-derived immature neurons; Pallial iN: pallial immature neurons; RG/Astro: radial glia and astrocytes; Div-NPC: dividing neural progenitor cells

## 2B. Postnatal expression of *Mafb* and *c-Maf* in the mature CINs

We then assessed single cell transcriptome data from postnatal day 40 (P40) CINs (Paul et al., 2017). These data showed that *Mafb* and *c-Maf* expression persisted in MGE-derived adult CINs. *Mafb* and *c-Maf* were enriched in multiple MGE-derived CIN subtypes, including chandelier cells (CHC), PV<sup>+</sup> basket cells (PVBC), SST; nNOS<sup>+</sup> cells (SST; NOS) and SST; CALRETININ<sup>+</sup> (SST;CR) cells. Importantly, these two TFs are highly expressed in the SST;CR subpopulation (Fig. 2.2A, 2.2B), suggesting that the broad SST<sup>+</sup> group of CINs was determined by these TFs. Moreover, it indicated that *c-Maf*, but not *Mafb* mRNA was detected in VIP<sup>+</sup> CINs (CGE-derived), suggesting a divergence of *Maf* expression into other CIN progenitor domains.

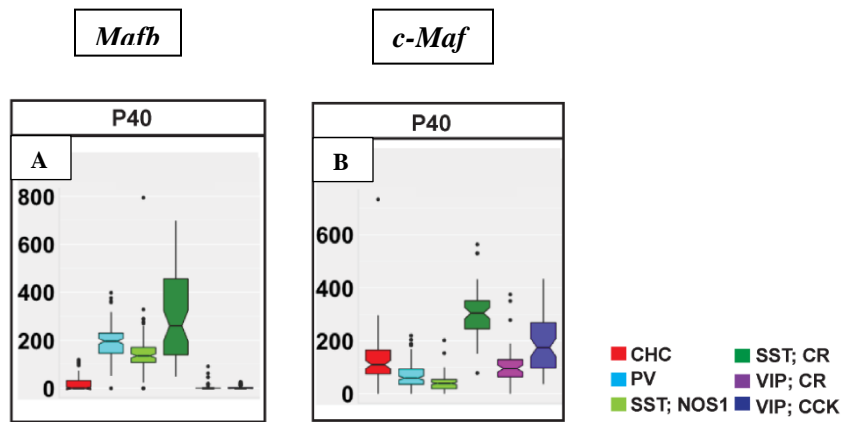


**Figure 2.2 Analysis of *Mafb* and *c-Maf* expression in single cells from P40 mature CINs.** Boxplots of *Mafb* (A) and *c-Maf* (B) expression in CIN subtypes at P40. Abbreviations: CHC: chandelier cells; CR: Calretinin; VIP: vasoactive intestinal peptide

## 2C. Validation of *Mafb* and *c-Maf* expression pattern using histochemistry

To complement the single cell transcriptome analysis data, we performed histochemistry to study *Mafb* and *c-Maf* RNA and protein expression (Fig. 2.3-2.4). Consistent with the single cell RNA-seq data, we found that MAFB and c-MAF proteins expressed in the MGE SVZ and in MGE-derived immature CINs (SVZ: Fig. 2.3A, 2.3C, 2.3H; CINs: Fig. 2.3J-2.3L). In the MGE SVZ, MAFB and c-MAF were expressed in KI67<sup>+</sup> SVZ2 progenitors (Fig. 2.3H). The SVZ2 is the layer of SVZ progenitors that are between the SVZ1 (adjacent to the VZ) and the layer of new-born neurons. (Petryniak et al., 2007).

CINs tangentially migrate to the cortex along multiple pathways. We explored whether MAFB<sup>+</sup> and c-MAF<sup>+</sup> CINs had shared or different trajectories. Immunofluorescence analyses of E15.5 WT neocortices showed that MAFB was expressed in immature CINs migrating along the marginal zone (MZ) pathway and in the cortical plate (CP) (Fig. 2.3I-2.3J) as described in Lim et al., 2018. On the other hand, c-MAF expression was enriched in the deep migratory pathway (Fig. 2.3K-2.3L). This suggests that MAFB and c-MAF may differentially regulate CINs migrating along the superficial and deep pathways, respectively.



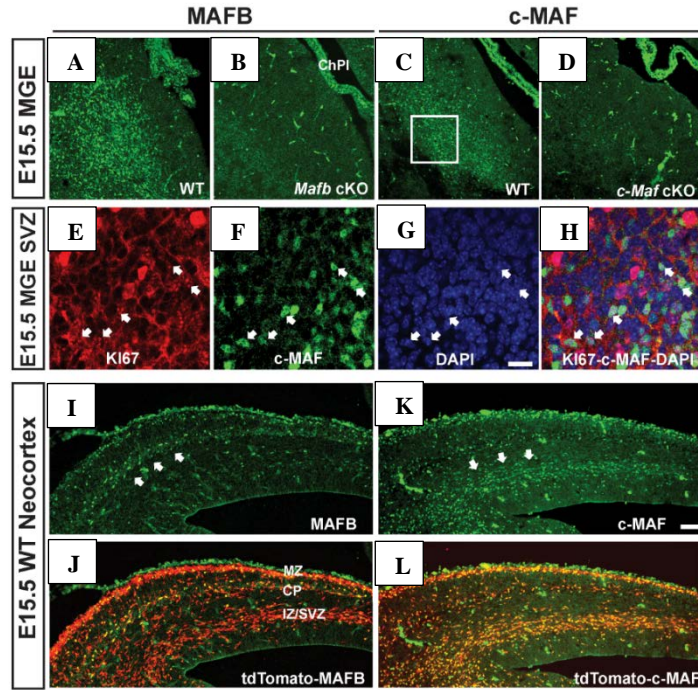


**Figure 2.3 Analysis of *Mafb* and *c-Maf* expression in tissue sections from the MGE and in MGE-derived developing CINs.** (A-B) Immunofluorescent images of the MGE from E15.5 WT and *Mafb* cKO that show MAFB expression. (C-D) Immunofluorescent images of the MGE from E15.5 WT and *c-Maf* cKO that show c-MAF expression. (E-H) Confocal imaging that shows co-labeling of KI67 and c-MAF in the MGE SVZ (boxed in (C)). Arrowheads point to cells that are c-MAF<sup>+</sup> progenitors. Immunofluorescent images from E15.5 WT neocortex that show *Nkx2.1-cre* mediated tdTomato expression merged with MAFB (I-J) and c-MAF (K-L). Scale bar in (G) and (K) = 100um. Abbreviations: ChPl: Choroid Plexus; MZ: marginal zone; CP: cortical plate; IZ/SVZ: intermediate zone/subventricular zone.

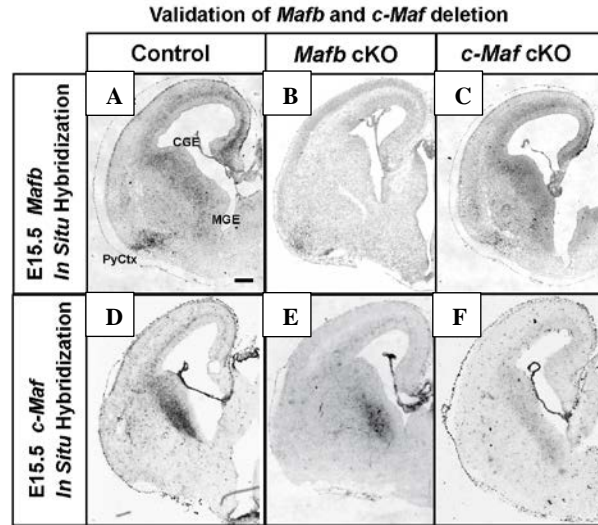


**Figure 2.4 Analysis of *Mafb* and *c-Maf* RNA expression and the Effect of *Maf* mutations on the expression of *Mafb* and *c-Maf* at E15.5.** (A,D) *Mafb* and *c-Maf* expression in E15.5 WT tissue sections. (B-C, E-F) Effect of *Mafb* and *c-Maf* deletion on RNA expression in the *Mafb* cKO/*c-Maf* cKOs at E15.5, compared to control brain.

### **Chapter 3: *Mafb* and *c-Maf* function synergically to control MGE CIN neurogenesis**

#### **3A. Combined loss of *Mafb* and *c-Maf* results in decreased MGE-derived CINs**

The functions of *Mafb* and *c-Maf* in CIN development largely remain unknown, in part because constitutive *Mafb* and *c-Maf* mutant mice die at embryonic or neonatal ages (Blanchi et al., 2003; Kawauchi et al., 1999). Thus, to examine the prenatal and postnatal functions of these TFs in MGE-derived CINs, we generated conditional mutant mice using floxed *Mafb* and *c-Maf* (Wende et al., 2012; Yu et al., 2013), combined with *Nkx2.1-Cre* (Xu et al., 2008) alleles, whose expression in the MGE and POA begins ~embryonic day (E) 9.5. We crossed either *Mafb*<sup>Flox</sup> and/or *c-Maf*<sup>Flox</sup> mice to those harboring *Nkx2.1-Cre* and the *Ai14* allele (Madisen et al., 2010), which expresses the fluorescent protein tdTomato after CRE recombination, and subsequently generated both conditional *Mafb* and *c-Maf* single (cKOs) as well as double knockouts (cDKOs). Mice were born at expected Mendelian ratios and lived into adulthood. Of note, these crosses generated both WT and conditional heterozygous states for each genotype (see details in methods). We did not detect gross phenotypes between WT and conditional heterozygous mice. Thus, controls used in this report are either WT or mixed conditional heterozygotes unless otherwise noted.

We began our phenotypic analysis of *Maf* mutant mice by assessing MGE-derived CINs and CIN subgroups from *Nkx2.1-Cre*-lineages (tdTomato<sup>+</sup>) at P35 in the somatosensory cortex (Fig. 3.1). *Mafb* and *c-Maf* cKOs had modest decreases of 25% and 32%, respectively, in tdTomato<sup>+</sup> cells (Fig. 3.1A-3.1C, 3.1E-3.1G, 3.1J, *Mafb* cKOs p= 0.002, *c-Maf* cKOs p = 0.0002). On the other hand, *Maf* cDKOs had a 64% reduction in the density of tdTomato<sup>+</sup> cells (Fig. 3.1D, 3.1H, 3.1J, p < 0.0001). These results suggest that *Mafb* and *c-Maf* have compensatory roles in regulating the number of MGE-derived CINs.

Next, we assessed the proportion of cells that occupied each lamina of the somatosensory cortex. *Mafb* and *c-Maf* cKOs did not differ from controls, whereas the cDKOs had a greater loss in upper lamina (layers II-IV) and an increased proportion in deep lamina (layer VI) (Fig. 3.1I, layers ii/iii p= 0.03, layer

iv  $p < 0.0001$ , layer vi  $p < 0.0001$ ), even though tdTomato<sup>+</sup> cell densities were reduced in all layers (Fig. 3.1J). Interestingly, in the cDKOs MGE-derived CINs were also found in layer I, a lamina that is not populated by these cells (Fig. 3.1I,  $p < 0.0001$ ).

To determine if loss of *Mafb* and *c-Maf* affected MGE lineage CINs equally, we determined the proportion of remaining tdTomato<sup>+</sup> cells in the mutants that expressed either SST or PV. While the density of tdTomato<sup>+</sup>;SST<sup>+</sup> CINs decreased in all KOs (Fig. 3.1A-3.1D, Table S2), the proportion of SST<sup>+</sup> CINs was similar between genotypes (Fig. 3.1J, 3.1K). Furthermore, the density of tdTomato<sup>+</sup>;PV<sup>+</sup> CINs decreased in all KOs (Fig. 3.1E-3.1H, Table S2); however, the proportion of tdTomato<sup>+</sup> cells expressing PV was reduced 2-fold only in the cDKO (Fig. 3.1J, 3.1L,  $p < 0.0001$ ). This disproportionate decrease in PV<sup>+</sup> CINs led to an increase in the ratio of SST to PV CINs in the cortex in cDKOs (Fig. 3.1M). Of note, interneurons in the hippocampus and striatum also exhibited similar disproportionate decreases in the PV<sup>+</sup> cells (Table S2).

In sum, *Mafb* and *c-Maf* together are required for controlling the appropriate number of MGE-derived CINs at P35. Furthermore, they are particularly important in promoting PV<sup>+</sup> cortical, hippocampal and striatal interneuron generation and/or maturation.

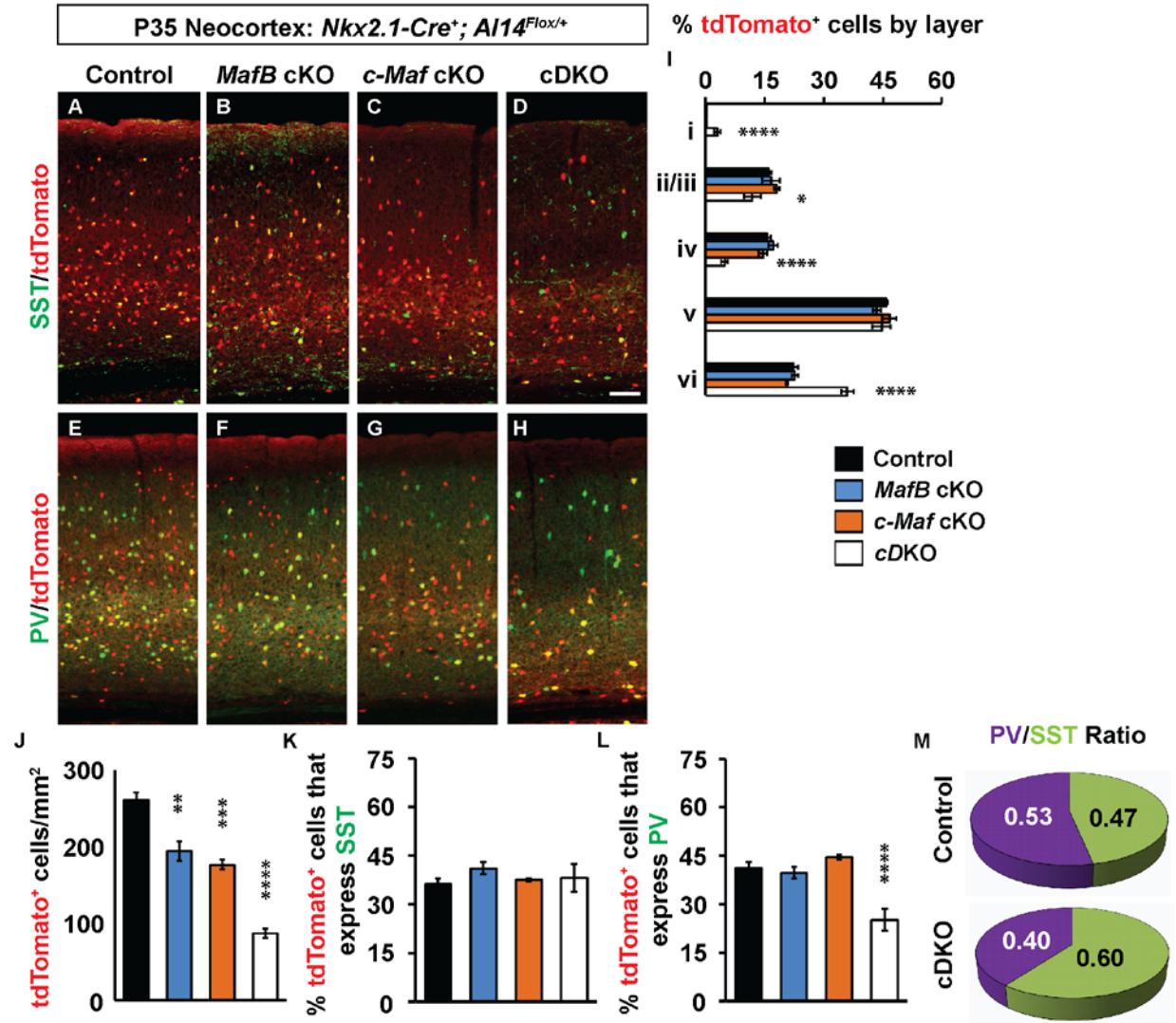


**Figure 3.1 CINs in *Maf* cDKOs are reduced in numbers, have altered laminar positions and a preferential loss of PV<sup>+</sup> subtype.** Immunofluorescent images from P35 somatosensory cortices show native tdTomato merged with either somatostatin (SST) (A-D) or parvalbumin (PV) (E-H). (I) Quantification of the relative proportion of tdTomato cells that occupy cortical layers. (J) Quantification of the number of tdTomato<sup>+</sup> cells per mm<sup>2</sup> in the somatosensory cortex. Quantification of the proportion of tdTomato<sup>+</sup> cells that co-express either SST (K) or PV (L). (M) Pie chart of PV<sup>+</sup>/SST<sup>+</sup> ratio of the remaining tdTomato<sup>+</sup> cells. (n) = 4 for all groups. Scale bar in (D) = 100  $\mu$ m. Data are expressed as the mean  $\pm$  SEM. \*p < 0.05, \*\*p < 0.01, \*\*\*p < 0.001, \*\*\*\*p < 0.0001.

### 3B. Cell autonomous role for *Mafb* and *c-Maf* in establishing normal numbers of PV<sup>+</sup> MGE-lineage CINs

To test whether the preferential reduction of PV<sup>+</sup> cells in the *Maf* cDKOs was cell autonomous, we used an MGE transplantation assay to transduce small numbers of MGE progenitor cells into a WT cortex and monitor their development *in vivo* (Vogt et al., 2015). E13.5 *Ai14<sup>Flox/+</sup>* MGE cells, that were either WT, *Mafb<sup>Flox/Flox</sup>*, *c-Maf<sup>Flox/Flox</sup>*, or *Mafb<sup>Flox/Flox</sup>; c-Maf<sup>Flox/Flox</sup>* were harvested and virally transduced with a *Cre* expression vector using the *Dlx112b* enhancer. These MGE cells were transplanted into P1 WT neocortices; 40 days later they were analyzed for SST, PV, nNOS, VIP and SP8 expression.

The proportion of tdTomato<sup>+</sup> cells that were PV<sup>+</sup> were decreased in all *Maf* mutant cells (Fig. 3.2O, *Mafb* cKOs: 45% p = 0.04, *c-Maf* cKOs: 50%, p = 0.02, cDKOs: 65%, p = 0.006). SST numbers were not changed except for *Mafb* cKO (increased 14%; Fig. 3.2N, p = 0.04). Other MGE-derived CINs such as nNOS<sup>+</sup> cells (Fig. 3.2P) and CGE-derived CINs, VIP<sup>+</sup> and SP8<sup>+</sup>, were unchanged (Fig. 3.2Q-3.2R). These data suggest that the decrease in PV<sup>+</sup> MGE-lineage CINs is cell autonomous and that loss of *Mafs* does not lead to CIN fate change from MGE-type (SST, PV) to CGE-type (SP8, VIP).

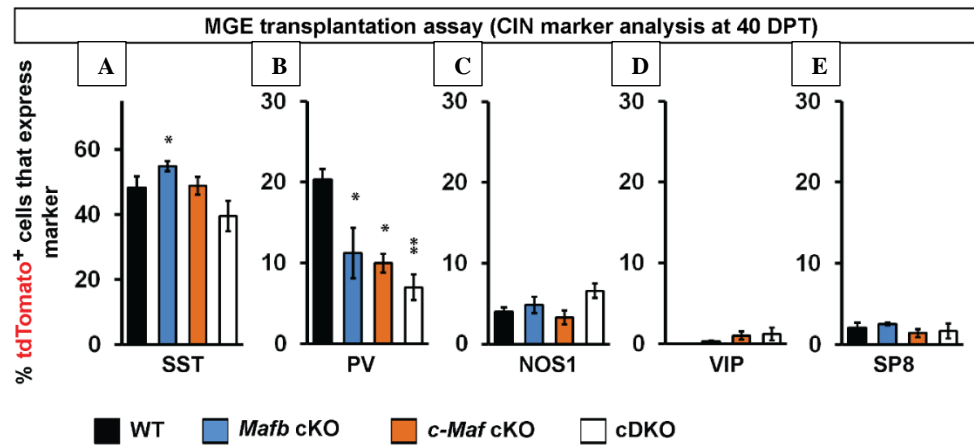


**Figure 3.2. CINs in *Maf* cDKOs cell autonomously have a decreased proportion of PV<sup>+</sup> CINs. (A-E)** MGE cell transplantation into neocortex assay to assess cell autonomy of CIN phenotypes. Quantification of the number of transplanted tdTomato<sup>+</sup> cells per mm<sup>2</sup> that co-express MGE or CGE CIN markers including SST, PV, nNOS, VIP and SP8. (n) = 4 for all groups. Data are expressed as the mean ± SEM. \*p < 0.05, \*\*p < 0.01, \*\*\*p < 0.001, \*\*\*\*p < 0.0001.

### **3C. cDKOs have reduced CINs and excess hippocampal interneurons at P0**

To identify the onset in the reduction of MGE-lineage CINs observed in cDKOs (Fig. 3.1), we assessed tdTomato<sup>+</sup> cells at multiple ages (Fig. 3.3). At E13.5 and E15.5 we found no significant changes in the density of tdTomato<sup>+</sup> neocortical cells (Fig. 3.3A-3.3H, 3.3W). By P0, the cDKOs had a decrease (~26%) in the density of tdTomato<sup>+</sup> neocortical cells (Fig 3.3I-3.3L, 3.3W,  $p = 0.046$ ). By P7 (Fig. 3.3M-3.3P) and P16 (Fig. 3.3Q-3.3T) there were further decreases in the density of tdTomato<sup>+</sup> neocortical cells, which reached ~64% reduction at P35 (Fig. 3.3W).



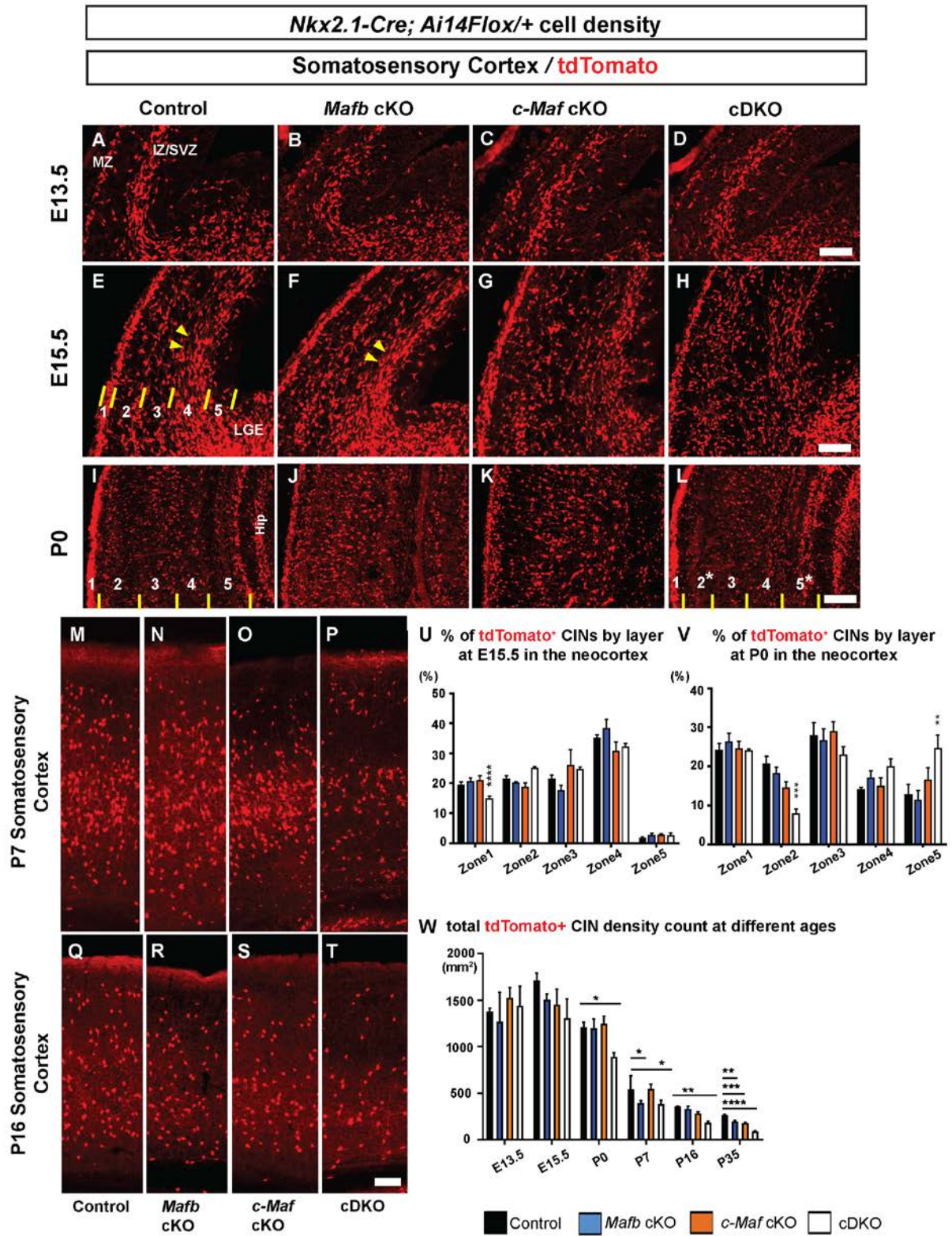




**Figure 3.3. *Mafb/ c-Maf* cKO and cDKOs have gradual reduction of CINs by P35.** (A-T) Immunofluorescent images from E13.5/ E15.5/ P0 neocortices and P7/ P16 somatosensory cortices show native tdTomato<sup>+</sup> CIN distribution. (U) Quantification of the proportion of tdTomato<sup>+</sup> cells by regions at E15.5 neocortex. Zone 1= marginal zone; Zone 2 = cortical plate and subplate; Zone 3 = intermediate zone; Zone 4 = deep migration/subventricular zone; Zone 5= ventricular zone. (V) Quantification of the proportion of tdTomato<sup>+</sup> cells by regions at P0 neocortex. Cortex was binned into 5 zones roughly by equal distance, but zone 1 was focused on the marginal zone. (W) Quantification of the number of tdTomato<sup>+</sup> cells per mm<sup>2</sup> in the neocortices or somatosensory cortices. Data are expressed as the mean  $\pm$  SEM. \**p* < 0.05, \*\**p* < 0.01, \*\*\**p* < 0.001. (n) = 3-4 for all groups. Scale bar in (D, H, L, P and T) = 100  $\mu$ m. The P35 data is the same as shown in Fig. 3.1.

Concomitant with the significant decrease in the density of neocortical tdTomato<sup>+</sup> cells starting at P0, the cDKOs had a ~42% increased density of tdTomato<sup>+</sup> cells in the hippocampus (Fig. 3.4A-3.4E, *p* = 0.007). However, the increase of hippocampal tdTomato<sup>+</sup> cells was transient; it was no longer present at P16 (Table S2). By P35, the cDKOs had a comparable reduction of tdTomato<sup>+</sup> cells in both the hippocampus and somatosensory cortex (Table S2).

We suggest that the transient increased density of tdTomato<sup>+</sup> cells in the hippocampus could be due to an “over-migration” of CINs into that region, which may contribute to the reduction in their numbers in the neocortex.

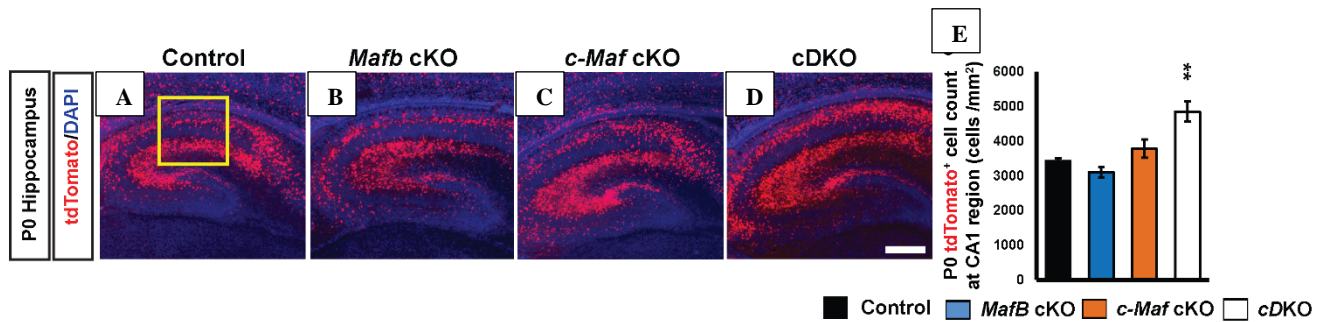


**Figure 3.4. Effect of *Maf* single and double conditional mutants (*Nkx2.1-Cre*) on the numbers of hippocampal tdTomato<sup>+</sup> interneurons at P0.** (A-D) Immunofluorescent images of the P0 hippocampus of the 4 different *Maf* genotypes. Boxed region in (A) highlights the CA1 region used for tdTomato<sup>+</sup> CIN quantification for each genotype. (E) Quantification of tdTomato<sup>+</sup> CINs per mm<sup>2</sup> in the CA1 region; (n)=4 for all *Maf* genotypes. Scale bars in (D) =100 $\mu$ m; Data are expressed as the mean  $\pm$  SEM. \*\**p* < 0.01

### **3D. MGE proliferation and CIN apoptosis are not altered in cDKOs**

Several mechanisms could lead to the reduction of CIN numbers (Fig. 3.1, Fig. 3.3). While ectopic cell accumulation in the hippocampus could account for cell loss in the neocortex, it is also possible that reduced cell proliferation and/or increased cell death play a part. We focused our subsequent analyses on the cDKOs. To study MGE proliferation, we administered 5-Ethynyl-2'-Deoxyuridine (EdU) for 30 minutes to E13.5 pregnant mice to label S-phase progenitors (schema, Fig. 3.5A). We assessed EdU<sup>+</sup> cell density in the VZ, SVZ1 and SVZ2 (secondary progenitors), and found no change in the cDKOs. (Fig. 3.5B-3.5D). Next, at E13.5 and E15.5 we determined the density of phospho-histone-3 (PH3<sup>+</sup>) cells to assess the numbers of M-phase progenitors, and again found no difference (Fig. 3.5E-3.5J). These data suggested that during peak MGE CIN generation, there were no significant differences in the number of S-phase and M-phase progenitors in the VZ and SVZ.

To determine if increased apoptosis could contribute to the CIN reduction in cDKOs, we stained for cleaved caspase-3 (CC3), a marker of apoptosis. At E13.5 and E15.5, no differences in CC3<sup>+</sup> cell densities were detected in the MGE or along the CIN migration route. At P0, P7 and P16, we also observed no differences in the density of tdTomato<sup>+</sup>/CC3<sup>+</sup> cells (data not shown).

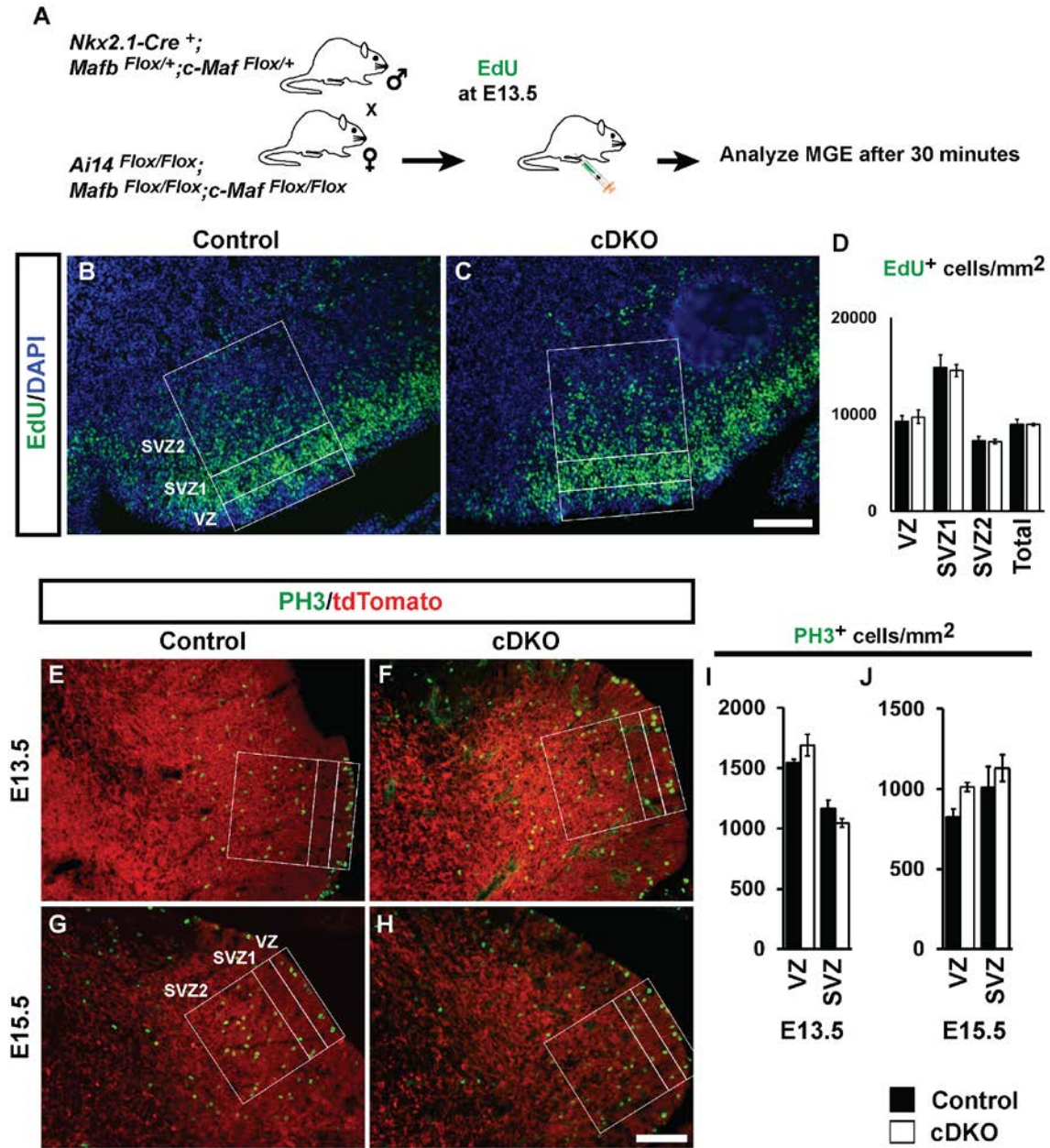


**Figure 3.5. MGE progenitors show no differences in proliferation indices in *Maf* cDKOs.** (A) Schema depicting the EdU 30-minute pulse assay. Briefly, EdU was injected into pregnant females when embryos were E13.5 and assessed after 30 minutes. Immunofluorescent images show the MGE co-stained with EdU and DAPI (B-C). (D) Quantification of EdU<sup>+</sup> progenitors per mm<sup>2</sup> by region. Immunofluorescent images from either E13.5 (E and F) or E15.5 (G and H) MGEs that were co-labeled for tdTomato and PH3. Quantification of the numbers of PH3<sup>+</sup> cells/area were calculated at E13.5 (I) and E15.5 (J) for both VZ and SVZ regions. Data are expressed as the mean ± SEM. (n)=3-4 for all groups. Student t-test was done but found no significant changes. Scale bars in (C and H) = 100 μm. Abbreviations: VZ: ventricular zone, SVZ: subventricular zone

Additionally, we stained for IBA1, a marker of active microglia, to see if increased microglia activity might contribute to the CIN reduction in cDKOs. Again, we observed no significant changes in IBA1<sup>+</sup> microglia density in the neocortex at P7 and P16 (Fig. 3.6). Thus, we did not obtain evidence for increased apoptosis and microglia engulfment contributing to the reduction in neocortical CINs in cDKOs.

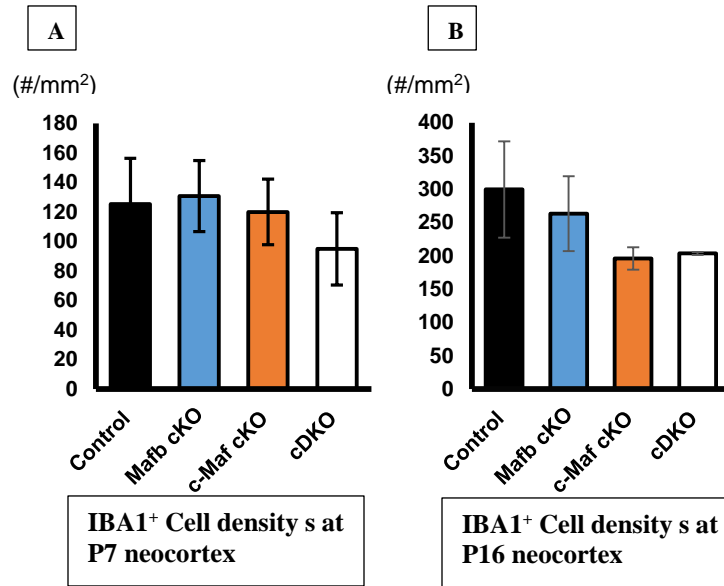


**Figure 3.6. Microglia does not account for the loss of CIN in *Maf* cDKO.** Quantification of IBA<sup>+</sup> microglia at P7 and P16 neocortex. (n)=2 per group. There was no statistically significant change between groups at both ages.

### 3E. Early born MGE lineages are over represented in cDKO adult brains

In the adult (P35) cDKO somatosensory cortex, the remaining CINs maintained the normal proportion of SST<sup>+</sup> CINs but showed a reduction of PV<sup>+</sup> CINs. Furthermore, cDKO CINs were disproportionately reduced in superficial layers (likely late born) and increased in deep layers (likely early born) (Fig. 3.1I).

We hypothesized that P35 cDKOs CINs were enriched for early-born SST CINs. The birthdate of MGE derived CINs correlates with their cell fate and laminar position. Early born (E12.5-E13.5) MGE cells tend to occupy deep neocortical lamina and express SST, while later born (E15.5) cells tend to occupy superficial lamina and express PV (Inan et al., 2012; Miyoshi et al., 2007; Pla et al., 2006). To test this hypothesis, we followed the fate of early and late born control and cDKO MGE CINs by giving EdU at either E12.5 or E15.5, and then analyzing their neocortical laminar position at P35 (schema, Fig. 3.7A). Following the E12.5 EdU pulse, we detected a 2-fold increase in the proportion of double-labeled tdTomato<sup>+</sup>;EdU<sup>+</sup> cells in cDKOs (Fig. 3.7B,  $p = 0.0003$ ). However, no differences were observed following the E15.5 pulse (Fig. 3.7C). These data support the idea that the cDKO generates disproportionately more CINs by E12.5. The laminar distribution of tdTomato<sup>+</sup>;EdU<sup>+</sup> CINs in these experiments showed no major differences, except for a trend for an increase in layer vi and a decrease in layers ii/ii/iv (Fig. 3.7D-3.7E).

Of note, the above data could be confounded by the cell loss that occurs in the cDKO neocortices by P35 (Fig. 3.1). To circumvent this, we used a prenatal, 6 hour, EdU pulse/chase paradigm (schema, Fig. 3.7A) to compare neurogenesis in the control and cDKOs MGE, before cell loss occurs. To this end, pregnant mice were given EdU when the embryos were E13.5; 6 hours later the embryos were sacrificed, and immunofluorescently co-labeled for EdU and the neuronal marker,  $\beta$ III-tubulin (Fig. 3.7F-3.7I). We quantified the percentage of EdU<sup>+</sup>  $\beta$ III-tubulin<sup>+</sup> double-positive cells to determine the fraction of cells that left the cell cycle and became immature neurons (the quiescent (Q)-fraction) (Fig. 3.7K) (Takahashi et al., 1996). We focused on the MGE SVZ, where newly generated neurons are present before they migrate.

As in previous experiments, we did not detect differences in the density of EdU<sup>+</sup> cells in the MGE (Fig. 3.5). However, the proportion of newly post-mitotic ( $\beta$ III-tubulin<sup>+</sup>; EdU<sup>+</sup>) cells (Q-fraction) generated at E13.5 increased ~2 fold in the cDKOs (Fig. 3.7K,  $p = 0.0009$ ). These data provided evidence that while loss of *Mafb*; *c-Maf* did not change the rate of proliferation, the newly generated cells were becoming neurons at an increased rate in the cDKO. This could lead to an increase in SST<sup>+</sup> CINs, perhaps at the expense of the PV<sup>+</sup> CINs.

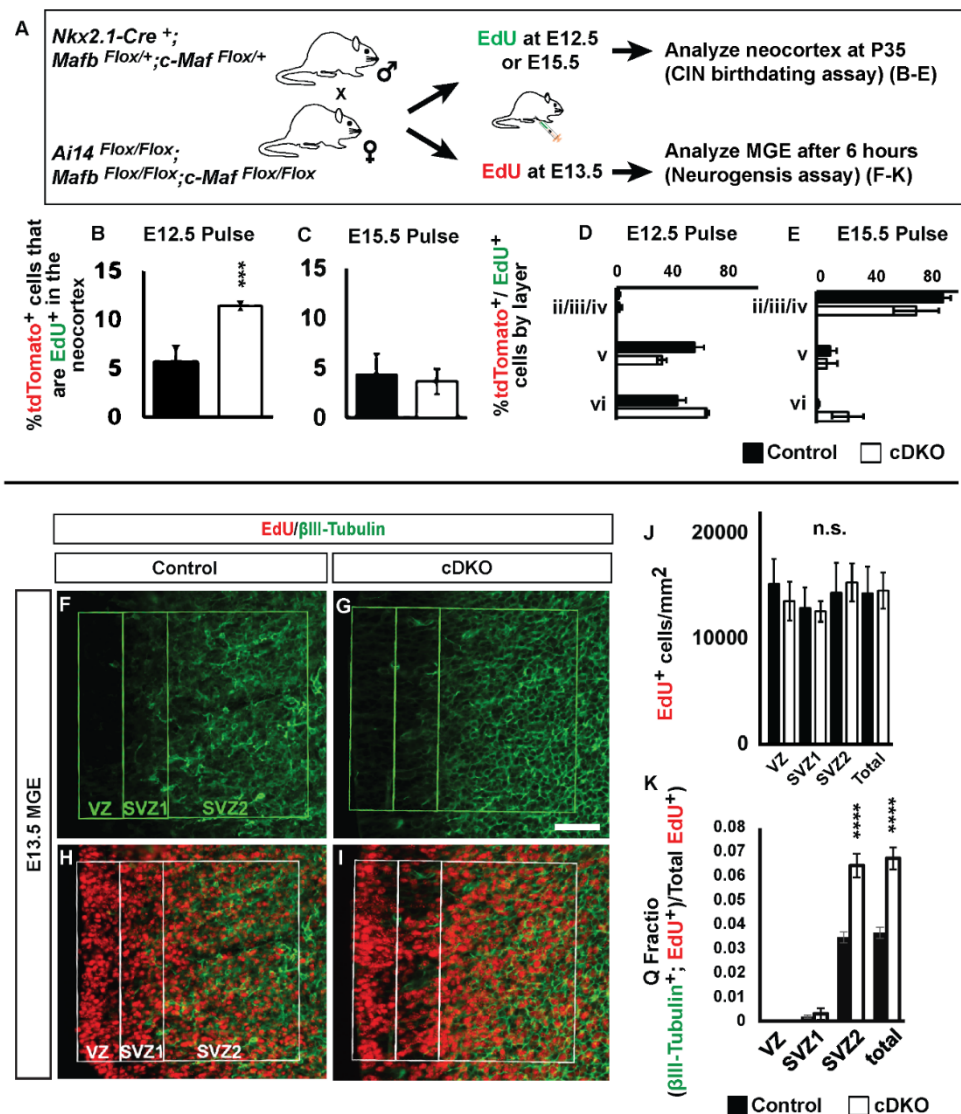


**Figure 3.7. EdU pulse chase experiments revealed that *Maf* cDKOs have increased early-born adult CINs and have precocious MGE neurogenesis.** (A) Schema depicting the EdU pulse-chase assays. To

follow CIN birthdates (**B-E**), EdU was injected into pregnant females when embryos were E12.5 or E15.5. The somatosensory cortex was assessed at P35. To study MGE neurogenesis (**F-K**), EdU was injected into pregnant females when embryos were E13.5; the embryos were analyzed 6 hours later for co-expression of EdU and  $\beta$ III-Tubulin, a neuronal marker. Quantification of EdU<sup>+</sup>;tdTomato<sup>+</sup> double-labeled cells/mm<sup>2</sup> from EdU pulses at either E12.5 (**B**) or E15.5 (**C**). Quantification, as a function of cortical lamina, of the proportion of EdU<sup>+</sup>;tdTomato<sup>+</sup> double-labeled cells from EdU pulses at E12.5 (**D**) or E15.5 (**E**). (n)=4 for all groups. Immunofluorescent images show the MGE co-stained with EdU and  $\beta$ III-Tubulin (**F-I**). Boxed region indicates VZ, early SVZ (SVZ1) and late SVZ (SVZ2). (**J**) Quantification of EdU<sup>+</sup> progenitors per mm<sup>2</sup> in the VZ, SVZ1, and SVZ2. (**K**) Quantification of the Q fraction (EdU<sup>+</sup>;  $\beta$ III-Tubulin<sup>+</sup>/EdU<sup>+</sup>) in the VZ, SVZ1, and SVZ2. (n)=3 for all groups. Data are expressed as the mean  $\pm$  SEM. \*\*\*p < 0.001, \*\*\*\*p < 0.0001. Scale bar in (**G**) = 50  $\mu$ m. Abbreviations: SVZ1: subventricular zone 1; SVZ2: subventricular zone 2; VZ: ventricular zone.

### 3F. Excessive production of SST<sup>+</sup> CINs in cDKOs

Our earlier EdU pulse-chase experiments provided evidence that cDKOs had an increased proportion of early born CINs in the adult cortex (Fig. 3.7B), as well as increased MGE neurogenesis at E13.5 (Fig. 3.7K). Thus, as the early wave of CINs are mostly *Sst*<sup>+</sup> (Inan et al., 2012; Miyoshi et al., 2007; Pla et al., 2006), we were interested in determining whether there were increased numbers of *Sst*<sup>+</sup> cells being generated in the cDKO MGE. We characterized *Sst* RNA expression by *in situ* hybridization (ISH) at E13.5, E15.5 and P0 (Fig. 3.8A-3.8C). While there was no detectable change in *Sst* expression at E13.5 (Fig. 3.8A), there was a ~2-fold increased density of cortical *Sst*<sup>+</sup> cells at E15.5 (Fig. 3.8B, 3.8E p=0.0184). This increase was even more apparent by P0 (Fig. 3.8C). Furthermore, at P0 *Sst*<sup>+</sup> cells were clearly increased in the hippocampus (caudal) and in the cingulate (rostral) cortex (Fig. 3.8C), consistent with the transient increase in neonatal MGE-lineage cells (tdTomato<sup>+</sup>) in these locations at P0 (Fig. 3.4).



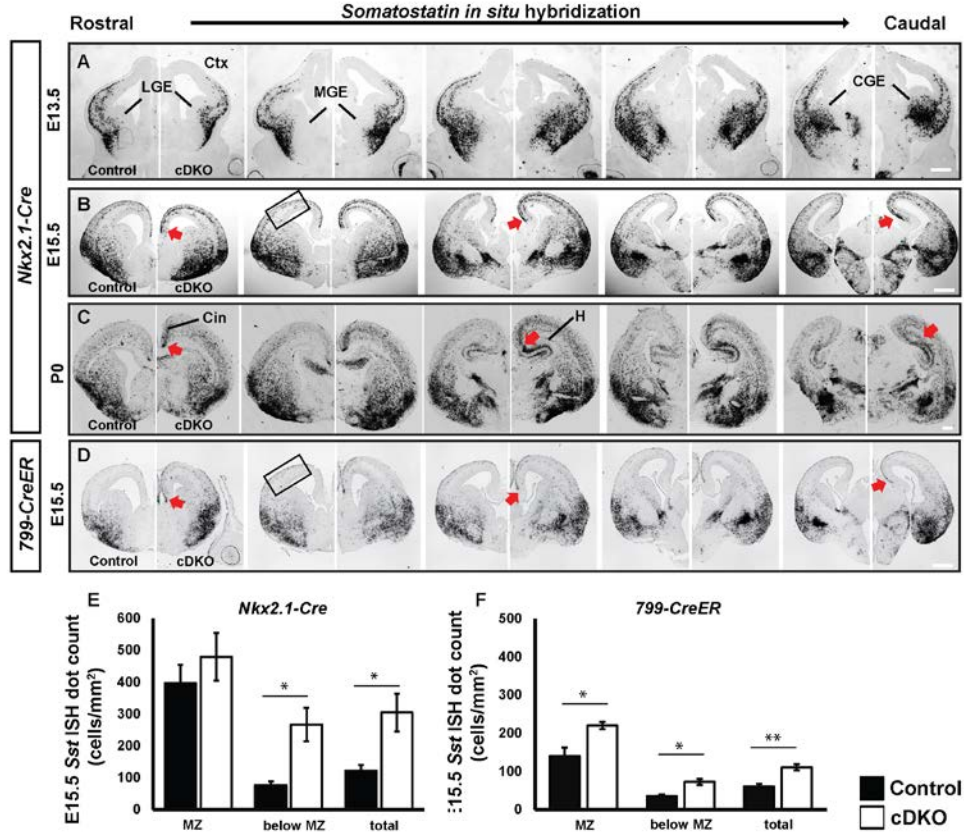


**Figure 3.8. *Mafb* and *c-Maf* regulate the quantity and position (laminar and regional) of MGE-derived *somatostatin*<sup>+</sup> interneurons during cortical and hippocampal development.** (A-C) *Sst* *in situ* hybridization at E13.5, E15.5 and P0 in control and cDKO generated using *Nkx2.1-Cre*. (D) *Sst* *in situ* hybridization at E15.5 in control and cDKO generated using *799-CreER*, whose activity begins in the SVZ. Increased numbers of *Sst* CINs in the dorsomedial cortex and hippocampus are denoted by red arrows. (E) Quantification of *Sst*<sup>+</sup> CINs per mm<sup>2</sup> by region in the neocortex in control and cDKO generated using *Nkx2.1-cre*. Increased *Sst*<sup>+</sup> CINs were observed in laminae below marginal zone (MZ) in cDKO at E15.5. (n)=4 for Control; (n)=3 for cDKO (F) Quantification of *Sst*<sup>+</sup> CINs per mm<sup>2</sup> by region in the neocortex in control and cDKO generated using *799-CreER*. Increased *Sst*<sup>+</sup> CINs were observed in the MZ and below MZ in cDKO at E15.5. (n)=4 for both groups. Data are expressed as the mean ± SEM. \*p < 0.05, \*\*p < 0.01. Scale bar in (A-D) = 500 µm. Boxed region indicates where quantification was done. Abbreviations: Cin: cingulate cortex; MGE: medial ganglionic eminence; LGE: lateral ganglionic eminence; H: hippocampus



To determine if the increase in *Sst*<sup>+</sup> cells in the cortex was related to the precocious neurogenesis observed at early ages in the MGE (Fig. 3.7K), we administered EdU to pregnant mice at E12.5 and analyzed them at E15.5 in the neocortex to assess the number of SST<sup>+</sup> and tdTomato<sup>+</sup> cells generated at earlier age (Schema Fig. 3.9A; Fig. 3.9B-3.9G). Indeed, the proportion of tdTomato<sup>+</sup> cells that expressed SST nearly doubled in cDKOs (Fig. 3.9H,  $p < 0.0001$ ). Moreover, we found that the number of triple-labeled tdTomato<sup>+</sup>;SST<sup>+</sup> CINs that were EdU<sup>+</sup> also doubled in the cDKOs (Fig. 3.9I,  $p = 0.0002$ ).

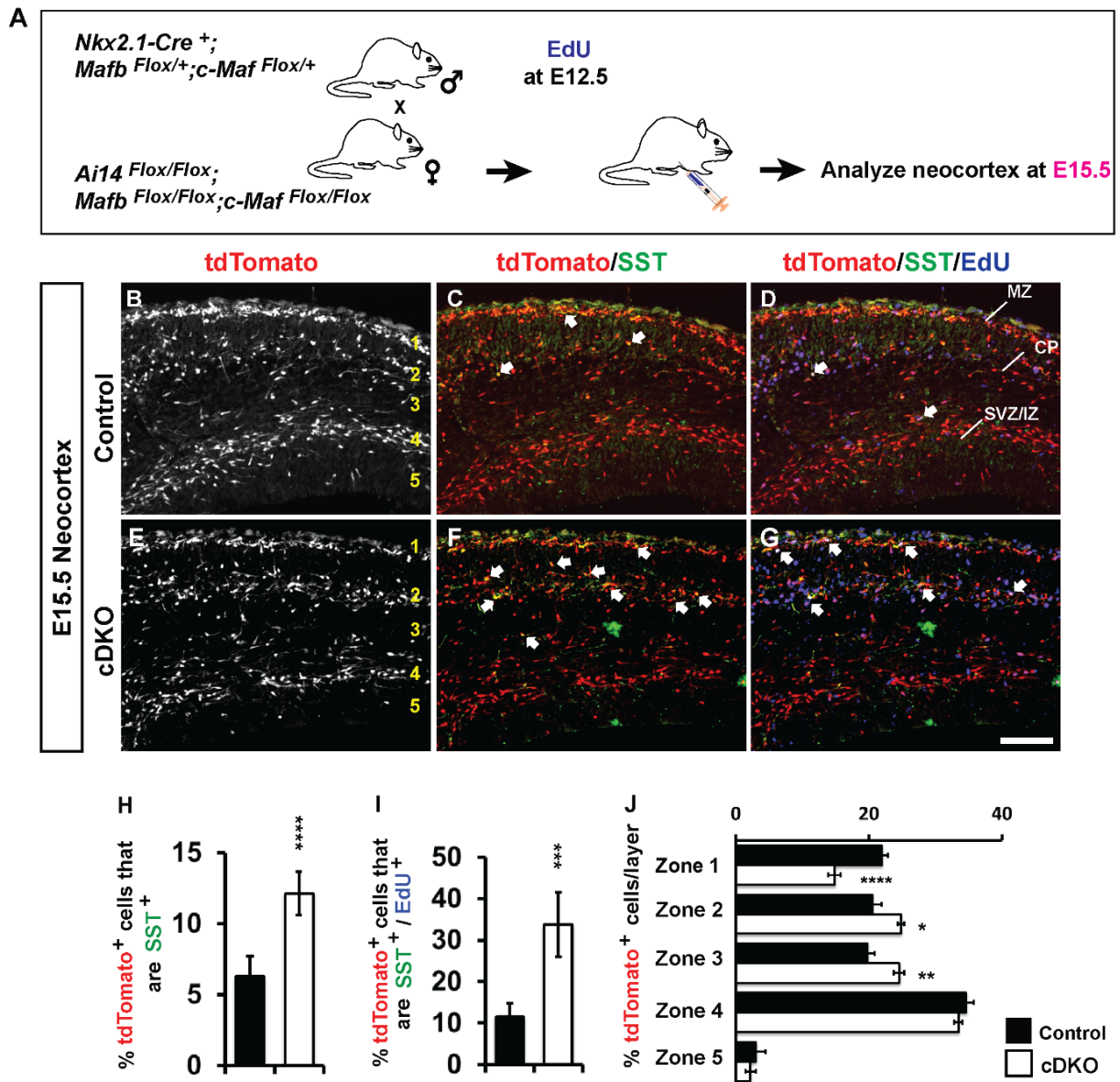


**Figure 3.9. Increased numbers of SST<sup>+</sup> interneurons in developing (E15.5) cDKO neocortex.** (A) Schema depicting the EdU 3 day pulse-chase experiment. EdU was injected into pregnant females when embryos were E12.5. The neocortices were assessed at E15.5. (B-G) Immunofluorescent images of E15.5 neocortices showing tdTomato<sup>+</sup> cells co-stained for EdU and SST. Arrows show double- or triple-labelled cells (C, D, F and G). (H) Quantification of the number of tdTomato<sup>+</sup> cells per mm<sup>2</sup> that are SST<sup>+</sup>. (I) Quantification of the number of EdU-labeled tdTomato<sup>+</sup> cells per mm<sup>2</sup> that are SST<sup>+</sup>. (J) Quantification of the proportion of tdTomato<sup>+</sup> cells for the five layers labeled in B and E. Marginal zone (zone 1), cortical plate and subplate (zone 2), intermediate zone (zone 3), deep migration stream (zone 4), and the ventricular zone (zone 5). (n)=3-4 for all groups. Data are expressed as the mean ± SEM. \*p < 0.05, \*\*p < 0.01, \*\*\*p < 0.001, \*\*\*\*p < 0.0001. Scale bars in (G) = 100 µm.

We also administered EdU to pregnant mice at E15.5 and analyzed them at P0 in the neocortex to assess SST<sup>+</sup> CIN neurogenesis at a later time point where PV<sup>+</sup> CIN is the cell type that is being actively produced. Similar to the E12.5-E15.5 pulse-chase experiment, we also identified excessive generation of SST<sup>+</sup> CINs born at E15.5 (Fig. 3.10).

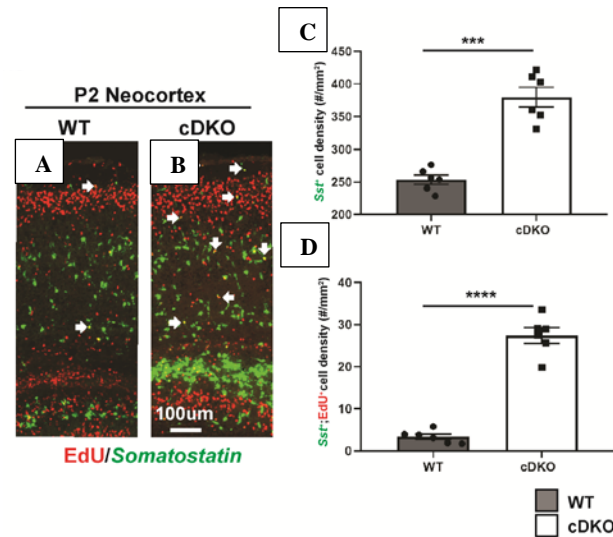


**Figure 3.10. Increased numbers of Sst<sup>+</sup> interneurons in developing (P2) cDKO neocortex (unpublished).** EdU was injected into pregnant females when embryos were E15.5. The neocortices were assessed at P0. (A-B) Immunofluorescent/fluorescent *in situ* hybridization images of P2 neocortices showing Sst<sup>+</sup> cells co-stained for EdU. Arrows show double-labelled cells. (C) Quantification of the number of Sst<sup>+</sup> cell density (#/ mm<sup>2</sup>). (D) Quantification of the number of Sst<sup>+</sup> and EdU<sup>+</sup> double positive cell density (#/mm<sup>2</sup>). (n)=3 for all groups. Data are expressed as the mean ± SEM. \*\*\*p < 0.001, \*\*\*\*p < 0.0001. Scale bar in (B) = 100µm.

Overall, these data show that without *Mafb* and *c-Maf*, the MGE has a normal density of progenitors, which generate more SST<sup>+</sup> CINs, both at E12.5 and E15.5. Since there is no increased density in cortical tdTomato<sup>+</sup> cells at E15.5 and at P0 (Fig. 3.3), we hypothesize that the remaining

tdTomato<sup>+</sup>;SST<sup>-</sup> cells are most likely the PV<sup>+</sup> lineage (although this age is too young to assess PV expression).

### 3G. *Mafb* and *c-Maf* function in SVZ progenitors to control MGE-derived CIN production

Above we provided evidence that lack of *Mafb* and *c-Maf* results in *Sst*<sup>+</sup> CIN over-production in the late SVZ of MGE (SVZ2; Fig. 3.7K). Thus, we hypothesized that *Mafb* and *c-Maf* function in the SVZ to control the production and fate of CINs. To further test this idea, we generated conditional *Maf* cDKOs using the 799-*CreER* mouse line, whose activity initiates in the SVZ of the MGE (Silberberg et al., 2016).

First, we identified, in more detail, the type(s) of MGE progenitors where 799-*CreER* activity initiates (Fig. 3.11). We induced *Cre* activity with a tamoxifen injection at E11.5, and assayed CRE activity with the *Ai14* reporter. We harvested the embryos at E12.5, 30 mins after an EdU injection. To test if there was 799-*CreER* activity in MGE progenitors, histological sections were analyzed with antibodies to tdTomato, EdU (S-phase progenitors) and Ki67 (pan-progenitor marker). We identified tdTomato and Ki67 double-positive cells in the SVZ2, and not in the VZ or SVZ1 (Fig. 3.12A-3.12B). Thus, we provided evidence that 799-*CreER* activity initiates in a subset of MGE “late” progenitors. Furthermore, MAFB and tdTomato co-localize in the MGE SVZ2, suggesting MAFB expression initiates around the time when 799-*CreER* activity begins (Fig. 3.12C-3.12E).

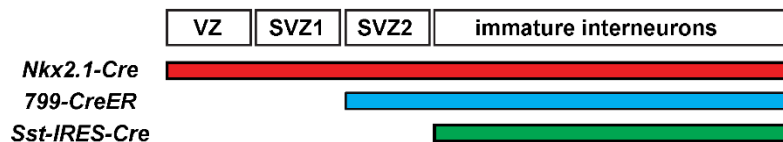


**Figure 3.11. Schema showing where each Cre line initiates recombination.**

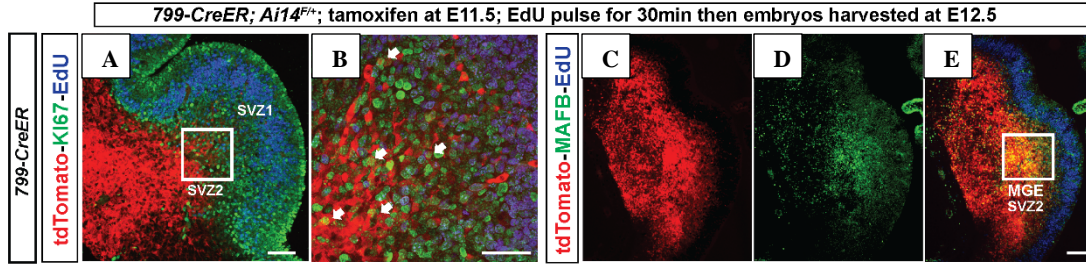


**Figure 3.12. 799-CreER activity initiates in the late SVZ (SVZ2) of MGE.** (A) Immunofluorescent images from E12.5 MGE that show co-staining of tdTomato (799-CreER lineage), EdU and KI67. (B) Higher magnification views (imaged from the boxed region in K) showing colocalization of tdTomato and KI67 in the SVZ2 of the MGE. (C-E) Immunofluorescent images from E12.5 embryonic basal ganglia that show co-staining of tdTomato, EdU and MAFB. Note the boxed region in (E) that show colocalization of tdTomato and MAFB, providing evidence that 799-CreER activity and MAFB expression both initiate in SVZ2 (late SVZ) of the MGE. Scale bars in (A) =100um; Scale bar in (B) = 50  $\mu$ m; Scale bar in (E) = 200 um. Abbreviations: SVZ1: early subventricular zone, SVZ2: late subventricular zone.

Next, we used 799-CreER (tamoxifen at E11.5) to generate cDKO embryos which were analyzed at E15.5 to test the mutation affected the number of *Sst*<sup>+</sup> CINs. *Sst* ISH showed a ~2-fold increase (Fig. 3.8D-3.8F;  $p=0.003$ ), as also observed with *Nkx2.1-Cre* mediated deletion (Fig. 3.8B, 3.8E); similar changes were also seen in CIN laminar distribution (Fig. 3.8E, 3.8F; MZ  $p=0.03$ ; below MZ  $p=0.012$ ).

Lastly, we used *Sst-IRES-Cre* (Taniguchi et al., 2011) and Ai14 (Fig. 3.13) to generate cDKO mice that express tdTomato at P0 and P30 to test whether deletion of *Mafb* and *c-Maf* expression in post-mitotic SST<sup>+</sup> lineage cells affects the numbers of SST<sup>+</sup> CINs. In the cDKO we did not observe a change in the density of tdTomato<sup>+</sup> CINs or tdTomato<sup>+</sup>; SST<sup>+</sup> CINs (Fig. 3.14).

Thus, the use of 799-CreER and *Sst-IRES-Cre* support the conclusion that MAF proteins act in the SVZ2, and not in immature CINs, to repress the generation of SST<sup>+</sup> CINs.



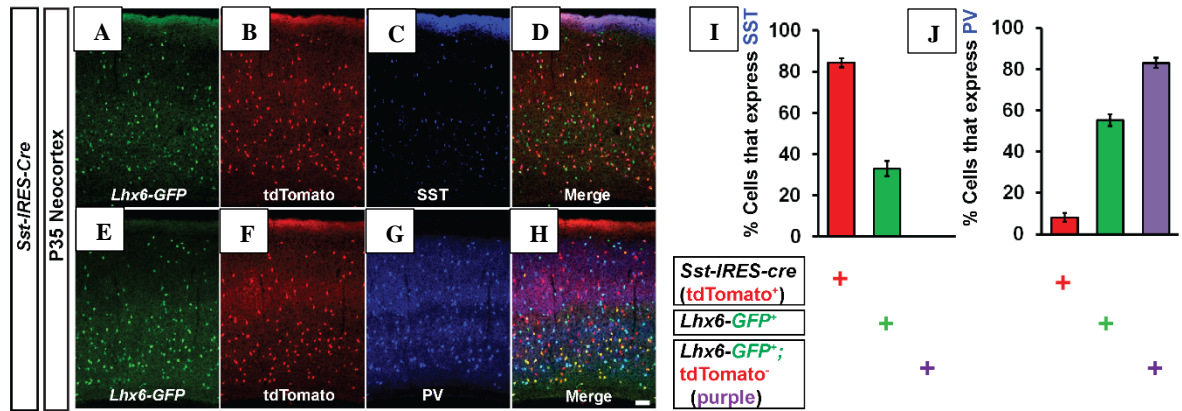


**Figure 3.13. Fate mapping of *Sst-IRES-Cre* lineage CINs in the adult CINs. (A-D)**

Immunofluorescent images from P35 neocortex that show the overlay of SST<sup>+</sup> CINs with the *Sst-IRES-Cre* lineage (tdTomato<sup>+</sup>) and Lhx6-GFP<sup>+</sup> cells (mostly MGE-derived CINs). (E-H) Immunofluorescent images from P35 neocortex that show the overlay of PV<sup>+</sup> CINs with the *Sst-IRES-Cre* lineage (tdTomato<sup>+</sup>) and Lhx6-GFP<sup>+</sup> cells. (I) Quantification of the percentage of tdTomato<sup>+</sup> CINs, Lhx6-GFP<sup>+</sup> CINs or tdTomato<sup>+</sup>;GFP<sup>+</sup> CINs that express SST. 80% of tdTomato<sup>+</sup> cells (*Sst-IRES-Cre*-lineage) were SST<sup>+</sup>. ~35% of Lhx6-GFP<sup>+</sup> CINs were SST<sup>+</sup>. None of the tdTomato<sup>+</sup>/GFP<sup>+</sup> cells were SST<sup>+</sup>. (J) Quantification of the percentage of tdTomato<sup>+</sup> CINs, Lhx6-GFP<sup>+</sup> CINs or tdTomato<sup>+</sup>;GFP<sup>+</sup> CINs that express PV. ~8% of tdTomato<sup>+</sup> cells (*Sst-IRES-Cre*-lineage) were PV<sup>+</sup>. ~55% of Lhx6-GFP<sup>+</sup> CINs were PV<sup>+</sup>. ~85% of the tdTomato<sup>+</sup>/GFP<sup>+</sup> cells were PV<sup>+</sup>. Together, this data provide evidence that most of the CINs derived from the *Sst-IRES-Cre* lineage are SST<sup>+</sup>. Data are expressed as the mean  $\pm$  SEM. \* $p < 0.05$ , \*\* $p < 0.01$ , \*\*\*\* $p < 0.0001$ . Scale bars in (H) = 100um. This figure is kindly generated by Dr. Daniel Vogt and Dr. Jia Sheng Hu.

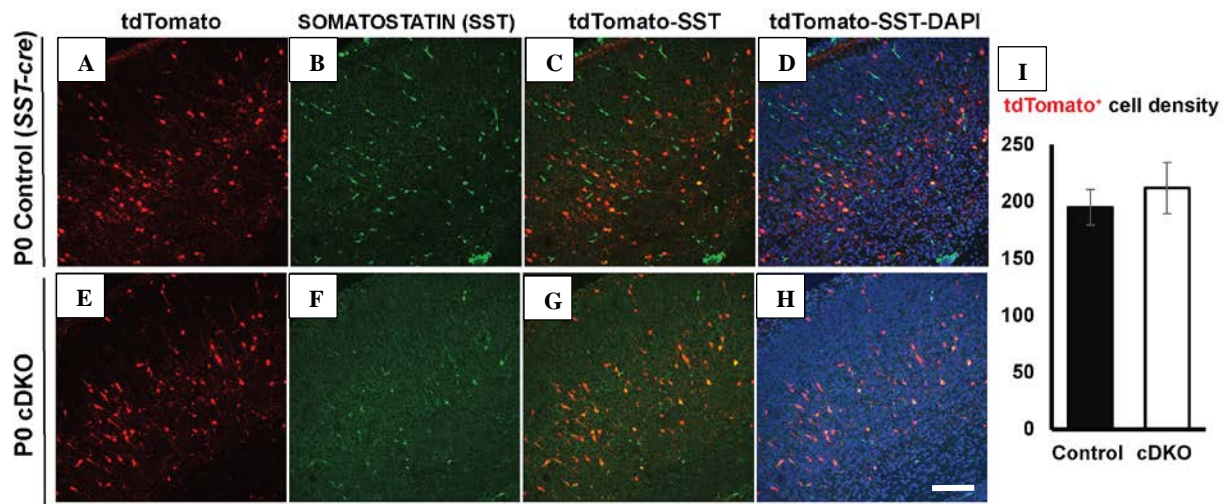


**Figure 3.14. *Sst-IRES-Cre* generated cDKOs does not have CIN loss phenotype (unpublished).**

Immunofluorescent images from P0 neocortex that show the overlay of SST<sup>+</sup> CINs with the *Sst-IRES-Cre* lineage (tdTomato<sup>+</sup>) for control (A-D) and cDKO (E-H). (I) Quantification of the density of *Sst-IRES-Cre* lineage (tdTomato<sup>+</sup>) CINs in both group. Data shows that loss of Mafb and c-Maf using *Sst-IRES-Cre* does not recapitulate the *Nkx2.1-cre* result. Scale bar in (H) = 200um.

### 3H. *c-Maf* controls CIN migration alone and together with *Mafb*

*Mafb* and *c-Maf* cDKOs, in addition to the increase in *Sst*<sup>+</sup> CINs in immature neocortex and hippocampus, also have changes in CIN migration patterns at E15.5. We quantified CIN densities of the deep and superficial migration streams using both E15.5 *Sst* ISH (Fig. 3.8E, 3.8F) and E15.5 tdTomato immunofluorescence (IF) (Fig. 3.9).

In the *Nkx2.1-Cre* mediated cDKO, the density of *Sst*<sup>+</sup> cells in lamina below the MZ was increased (Fig. 3.8E;  $p=0.02$ ). Consistent with this, the proportion of tdTomato<sup>+</sup> CINs in the MZ (zone 1) was reduced ~30% (Fig. 3.9J,  $p < 0.0001$ ). In turn, zones 2 and 3, which included the CP and subplate, had increased proportions of cells in the cDKOs (Fig. 3.9J,  $p=0.04$  and  $0.003$ , respectively), while deeper layers, zones 4 and 5, were unchanged.

We also conducted *Sst* ISH at E15.5 in the *Mafb* and *c-Maf* single cKOs (Fig. 3.15A-3.15D). While there was no obvious change in total *Sst*<sup>+</sup> cell density in the *Mafb* cKO, the *c-Maf* cKO showed a slight increase (Fig. 3.15E).

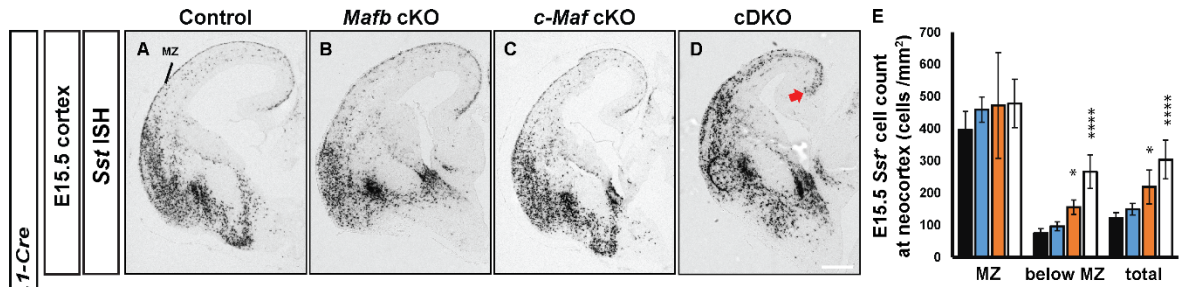


**Figure 3.15. Effect of *Maf* single and double conditional mutants (*Nkx2.1-Cre*) on the expression of *Sst* RNA at E15.5.** (A-D) *Sst* *in situ* hybridization at E15.5 in control, *Mafb* cKO, *c-Maf* cKO and cDKO. (E) Quantification of *Sst*<sup>+</sup> CINs per mm<sup>2</sup> by region in the neocortex in 4 different *Maf* genotypes. (n)=3-4 for all groups. Note that in the *c-Maf* cKOs, there was no reduction in the *Sst*<sup>+</sup> CIN density count. \*\*\*\* $p < 0.0001$ . Scale bars in (D) =200um.

Of note, tdTomato expression identified an alteration in the laminar pattern of CINs in the deep tangential migration zone at E15.5 in the *c-Maf* cKO and the cDKO. Whereas control and *Mafb* cKO have

a tightly organized deep migration zone (arrowheads Fig. 3.3E-3.3F), this region is disorganized and has ~2-fold fewer CINs in the *c-Maf* cKO and the cDKO (Fig. 3.3G-3.3H, *c-Maf* cKO  $p < 0.0001$ ; cDKO  $p = 0.0001$ ). The observation that the *c-Maf* cKO had a defect in the deep migration layer correlates with *c-Maf*'s selective expression in this location (Fig. 2.3I, 2.3K). Together these alterations in CIN laminar organization, during their tangential migration, suggest that *c-Maf* alone, and together with *Mafb*, control migration of immature CINs.

Towards understanding mechanisms underlying the migration phenotypes, we assayed *Cxcr7* RNA expression, as *Cxcr7* mutants have a reduction in migrating CINs in the MZ and an increase in the CP, a very similar phenotype observed in the distribution of tdTomato<sup>+</sup> CINs in the cDKO (Fig. 3.9J). Indeed, in the cDKO, the cortical distribution of *Cxcr7* RNA resembled that of tdTomato (Fig. 3.16O-3.16P, 3.16O'-3.16P') (Li et al., 2008; Sánchez-Alcañiz et al., 2011; Stumm et al., 2003; Wang et al., 2011). This provides evidence that *Mafb* and *c-Maf* control CIN migration independent of *Cxcr7* expression, potentially through a parallel pathway and/or downstream event.

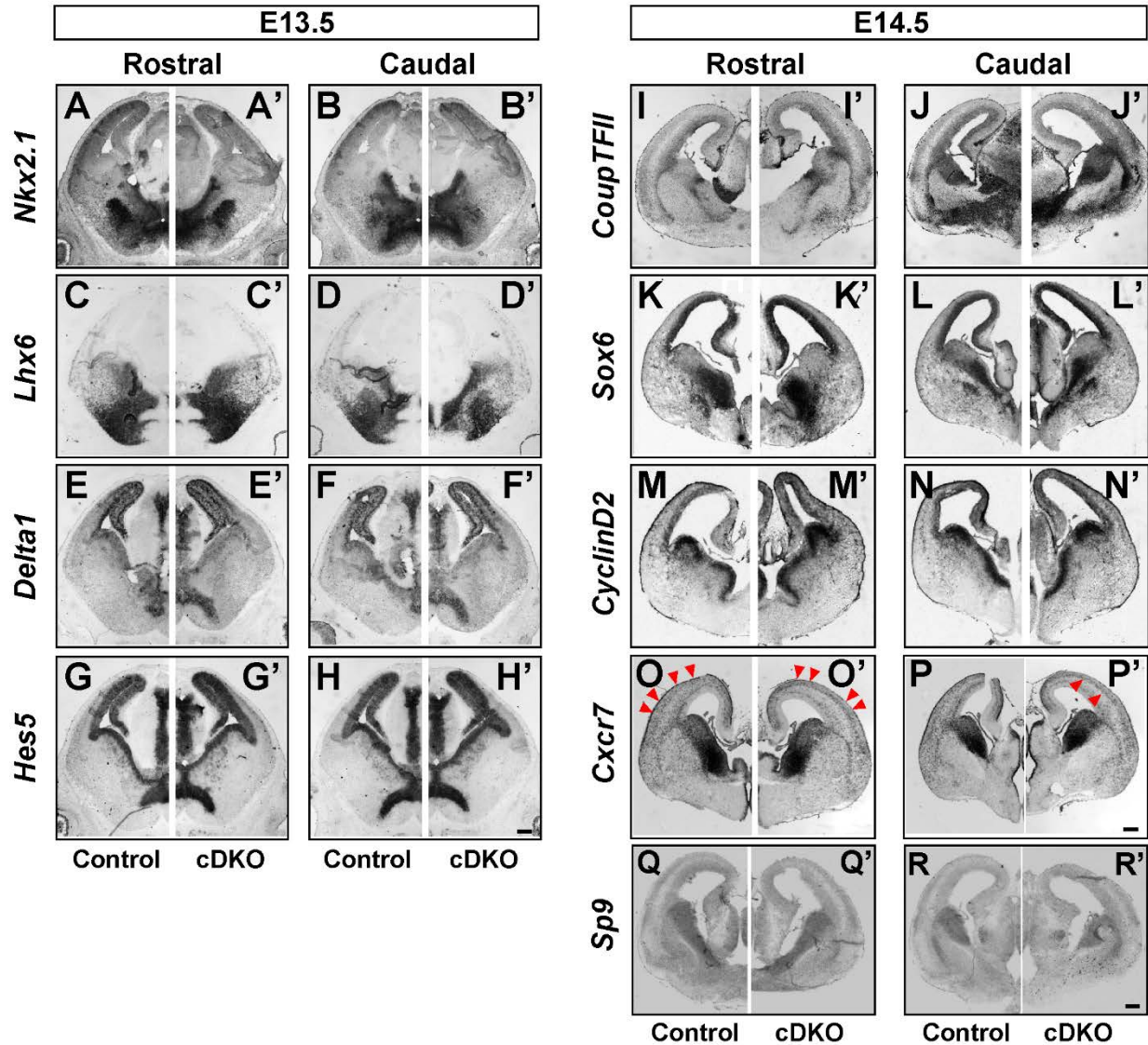


**Figure 3.16. *In situ* hybridization for genes that regulate MGE and CIN development.** Rostral and caudal coronal hemisections through the telencephalon; *in situ* hybridization shows RNA expression of *Nkx2.1* (A, A', B and B'), *Lhx6* (C, C', D and D'), *Delta1* (E, E', F and F') and *Hes5* (G, G', H and H') at E13.5. *In situ* hybridizations showing expression of *CoupTFII* (I, I', J and J'), *Sox6* (K, K', L and L'), *CyclinD2* (M, M', N and N'), *Cxcr7* (O, O', P and P') and *Sp9* (Q, Q', R and R') at E14.5. In all panels, control hemispheres are on the left and cDKO hemispheres are on the right. Scale bars in (H', P' and R') = 250  $\mu$ m.



## **Chaper 4: Postnatal function of *Mafb* and *c-Maf* in CIN action potential firing properties, synaptic excitation and cortical excitability**

### **4A. Active and passive membrane properties of CINs in the controls and *Maf* mutants**

To better understand how *Maf* mutations affect CINs physiology, we performed whole-cell patch-clamp recordings from *Nkx2.1-Cre*-lineage CINs in cortical layer 5 of the somatosensory cortex in adult control and *Maf* mutant mice (P63-P82). CINs were visually identified for electrophysiological analyses via tdTomato expression. For assessments where feasible, we post-hoc identified fast-spiking (FS) and regular-spiking (RS) CINs based on their firing patterns and analyzed their cellular electrical properties separately.

We measured the mean firing frequency of FS and RS CINs in response to the increasing intensity of the intracellular positive current injection (F-I plots, Fig. 4.1D). We found that in FS cells, the maximal firing frequency was reduced in all mutant CINs compared with controls. FS CINs from all *Maf* mutants could not sustain firing rates higher than ~60Hz and could not maintain firing rates for currents above 200pA, most prominently in the *Mafb* cKO. Interestingly, the F-I plots in RS CINs were similar between controls and all *Maf* mutants (Fig. 4.2B). These results provide evidence that loss of *Mafb* and *c-Maf* reduce the ability of FS CINs to sustain action potential (AP) firing.

In the FS CIN population, we found similar passive electrical membrane properties when comparing controls with each of the *Maf* mutants (Table S3, Top). We also observed no strong changes in single AP properties (threshold, amplitude and duration) in *Maf* mutants (Table S3, Bottom). However, there were differences when *Mafb* and *c-Maf* cKOs were compared side-by-side (Table S3, Bottom). Notably, *Mafb* cKO had lower AP threshold ( $p = 0.001$  vs. *c-Maf* cKO); increased AP amplitude ( $p = 0.025$  vs. *c-Maf* cKO); increased AP duration ( $p = 0.04$  vs. *c-Maf* cKO); and increased AP half duration ( $p = 0.02$  vs. *c-Maf* cKOs). These results suggest *Mafb* and *c-Maf* have divergent roles in regulating CIN AP properties.

In the RS CIN population, some passive electric membrane properties were different in *Maf* mutants (Table S3, Top). For instance, *Mafb* cKOs had a more depolarized resting membrane potential ( $p = 0.01$  vs. control); *c-Maf* cKOs had decreased membrane capacitance ( $p = 0.04$  vs. control); cDKOs had decreased input resistance ( $p = 0.0005$  vs. control). We observed similar AP properties between controls and all *Maf* mutants (Table S3, Bottom). These results suggest that the features of RS CINs are also altered after deletion of *Mafb* and *c-Maf*, but may not be as extensive as the changes seen in FS CINs.

#### **4B. Excitatory synaptic properties onto CINs from the controls and *Maf* mutants**

To investigate excitatory inputs onto CINs, we measured the spontaneous excitatory post-synaptic currents (sEPSCs) onto control and *Maf* mutant CINs (Fig. 4.1). sEPSCs were smaller in amplitude in *Mafb* cKO compared to control, *c-Maf* cKO and cDKO (Fig. 4.1A, 4.1C, Table S4,  $p = 0.0004$ ,  $0.002$ , and  $0.002$ , respectively), whereas the average frequency of sEPSCs was increased in *c-Maf* cKO compared to *Mafb* cKO (Fig. 4.1A, 4.1C, Table S4,  $p = 0.015$ ). These phenotypes were primarily observed in FS CINs. We found no significant differences in the decay time constant of the recorded sEPSCs across different genotypes (Table S4). These results suggest that the synaptic excitatory input is reduced onto *Mafb* cKO CINs but increased onto *c-Maf* cKO CINs.

To determine if the reduced sEPSCs amplitude observed in *Mafb* cKO resulted from changes in pre- or post-synaptic mechanisms, we measured miniature EPSCs (mEPSCs) in controls and the *Mafb* cKO CINs. Similar to sEPSCs, we observed no change in the average mEPSC frequency but a significant decrease in mEPSC amplitude in *Mafb* cKO compared to controls (Fig. 4.1C inset, Table S4 Bottom,  $p < 0.0001$ ). These results suggest that the reduced sEPSC amplitude in the *Mafb* cKO CINs was likely due to a post-synaptic mechanism rather than a reduced pre-synaptic transmitter release, and was not confounded by the increased cortical activity (Fig. 4.4).

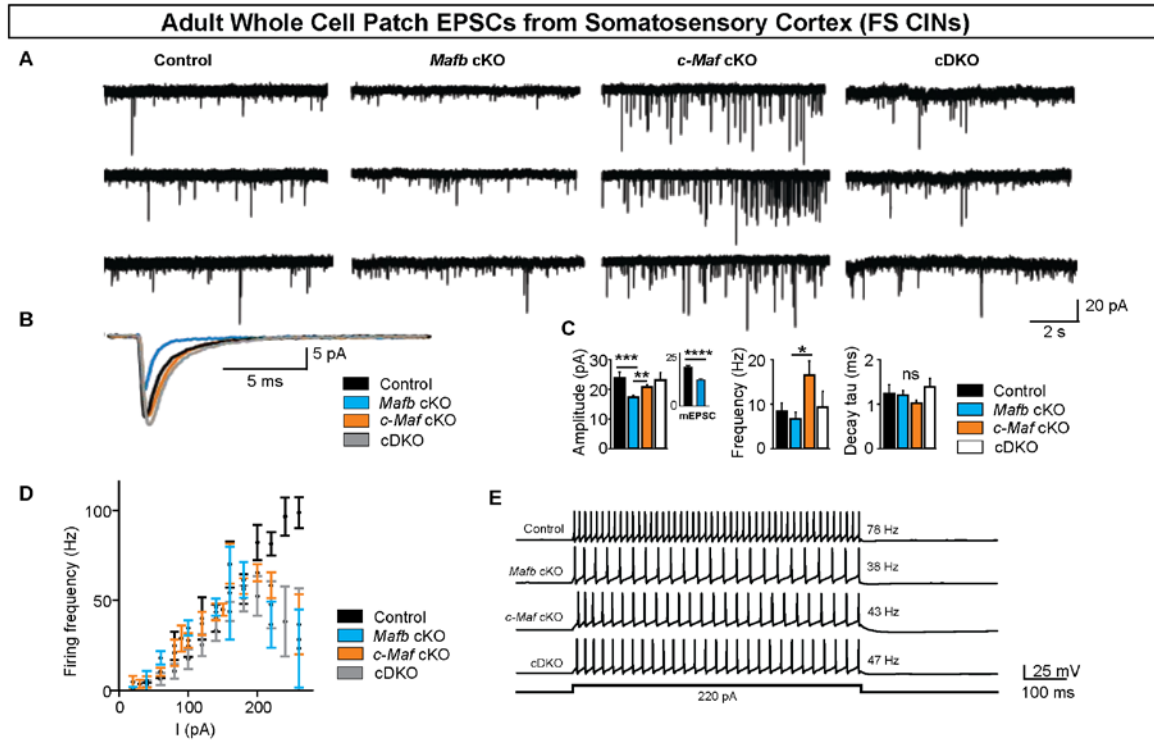


**Figure 4.1. Synaptic excitation and intrinsic excitability of Fast Spiking (FS) CINs in *Mafb* cKO, *c-Maf* cKO and cDKO mice.** (A) Representative traces of spontaneous EPSCs (sEPSCs) in layer 5-6 fast-spiking (FS) CINs. (B) Overlaid average sEPSCs from the representative cells depicted in (A). Note the reduced amplitude of sEPSC specifically in *Mafb* cKO FS CINs. (C) Quantification (mean  $\pm$  SEM) of the amplitude, frequency and decay time constant of sEPSCs ( $V_{hold} = -70$  mV) in FS CINs. Note the reduced amplitude of sEPSCs in *Mafb* cKO compared with other genotypes and the enhanced frequency of sEPSCs in *c-Maf* cKO compared with other genotypes. \* $p < 0.05$ ; \*\* $p < 0.01$ . (Control, 28 cells; *Mafb* cKO, 36 cells; *c-Maf* cKO, 39 cells; cDKO, 12 cells). Inset in (C) indicates reduced amplitude of mEPSCs in *Mafb* cKO compared with Control (Control, 24 cells; *Mafb* cKO, 16 cells; \*\*\* $p < 0.001$ , Mann-Whitney test). (D) F-I curve for FS CINs- a Plot of the mean action potential firing frequency as a function of current intensity injected in the FS CINs (Control, 19 cells; *Mafb* cKO, 32 cells; *c-Maf* cKO, 43 cells; cDKO, 12 cells). Note the inability of all *Maf* mutant FS CINs to sustain firing frequencies higher than  $\sim 60$  Hz, compared with control CINs that can exhibit firing rates  $> 100$  Hz.  $p < 0.0001$  for all genotypes. (E) Representative firing traces from FS CINs for each genotype.

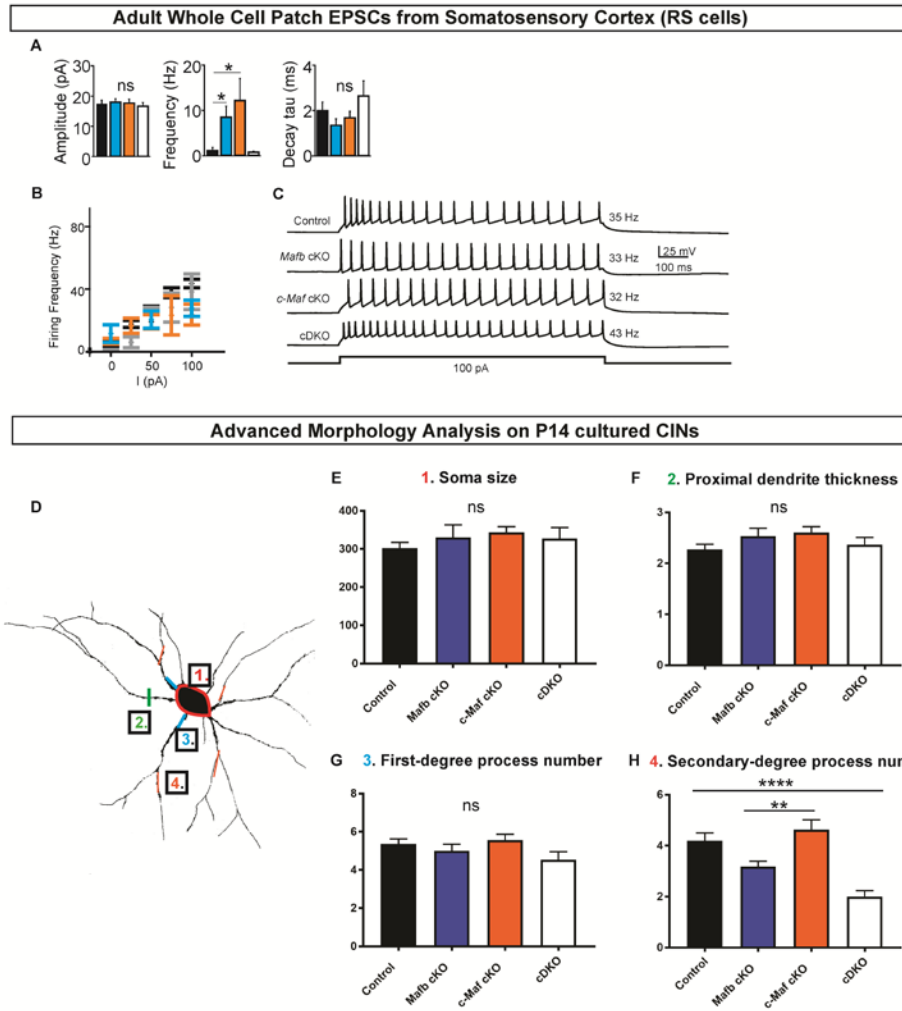


**Figure 4.2. (A-C) Synaptic excitation and intrinsic excitability of RS CINs in control, *Mafb* cKO, *c-Maf* cKO and cDKO mice. (D-H) Neurite complexity analysis on CINs from control, *Mafb* cKO, *c-Maf* cKO and cDKO following 14 days of *in vitro* cortical culture. (A)** Quantification (mean  $\pm$  SEM) of the amplitude, frequency and decay time constant of sEPSCs ( $V_{\text{hold}} = -70\text{mV}$ ) in RS CINs. Note no change in amplitude or decay of sEPSCs and the increased frequency in *Mafb* and *c-Maf* cKOs compared with controls. \* $p < 0.05$ , One Way ANOVA Kruskal-Wallis. (Control: 7 cells; *Mafb* cKO: 11 cells; *c-Maf* cKO: 6 cells; cDKO: 4 cells). **(B)** F-I curve: Plot of the mean action potential firing frequency as a function of current intensity injected in the RS cells. Overall, no significant change was observed between groups. **(C)** Representative traces from RS CINs for each genotype. **(D)** Schema depicting the regions that were quantified: soma size “1”, dendrite thickness “2”, primary neurite “3” and secondary neurite “4”. **(E)** Quantification (mean  $\pm$  SEM) of soma size for 4 *Maf* genotypes. (Control: 15 cells; *Mafb* cKO: 12 cells; *c-Maf* cKO: 19 cells; cDKO: 15 cells) **(F)** Quantification (mean  $\pm$  SEM) of proximal dendrite thickness. (Control: 43 neurites; *Mafb* cKO: 35 neurites; *c-Maf* cKO: 59 neurites; DKO: 38 neurites) **(G)** Quantification (mean  $\pm$  SEM) of primary neurite numbers. (Control: 14 cells; *Mafb* cKO: 12 cells; *c-Maf* cKO: 18 cells; cDKO: 15 cells) **(H)** Quantification (mean  $\pm$  SEM) of secondary neurite numbers. (Control: 21 cells; *Mafb* cKO: 17 cells; *c-Maf* cKO: 22 cells; cDKO: 24 cells). \*\* $p < 0.01$ , \*\*\*\* $p < 0.0001$ ; One Way ANOVA followed by Turkey’s multiple comparisons test.

#### **4C. *c-Maf* cKO CINs had an increased density of excitatory synapses and increased neurite complexity *in vitro***

To determine if the changes in the *Maf* mutant sEPSCs were due to a change in glutamatergic synapse densities and/or CIN morphology, we grew primary cortical neurons for 14 days from control, *Mafb* cKO, *c-Maf* cKO and cDKO P0 mice. We then analyzed soma size, neurite complexity (Sholl analysis) and the excitatory synapse density on proximal dendrites of tdTomato<sup>+</sup> CINs (Fig. 4.3, schema 4.2D). Soma size was similar between controls and all *Maf* mutants (Fig. 4.2E). Sholl analysis revealed that the cDKOs had decreased neurite complexity (Fig. 4.3I-4.3K), whereas the *c-Maf* cKOs had increased neurite complexity (Fig. 4.3F-4.3H). Next, we studied excitatory synapses using vGLUT1 and PSD95 as pre- and post- synaptic markers (Fig. 4.3A-4.3B). CINs from *c-Maf* cKOs had an increased density of excitatory synapses compared to both controls and *Mafb* cKOs (Fig. 4.3B,  $p=0.008$  and  $0.0001$ , respectively), in agreement with an increased frequency of sEPSCs in *c-Maf* cKO (Fig. 4.1A, 4.1C). On the other hand, the *Mafb* cKOs showed a trend for reduced density of excitatory synapses compared to controls, and a significant decrease compared with *c-Maf* cKOs (Fig. 4.3B,  $p=0.0001$ ). Of note, excitatory synapse density in the cDKOs resembled that of the control, supporting the hypothesis that *Mafb* and *c-Maf* have opposite effects on synaptogenesis, which could have important impacts on physiological phenotypes in the single and double mutants. Notably, the normal excitatory synapse density result in the cDKO is consistent with the finding that sEPSCs were similar between the control and the cDKO (Fig. 4.1A, 4.1C, 4.3G).

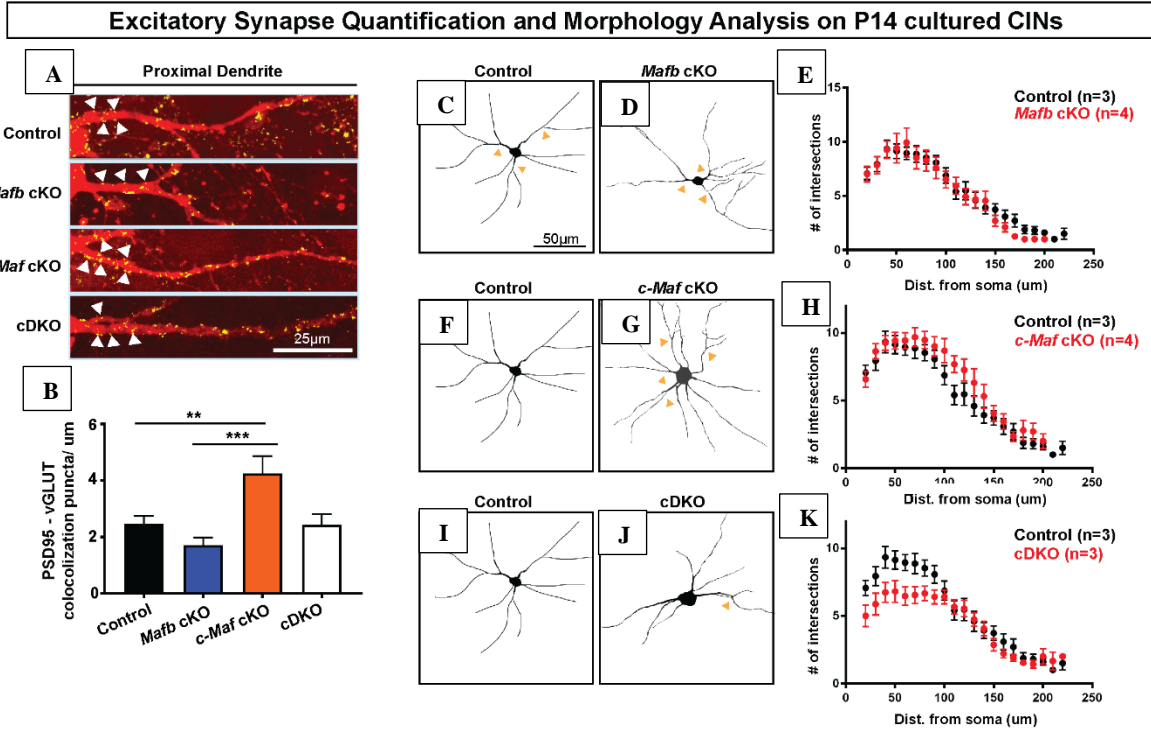


**Figure 4.3. Excitatory synapse quantification and morphology analysis of *Nkx2.1-cre*-lineage CINs from *Mafb* cKO, *c-Maf* cKO and cDKO.** (A) Confocal immunofluorescence analysis of tdTomato<sup>+</sup> CINs grown in *in vitro* for 14 days (14 DIV). Representative flattened Z-plane images of excitatory synapse labeling in the 4 *Maf* genotypes. Yellow dots represent the colocalized punta of tdTomato, PSD95 and vGLUT1 staining. (B) Quantification (mean  $\pm$  SEM) of excitatory synapses on proximal dendrites (within 15  $\mu\text{m}$  from soma); (n)=3-4 (animals) per genotype and 20-30 proximal dendrites were analyzed per group. \*\* $p < 0.01$ ; \*\*\* $p < 0.001$ . (C-D) Representative images of Control and *Mafb* cKO CINs at DIV14. (E) Quantification (mean  $\pm$  SEM) of Sholl analysis between Control and *Mafb* cKO CINs. (F-G) Representative images of Control and *c-Maf* cKO CINs at DIV14. (H) Quantification (mean  $\pm$  SEM) of sholl analysis between Control and *c-Maf* cKO CINs. (I-J) Representative images of Control and cDKO CINs at DIV14. (K) Quantification (mean  $\pm$  SEM) of Sholl analysis between Control and cDKO CINs. Note the increase in neurite complexity in *c-Maf* cKO and decrease in neurite complexity in cDKO. (n)=3-4 (animals) for all groups. (each genotype has 15-20 cells analyzed). Scale bar in (A) = 25 $\mu\text{m}$  and in (C) = 50 $\mu\text{m}$ .

#### **4D. Slice local field potential analyses showed that *Mafb* cKOs had increased neo-cortical circuit excitability unlike the *c-Maf* cKO and cDKOs.**

To further assess the effect of the *Maf* mutations on cortical circuit excitability, we measured the Local Field Potentials (LFPs) in acute brain slice preparations from the adult somatosensory cortex. We recorded LFPs across all cortical lamina evoked by electrical stimulation of the white matter tract (Schema, Fig. 7A). We performed current-source density (CSD) analysis (Aizenman et al., 1996) to determine the patterns of cortical activation between all genotypes. Notably, the CSD pattern was most significantly affected in the *Mafb* cKO neocortex, which showed a pattern consistent with hyper-excitability with an altered spatio-temporal pattern of synaptic sources and sinks, where darker blue and red represent more deviation from normal activation (Fig. 4.4C). In contrast, the CSD pattern of *c-Maf* cKOs suggested that cortical activity was diminished (Fig. 4.4B, 4.4C). Interestingly, cortical excitability of the cDKOs fell in between that of *Mafb* and *c-Maf* cKOs (Fig. 4.4B, 4.4C). Quantification of the duration of the response to the stimulus, line-length, and the amplitude of the evoked LFPs across layers show the above differences between *Maf* mutants (Fig. 4.4D, 4.4E), and detailed statistical comparisons between groups can be found in Table S5.

Thus, LFP analysis provides evidence that the *Mafb* cKO results in cortical circuit hyper-excitability whereas the *c-Maf* cKO results in cortical circuit hypo-excitability. Notably, the finding that cDKOs have relatively normal excitability in this assay, provides further evidence that *Mafb* and *c-Maf* control excitability in divergent ways.

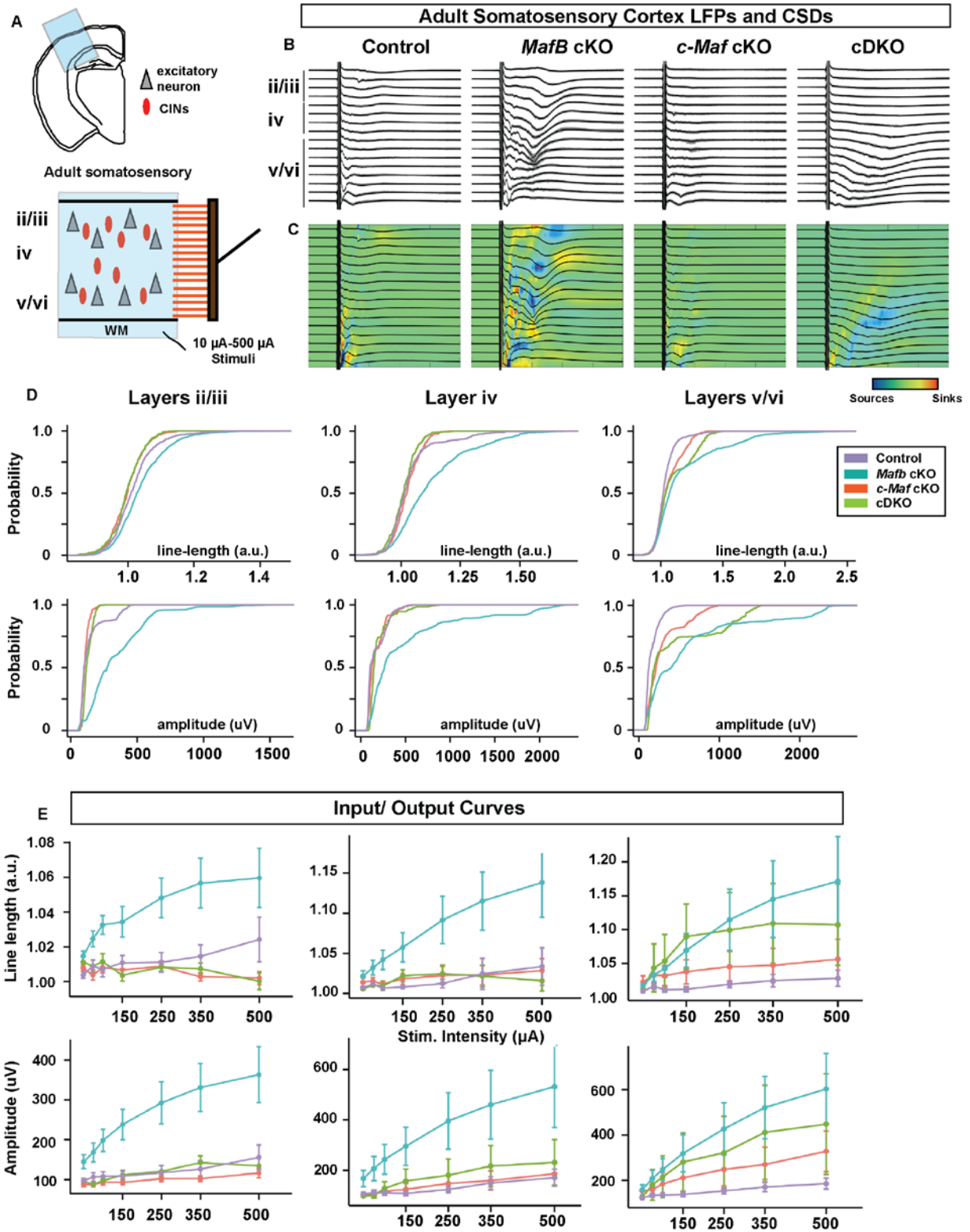




**Figure 4.4. Local Field Potentials (LFPs) and current source densities (CSDs) for neocortical slices illustrate cortical hyper-excitability in *Mafb* cKOs but not in *c-Maf* cKOs or DKO mice.** (A) Schema depicting the LFP multi-array experiment. (B) Examples of average LFPs (black) overlaid on the individual LFPs recordings (gray) for representative slices. (C) CSDs for the average LFPs of the representative slices. Blue indicates a source and red indicates a sink. (D) Bootstrapped cumulative probability distributions of the amplitude and the line-length (see Methods for details) of the LFP evoked by 500  $\mu$ A stimulation of the white matter. Note that *Mafb* cKOs show greater excitability in all layers at 500  $\mu$ A (indicated by greater line-length and amplitude in all layers compared with all genotypes), whereas *c-Maf* cKOs show hypo-responsiveness in superficial layers (indicated by reduced line-length and amplitude in layers 2-3 compared with control). (E) Average LFP responses for increasing stimulation intensities of the white matter. Note that average responses for *Mafb* cKOs in all layers show greater intensity-dependent-responses than the other genotypes. Note that only in layers 5-6 DKOs show a trend towards enhanced excitability approaching that of *Mafb* cKOs. 6 Controls, 7 *Mafb* cKOs, 6 *c-Maf* cKOs and 3 cDKOs were used for the analyses. Graphs in (E) are shown as mean  $\pm$  SEM; P values are in Table S5.

## **Chapter 5: Discussion of main findings**

### **5A. *Mafb* and *c-Maf* control MGE CIN numbers**

*Mafb* and *c-Maf* are expressed in the MGE SVZ, and persist in migrating immature and mature CINs, but not in pallidal projection neurons, unlike other known MGE TFs (Hu et al., 2017). Thus, we wondered whether loss of *Mafb* and *c-Maf* together might abort the specification of MGE-derived CINs; however, this was not the case, as cDKOs still generated CINs that tangentially and radially migrated to the neocortex (Fig. 3.1, Fig. 3.3). This raised the possibility that other TFs are responsible for generating CINs versus projection neurons. These TFs may coordinate with *Lhx6*, *Nkx2-1*, *Dlx1/2* and *Zfhx1b* that have already been shown to contribute to initiating CIN specification (Anderson et al., 1997; McKinsey et al., 2013; Sussel et al., 1999; Zhao et al., 2008).

*Maf* cDKOs have decreased SST<sup>+</sup> and PV<sup>+</sup> CINs at P35 with a preferential loss of PV<sup>+</sup> CINs (Fig. 3.1). In addition, about 40% of the tdTomato<sup>+</sup> cells in the cDKO don't express SST and PV (in the control group, about 20% of the tdTomato<sup>+</sup> cells don't express SST and PV, which could be due to antibody labeling efficiency). This could be due to a change in cell fate. We explored whether the ~20% "missing" cells in the cDKO had an alternative fate. We investigated whether the PV<sup>+</sup> cells were converted into *Cck*<sup>+</sup> basket cells, CGE-type CINs (SP8<sup>+</sup>), other types of INs (nNOS<sup>+</sup>, NPAS1<sup>+</sup>), cholinergic striatal interneurons (CHAT<sup>+</sup>), or oligodendrocytes (OLIG2<sup>+</sup>), but we did not find an increase in these cell-types in the cortex of cDKOs (data not shown). Thus, we hypothesize that ~20% of the MGE lineage CINs in the cDKO may be either some other cell type or poorly differentiated PV<sup>+</sup> CINs. Furthermore, our MGE transplant data support this conclusion (Fig. 3.2). Alternatively, CINs in the cDKO may have impaired maturation or abnormal responses to environmental perturbations, which in turn could affect SST and PV expression.

## **5B. *Mafb* and *c-Maf* provide a brake on neural differentiation**

*Mafb* and *c-Maf* control proliferation in hematopoietic stem cell, macrophages and epidermal cells (Lopez-Pajares et al., 2015; Sarrazin et al., 2009; Soucie et al., 2016). Their expression in the SVZ suggests that they could regulate proliferation of secondary progenitors in the MGE. However, we did not observe such changes in the cDKO MGE (Fig. 3.5). On the other hand, in the SVZ of cDKOs we observed increased expression of  $\beta$ III-tubulin, a marker of immature neurons at E13.5 (Fig. 3.7K). This provides evidence that *Mafb* and *c-Maf* restrain neurogenesis. Thus, *Mafb* and *c-Maf*, by serving as a brake on neural differentiation, may regulate cell fate specification.

## **5C. *Mafb* and *c-Maf* repress SST CIN fate**

SST CINs are largely generated before PV CINs (Inan et al., 2012; Miyoshi et al., 2007; Pla et al., 2006). Here we show that *Mafb* and *c-Maf* control this temporal sequence by restraining the production of SST CINs. The cDKOs generate excessive SST<sup>+</sup> MGE-derived cells, many of which become CINs. As early as E15.5, there is an obvious increase in immature SST<sup>+</sup> CINs without any increase in total numbers of MGE-derived cells (Fig. 3.3, Fig. 3.9). Moreover, we show that at E15.5, there were increased SST<sup>+</sup> CINs that were born around E12.5 (Fig. 3.9). Analyses (ISH) of multiple regulators of MGE development did not yield insights into how *Mafb* and *c-Maf* repress SST fate or promote PV fate (Fig. 3.16). Thus, we hypothesize that *Mafb* and *c-Maf* control the timing of when other factors specify SST and PV CIN fate.

## **5D. *Mafb* and *c-Maf* functions begin in SVZ2 of the MGE to control CIN fate**

Are SST and PV CINs produced by different MGE progenitors? There is a proposal that SST<sup>+</sup> CINs primarily arise by direct neurogenesis from radial glial progenitors in the VZ, whereas PV<sup>+</sup> CINs are produced by secondary progenitors in the SVZ (Petros et al., 2015). Our results are not fully

consistent with this model. Given that *Mafb* and *c-Maf* repress the generation of SST CINs, it is likely that these TFs are functioning autonomously in cells that produce SST CINs. *Mafb* and *c-Maf* are expressed in the SVZ and are not detected in the VZ at E12.5 and E15.5 (Fig. 1.1, Fig. 2.3), arguing that these TFs are repressing SST CIN production in SVZ progenitors.

To further address *Mafb* and *c-Maf* functions in the SVZ, we used the recently generated 799-*CreER* line (Silberberg et al., 2016a). Here we demonstrated that 799-*CreER* activity begins in the SVZ2 of MGE (Fig. 3.12). SVZ2 is thought to contain the most mature progenitors of the ganglionic eminences (Petryniak et al., 2007). We utilized 799-*CreER* to generate *Maf* cDKOs and found that they phenocopy the increase in *Sst*<sup>+</sup> CINs at E15.5 in the *Nkx2.1-Cre* cDKO (Fig. 3.8). Notably, we did not observe a decrease in tdTomato<sup>+</sup> CIN numbers using *SST-IRES-Cre*, unlike the *Nkx2.1-Cre* generated *Maf* cDKOs (Fig. 3.14). This provides evidence that *Mafb* and *c-Maf*, in the SVZ2, and not in postmitotic neurons, controls the decision between SST and PV CIN fate.

We hypothesize that the MGE SVZ produces both SST and PV CINs, and that *Mafb* and *c-Maf* control the probability and timing of SST and PV CIN generation by repressing SST CIN fate and promoting PV CIN fate (Model upper panel, Fig. 5.1), a model not fully consistent with Lim et al (Lim et al., 2018a). Moreover, contrary to our hypothesis, Mi et al. proposed that *c-Maf* promotes the generation of SST<sup>+</sup> CINs based on loss-of-function and viral gain-of-function studies. We agree that adult *c-Maf* mutants have reduced SST<sup>+</sup> CINs (Fig. 3.1; Table S2). However, at E15.5 we did not detect a reduction in *Sst*<sup>+</sup> CINs in the *c-Maf* cKO (Fig. 3.15), supporting the idea that the reduction is caused by postnatal CIN loss (Fig. 3.3).

## **5E. Interneurons in *Maf* mutants show laminar and regional mislocalization**

The combined loss of *Mafb* and *c-Maf* partially phenocopies the prenatal lamination defect of *Cxcr4* and *Cxcr7* mutants which have a depletion of tangentially migrating cells in the MZ and their

premature entry into the CP (Fig. 3.9) (Li et al., 2008; Sánchez-Alcañiz et al., 2011; Wang et al., 2011). Thus, we investigated *Cxcr7* expression in the cDKO, but found that its expression levels appeared normal at E14.5 (Fig. 3.16).

Lamination defects were also observed in the P35 cDKO cortices (Fig. 3.1); they had greater numbers of CINs in deep (layer vi), and fewer CINs in superficial (layers ii-iv) lamina, a phenotype also observed in the *Cxcr7* cKO adult cortex (Wang et al., 2011). This further raises the possibility that the CXCR signaling pathway is regulated by *Mafb* and *c-Maf*.

The cDKOs exhibited an additional migration defect: excessive numbers of MGE-derived INs in the P0 hippocampus (Fig. 3.4, Fig. 3.8). We suggest that this may reflect a defect in the ability of migratory CINs to detect signals to stop in the neocortex, thus, resulting in continued migration into the hippocampus. However, the *Maf* cDKO interneuron accumulation in the hippocampus diminished over time, and by P35 the hippocampus had reduced tdTomato<sup>+</sup> cells (Table S2). Thus, both CINs and hippocampal interneurons reduce over time in *Maf* mutants.

#### **5F. *Mafb* and *c-Maf* have distinct roles in regulating fast-spiking CINs and neocortical circuit function postnatally**

Our results suggest that *Mafb* and *c-Maf* have distinct functions postnatally in regulating the physiological properties of FS CINs. The finding that sEPSC and mEPSC amplitudes were smaller in the *Mafb* cKO suggests that *Mafb* promotes excitation of FS CINs (Fig. 4.1). This result is consistent with evidence that *Mafb* mutant spiral ganglion neurons had reduced postsynaptic AMPA receptors (Lu et al., 2011; Yu et al., 2013). The reduced excitation of CINs in the *Mafb* cKO, could account for the enhanced circuit excitability observed in their LFP recordings (Fig. 4.4). On the other hand, the *c-Maf* cKO CINs had an increased density of excitatory synapses and their sEPSC frequency was enhanced compared to the *Mafb*

cKO CINs, suggesting that *c-Maf* represses CIN excitation (Fig. 4.1). The enhanced excitability of CINs in the *c-Maf* cKO could explain the lower circuit excitability in their LFP recordings (Fig. 4.4).

Of note, the cDKO has intermediate phenotypes in the LFP, sEPSC and excitatory synapse analyses. This raises the possibility that *Mafb* and *c-Maf* have distinct transcriptional effects, potentially opposing roles, in maturing and/or mature CINs and cortical circuit excitability (Model lower panel, Fig. 5.1).

The finding that *Mafb* and *c-Maf* mutations mainly affect FS CINs suggest that these *Maf* genes regulate network excitability mainly by regulating the FS CINs. The fact that *Mafb* and *c-Maf* cKOs as well as cDKO all have reduced firing of FS CINs in response to current injections (Fig. 4.1D, F-I curve), but that *Mafb* and *c-Maf* mutations have distinct effects on synaptic excitation of these cells, suggests that the opposing roles of *Maf* genes on cortical network excitability mainly result from their distinct effects on the synaptic rather than intrinsic electric properties of CINs. Future experiments, such as electrocorticographic recordings, will be useful to determine how the *Mafb* and *c-Maf* mutations affect neocortical activity and pathophysiology *in vivo*.

In summary, we propose that in the MGE SVZ, *Mafb* and *c-Maf* have redundant functions in controlling the balance of SST and PV CINs generation, whereas in postnatal/maturing CINs *Mafb* and *c-Maf* have opposite functions in controlling CIN physiology. Ongoing studies are aimed at elucidating the molecular mechanisms underlying these overlapping and distinct functions of *Mafb* and *c-Maf*.

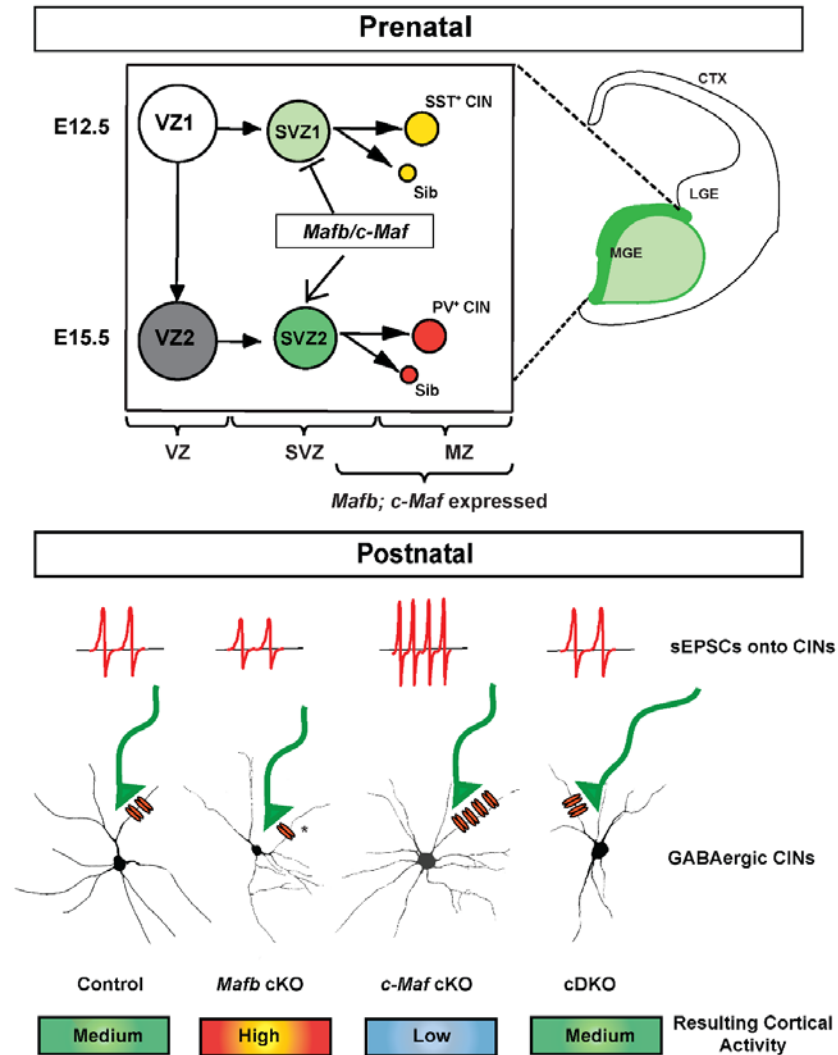


**Figure 5.1. Models of *Mafb/c-Maf* function in MGE CIN cell type specification and dendritic/synaptic/ function maturation.**

**Upper panel:** Hypothesis for redundant prenatal roles for *Mafb* and *c-Maf* in CIN cell type specification. In the absence of both *Mafb* and *c-Maf* (cDKO) in the SVZ, there is excessive generation of SST<sup>+</sup> CINs. In the postnatal brain, after normalizing for the loss of CINs, there are decreased numbers of PV<sup>+</sup> CINs. We hypothesize that the reduction of PV<sup>+</sup> CINs may due in part to a role of *Mafb* and *c-Maf* in promoting PV<sup>+</sup> CIN identity in the SVZ of the MGE. Furthermore, we postulate that *Mafb* and *c-Maf* repress SST<sup>+</sup> CIN production/identity in the SVZ.

**Lower panel:** Opposing postnatal roles for *Mafb* and *c-Maf* in cortical excitability. In the *Mafb* and *c-Maf* cKO cortices, the numbers of MGE-derived CINs are roughly equal. However, loss of *Mafb* results in CINs that have (1) less post-synaptic densities (\*= showing a decrease trend but didn't reach statistical significance), (2) receive less EPSCs and (3) a cortex that is hyper-responsive to a stimulus, while loss of *c-Maf* results in CINs that have (1) higher neurite complexity, (2) more post-synaptic densities, (3) receive greater EPSCs and (4) a cortex that is hypo-responsive to a stimulus. Notably, cDKO CINs have normal numbers of post-synaptic densities, receive a normal number of EPSCs and have a cortex that responded to a stimulus in a manner in between that of *Mafb* and *c-Maf* single cKOs.

## **Chapter 6: Molecular mechanism downstream of *Mafb* and *c-Maf* regulation in MGE-lineage CIN development and maturation.**

Our data suggest that *Mafb* and *c-Maf* have redundant function prenatally in generating SST and PV CINs, while postnatally, *Mafb* and *c-Maf* have divergent functions in regulating CIN maturation and physiology. To disentangle the roles of *Mafb* and *c-Maf* in the transcriptomic machinery in MGE-derived CIN development, we adopted single-cell RNA-sequencing technique (scRNA-seq) for transcriptomic profiling using P0 WT and cDKO freshly dissociated cortices (hippocampus is included in the dissection).

We pooled the WT and cDKO datasets to perform unsupervised data analysis using Seurat pipeline. We identified 23 different clusters, which includes excitatory neurons, neural progenitors, microglia, MGE and CGE-derived interneurons. The clusters were visualized by t-distributed stochastic neighbor embedding (t-SNE) (Fig. 6.1). We assigned the cell identities to each cluster based on the expression of their established marker genes. Overall, there was no obvious transcriptome changes in the excitatory neurons, neural progenitors, microglia and the CGE-derived CIN population between WT and cDKO. This suggests that the loss of *Mafb* and *c-Maf* in the *Nkx2.1-Cre*-lineage does not have non-cell autonomous effect on other cell types. However, there was a clear separation of the two samples in the assigned MGE-derived CIN population (Fig. 6.1B, boxed region). We further performed differential gene expression analysis in the MGE-derived CIN cluster, and identified 81 differentially expressed genes, with 47 genes upregulated in the cDKO and 34 genes down-regulated in the WT (Fig.6.2). Using gene ontology analysis based upon cellular components, the majority of the dysregulated genes are involved with synapse formation, neurite projection and neuronal maturation, which supports our previous finding that loss of *Mafb* and/or *c-Maf* in the *Nkx2.1-Cre*-lineage leads to defects in synaptogenesis and morphological maturation.



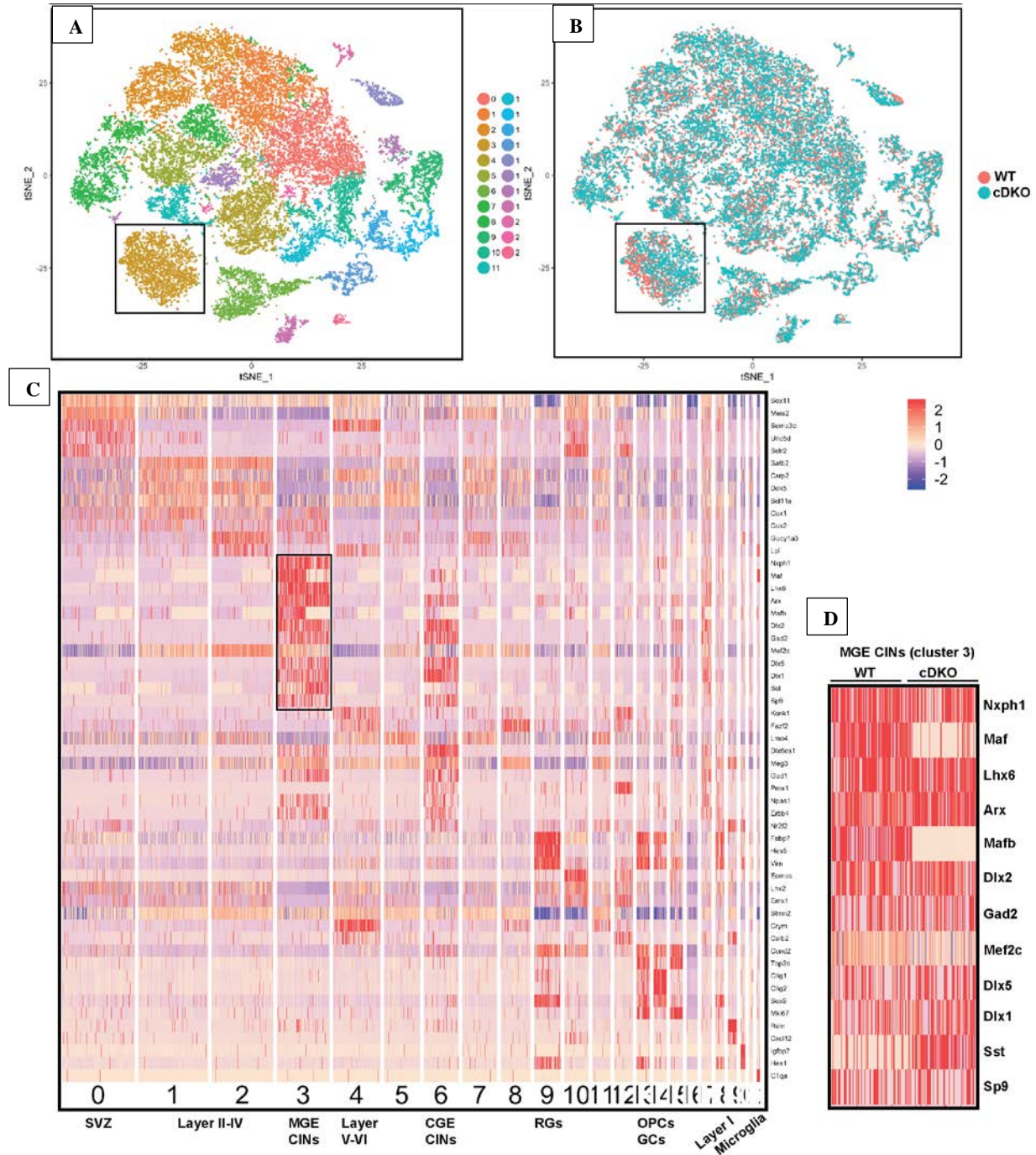


**Fig. 6.1. Single-Cell RNA-seq analysis of P0 WT and cDKO neocortex.** (A) t-SNE plot representing cells from P0 WT and cDKO neocortex, and colored by their cluster assignments. Cells with properties of MGE-derived CINs are in cluster 3 and are boxed in the panel. (B) t-SNE plot representing cells from P0 WT and cDKO neocortex. The clusters were colored based upon genotype. Note that cluster 3 (boxed) has clear separation between WT and cDKO, suggesting CIN property changes after deletion of *Mafb* and *c-Maf* in the *Nkx2.1*-lineage. (C) Heatmap representation of cluster marker genes. (D) Heatmap representation of cluster 3 (enlargement of the boxed region in cluster 3 in (C)). Note reduced expression of *Mafb* and *c-Maf*, and increased expression of *Sst* from the cDKO samples.

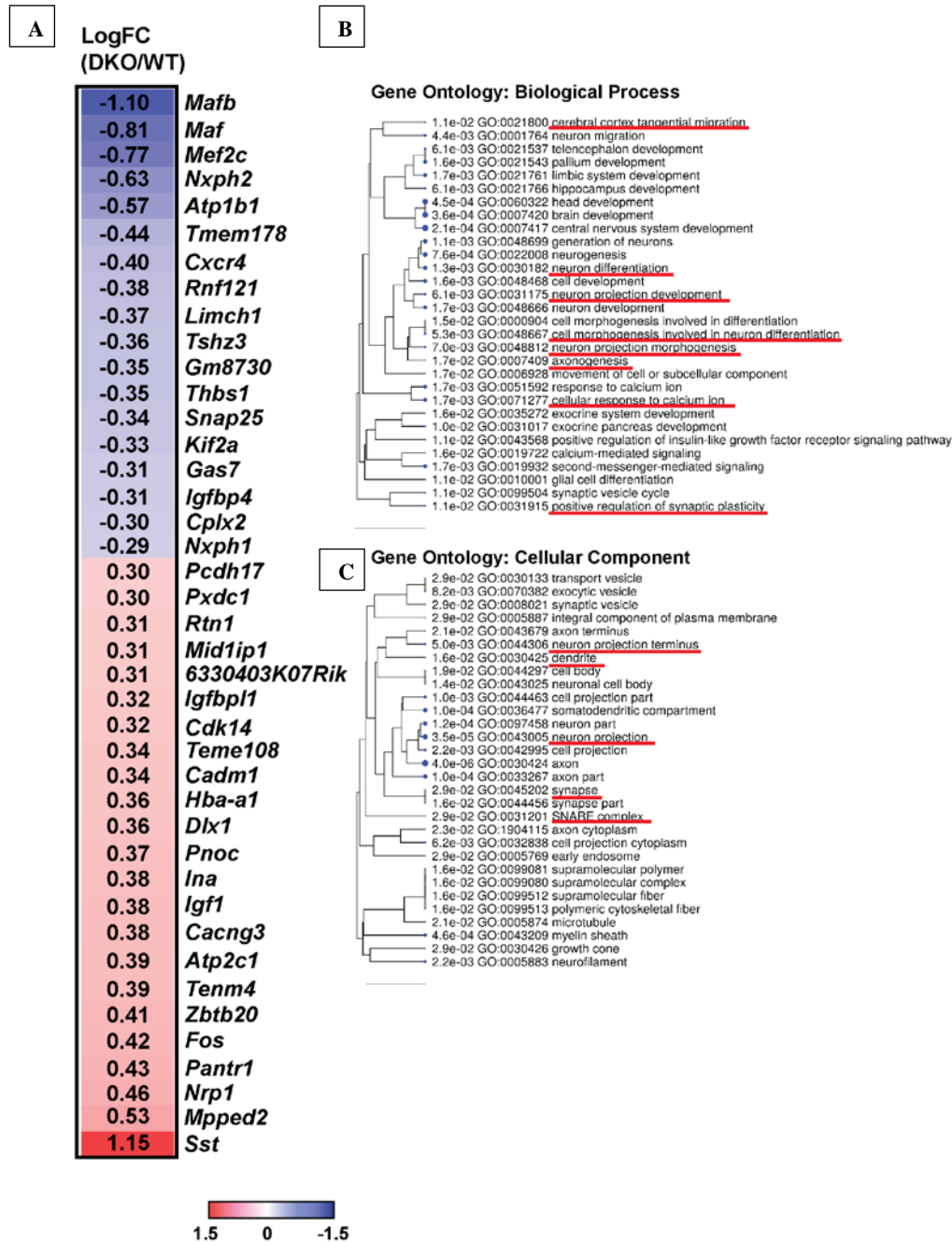


**Fig. 6.2. Representative differentially expressed genes in the cDKO.** (A) Heatmap representation of differentially expressed genes between WT and cDKO based on |LogFC| changes. Blue represents genes down regulated in the cDKOs, and Red represents genes upregulated in the cDKOs. (B-C) Gene ontology analysis on the DE genes based upon their biological processes (B) and their cellular component functions (C).

Previous work has shown that disease genes, such as *Mef2c* (ASD, downregulated) and *Snap25* (schizophrenia, downregulated), promotes neurite outgrowth and synapse formation (Houenou et al., 2017; Tu et al., 2017). We first evaluate if MEF2C is really down-regulated in the *Maf* cDKO using immunohistochemistry. Indeed, *Maf* cDKO has decreased expression of MEF2C in the majority of the *Nkx2.1-Cre*-lineage (tdTomato<sup>+</sup>) (Fig. 6.3). We hypothesized that the decrease expression of *Mef2c* and *Snap25* can account for the *Maf* cDKO neurite outgrowth defect. To evaluate this, we cultured neocortical neurons from WT and *Maf* cDKO animals at P0 (DIV1), transfected *Nkx2.1-Cre*-lineage CINs (tdTomato<sup>+</sup>) with *Dlx1/2b* enhancer driven *gfp*, *c-Maf*, *Mef2c* and *Snap25* expression plasmids, and analyzed CIN morphology at DIV 14. First, *Maf* cDKO CINs transfected with *gfp* alone demonstrated decreased numbers of neurites, suggesting that *gfp* expression does not affect neurite growth. Second, *Maf* cDKO CINs transfected with *c-Maf*, *Mef2c* and *Snap25* expressing plasmids all have increased numbers of neurites comparable to WT counterparts (Fig. 6.4). These results suggest that the expression of *c-Maf*, *Mef2c* and *Snap25* from early postnatal ages can promote neuronal maturation, specifically in dendritic process extension.

Aymé-Gripp syndrome due to *c-Maf* loss of function mutations have manifestations of intellectual disability, seizures, distinctive facial appearance and other symptoms (Niceta et al., 2015), which intersects with interneuronopathy disease symptoms (Marin and Rubenstein, 2001). One possibility could be that the Aymé-Gripp syndrome patients also have interneuron defects. The fact that *c-Maf*, *Mef2c* and *Snap25* expression can rescue the *Maf* cDKO CIN deformity, suggest there is convergence of *c-Maf* regulatory pathway with *Mef2c* and *Snap25* in interneuron development and maturation. Our future work will focus on elucidating the interactions between *c-Maf*, *Mef2c* and *Snap25* on the transcriptome and circuit level to shed light on understanding the pathophysiology of interneuronopathy and interneuron development.

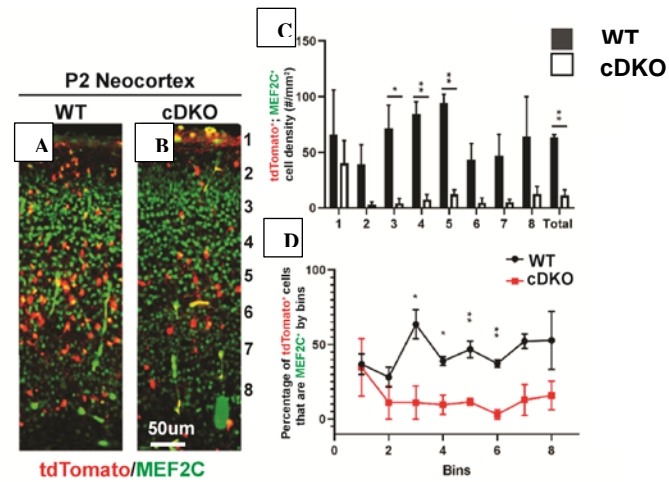


**Fig. 6.3. *Maf* cDKO has decreased expression of *Mef2c*.** (A-B) Immunofluorescence staining of MEF2C and endogenous tdTomato expression at P2 neocortex. (C) Quantification of tdTomato and MEF2C double-labeled cell density by bins. (D) Quantification of the percentage of tdTomato<sup>+</sup> CINs expressing MEF2C by bins. (n)=3 per group. \*p < 0.05; \*\*p < 0.01. Scale bar shown in (B)=50μm.

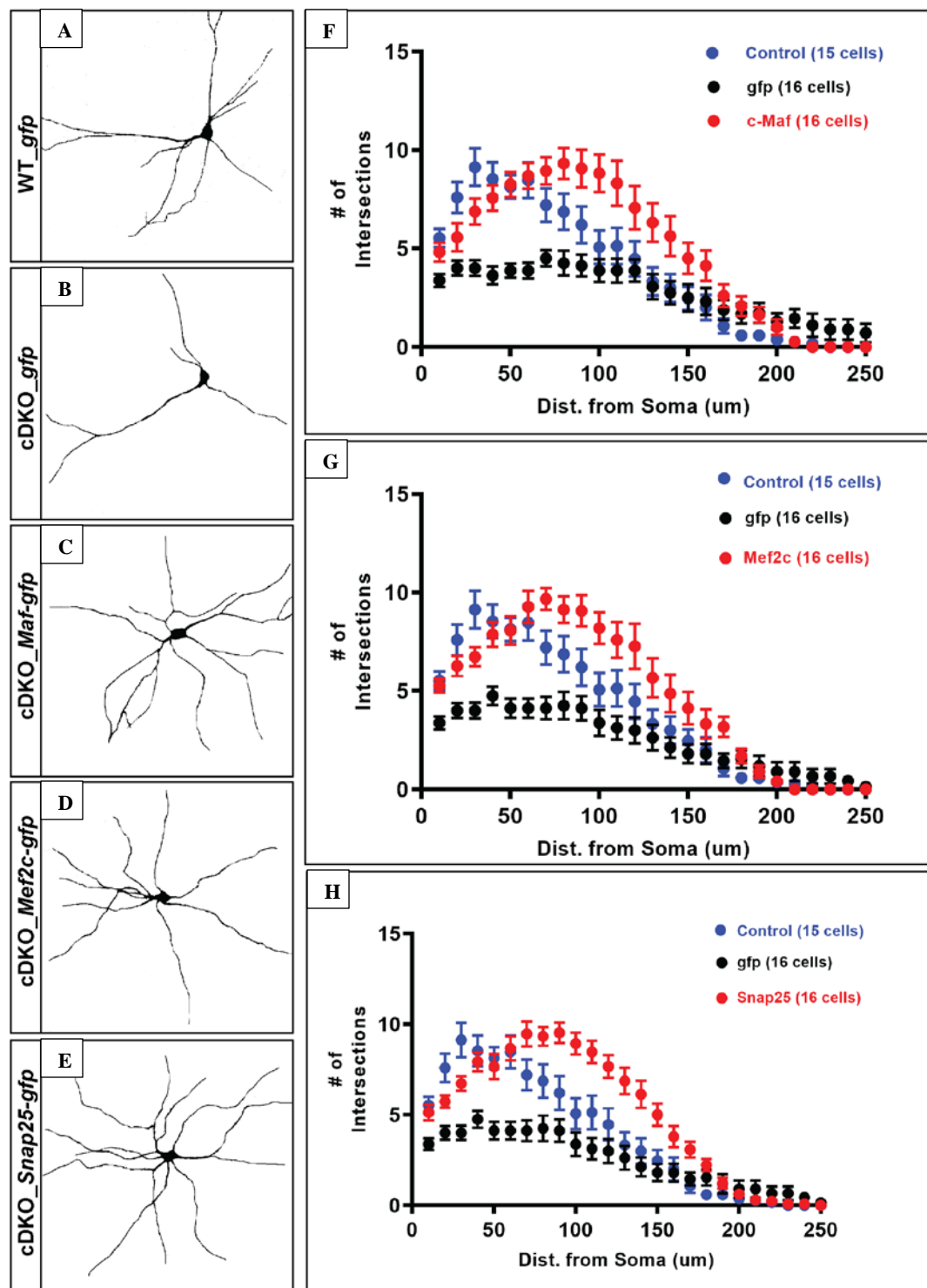


**Fig. 6.4. *Maf* cDKO neurite outgrowth defect can be rescued by expression of *Mef2c* and *Snap25*.** (A) Representative image of cultured CINs from WT co-transfected with *gfp*. (B-E) Representative images of cultured CINs from cDKO co-transfected with *gfp*, *c-Maf*, *Mef2c* and *Snap25* expressing plasmids. (F-H) Sholl analysis on cultured CINS from WT/cDKO treated with *gfp* as control and cDKO treated with *c-Maf*, *Mef2c* and *Snap25*.

## Appendix I: Methods

**Animals:** All procedures and animal care were approved and performed in accordance with the University of California San Francisco Laboratory Animal Research Center (LARC) guidelines. All mice strains have been previously published: *Ai14* Cre-reporter (Madisen et al., 2010), *Nkx2.1-Cre* (Xu et al., 2008), *Ma1b* flox (Yu et al., 2013), *c-Maf* flox (Wende et al., 2012), *799-CreER* (Silberberg et al., 2016) and *Sst-IRES-Cre* (Taniguchi et al., 2011). Mice were back-crossed onto a CD-1 background before analyses. For timed pregnancies, noon on the day of the vaginal plug was counted as embryonic day 0.5. Mouse crosses generated both pure *Ma1b* and *c-Maf* single mutants and those that were hemizygous for the other gene. We did not observe gross phenotypic differences between mice with or without the additional hemizygous allele, and these were combined together for analysis. For *799-CreER* experiments, tamoxifen (5mg/40g) was administered intraperitoneally to activate the *CreER*, at embryonic day 11.5. All analyses included both males and females.

**EdU injections and analysis:** Pregnant mice were pulsed with 5-Ethynyl-2'-Deoxyuridine (EdU), 10mg/ml (Thermo Fisher Scientific E10187), at a dose of 50mg EdU/kg body weight. For MGE S-phase progenitor quantification (EdU pulse), E12.5-E13.5 mice were sacrificed 30 minutes after EdU injection and collected in ice-cold PFA/PBS. For MAFB/c-MAF and EdU colabeling experiments, E12.5 embryos were harvested 1 hr after EdU injection. For pulse-chase experiments, mice or progeny were sacrificed at E15.5 or P35. Embryonic and postnatal brains were collected and fixed overnight in 4% PFA at 4°C, and then sunk in 30% sucrose before embedding in OCT. EdU<sup>+</sup> cells were visualized using standard procedures in the Click-iT EdU plus kit (Thermo Fisher Scientific C10340) that were co-stained with DAPI. For pulse-chase experiments, the same parameters were used, and the only differential factor was the time needed before analysis.

**Immunofluorescence/Immunohistochemistry:** All tissues were fixed with 4% PFA 1-2 hrs (for >P7 tissues) or overnight (< P7 tissues), followed by 30% sucrose cryoprotection. P7, P16 and P35 fixed tissues were sectioned coronally at 40 µm and stained free-floating. All embryonic ages and P0 fixed tissue were sectioned coronally, at 20 µm, and stained on glass slides. P40 transplant tissue was sectioned coronally at 25 µm and stained on glass slides. Immunofluorescent labeling was performed with the following primary antibodies: rabbit anti-Mafb (Sigma HPA005653; 1:500), rabbit anti-c-MAF (Santa Cruz Biotechnology sc-7866; 1:500), rabbit anti-parvalbumin (Swant PV25; 1:200), rat anti-somatostatin (Millipore MAB354; 1:200), goat anti-somatostatin (Santa Cruz Biotechnology sc-7819; 1:100), rabbit anti-VIP (Immunostar 20077; 1:100), rabbit anti-nNOS (Life Technologies 61-7000; 1:200), goat anti-SP8 (Santa Cruz Biotechnology sc-104661; 1:100), mouse anti-Tuj1 (Covance MMS-435P; 1:500), goat anti-MCM2 (Santa Cruz Biotechnology sc-9839; 1:200 (Maslov et al., 2004), rabbit anti-KI67 (Abcam ab15580; 1:500), mouse anti-KI67 (BD Biosciences 550609 ; 1:200), rabbit anti-VGLUT1 (synaptic system 135303; 1:500), rabbit anti-VGAT (synaptic system 131002; 1:200), mouse anti-GEPHRIN (synaptic system 147011; 1:500) and mouse anti-PSD95 (NeuroMab 75-028, clone ID K28/43; 1:500). The appropriate 488, 594 or 647 Alexa-conjugated secondary antibodies (1:500) were from Life Technologies. All primary and secondary antibodies were diluted in PBS containing 2.5% BSA and 0.3% Triton X-100. Sections were cover slipped with Vectashield containing DAPI (Vector labs).

**In situ hybridization:** In situ hybridization was performed as previously described (Silberberg et al., 2016). Probes included *CoupTF2* (M. Tsai), *Cxcr7* (ATCC MGC-18378), *CyclinD2* (A. Malamacci), *Lhx6* (V. Pachnis), *Mafb* (J. Rubenstein), *c-Maf* (J. Rubenstein), *Nkx2.1* (J. Rubenstein), *Sox6* (Open Biosystems, Clone #5269193), *Sp8* (C. Belmonte), *Sst* (T. Lufkin) were used.

To generate the *Mafb* DNA vector and riboprobe, *Mafb* cDNA was PCR amplified from mouse genomic DNA (mixed CD-1; C57BL6J) using the following primers:



5' GAGAGTCGACATGGCCGCGGAGCTGAGC

3' ATATGAGCTCTCACAGAAAGAACTCGGG.

SalI and SacI restriction enzymes sites were introduced (underlined). Next, the *Mafb* PCR product and the vector, pB3.p11 (Addgene # 69577), were digested with SalI and SacI, and then ligated. The *Mafb* RNA anti-sense probe was generated by T3 RNA polymerase from a SalI linearized vector, with the size of the probe ~1kb.

**Fluorescent In situ hybridization (FISH):** Brain tissues used for FISH were all from P2 animals, which were fixed overnight with 4% PFFA, followed by 30% sucrose/PBS cryoprotection until the day of section. Tissues were embedded in OCT and cryosectioned on a cryostat to generate 25um tissue sections.

To generate riboprobes for target genes, cDNAs was PCR amplified from homemade mouse cDNA library synthesized from P0 neocortex using Superscript II. The 5' and 3' primers while containing sequences for cDNA synthesis, also introduced ClaI and XbaI restriction enzymes sites. The PCR products and the vector, pSP73 (Promega Cat # P2221), were digested with ClaI and XbaI, and then ligated using T4 ligase. The RNA anti-sense fluorescein-labeled/Digoxigenin-labeled probe was generated by T7 RNA polymerase (Roche) and Fluorescein labeling kit (Roche)/DIG labeling kit (Roche) from a NdeI linearized vector, with the size of the probe usually between ~600-800bp.

**MGE transplantation:** A detailed protocol for this procedure is available in a methods format (Vogt et al., 2015). We bred male mice homozygous for *Ai14* and were either WT (control), *Mafb*<sup>Flox/Flox</sup>, *c-Mafb*<sup>Flox/Flox</sup> or *Mafb*<sup>Flox/Flox</sup>, *c-Mafb*<sup>Flox/Flox</sup> to females that were *Ai14* negative but WT or homozygous for



each of the corresponding male alleles, respectively. These crosses yielded embryos that were either WT or homozygous for each of the *Maf* alleles. The embryos were collected at E13.5, dissociated and then transduced with a *Dlx12b-Cre* lentivirus (Vogt et al., 2015b, 2017) in DMEM supplemented with 10% Fetal Bovine Serum (FBS) at 37°C and at pH ~7.2 for 30 minutes. This virus deletes the *Maf* genes and activates tdTomato expression from the *Ai14* allele. The cells were then washed several times with DMEM/FBS pelleted. Next, the cells were loaded into the front of a beveled glass needle. P1 WT pups were anesthetized on ice and injected with ~300 nL of cells over 3-5 sites in the right hemisphere. Pups were warmed until able to move and then put back with their mom. They were aged to 40 days and then perfused. Cells were analyzed as described above.

### **Primary neuronal culture for analysis of dendritic arborization (Sholl) and synapses using neonatal**

**cortex:** Primary cortical neuron cultures were prepared as described (Shepherd et al., 2006). Briefly, we bred *Mafb<sup>Flox/Flox</sup>*, *c-Mafb<sup>Flox/Flox</sup>*, *Ai14f<sup>Flox/Flox</sup>* females with *Mafb<sup>Flox/+</sup>*, *c-Mafb<sup>Flox/+</sup>*, *Nkx2-1 Cre<sup>+</sup>* males to generate P0 *Mafb* cKO, *c-Mafb* cKO and cDKOs. Control P0 animals were generated either through the same crossing or through *Ai14f<sup>Flox/Flox</sup>* females bred with *Nkx2-1 Cre<sup>+</sup>* males. tdTomato<sup>+</sup> P0 pups were pre-screened using fluorescence dissection microscope. We also collected some tdTomato<sup>-</sup> P0 pups for cell preparation. Cortical tissues were dissected in cold EBSS, followed by trypsin (Thermo Fisher Scientific 25200056) treatment for 15 minutes at 37°C. Trypsinization was inhibited using 10% FBS containing DMEM. Cells were washed once with DMEM, then resuspended in 10% FBS containing Neuralbasal-A medium (Thermo Fisher Scientific 12348017) with B27 (Thermo Fisher Scientific 17504044). Cell density was quantified using hemocytometer. tdTomato<sup>+</sup> cell preparation was diluted using tdTomato<sup>-</sup> P0 cell preparation roughly at a ratio of 1:10. Cells were plated in poly-D-lysine and laminin coated coverslips (Corning 08-774-385) preloaded in 24-well plates and cultured in 37°C incubator for 14 days. Serum free Neuralbasal-A medium with B27 and Glutamax (Thermo Fisher Scientific 35050061) was used to maintain the cell growth. At day in vitro 14, cell culture medium was removed and replaced with

freshly made 4% PFA for 15min fixation. PFA was washed off several times with 1X PBS followed by regular immunostaining protocol for synapse labeling. (1) For synapse quantification,  $\geq 3$  animals and 25-40 proximal dendrites were analyzed per genotype. Colocalizations were scored if pre- and post-synaptic puncta along tdTomato-labeled proximal dendrites (within 15um from soma) were fully overlapped. We performed a One way ANOVA followed by Turkey's multiple comparisons test. Differences were regarded significant if  $p < 0.05$ . (2) For Sholl analysis,  $\geq 3$  animals and 15-20 neurons were analyzed per genotype. Images were processed and analyzed using FIJI software based on previously described protocol (Ferreira et al., 2014; Martin et al., 2018).

#### **Image acquisition and processing:**

1. Immunohistochemistry images were taken using a CoolSNAP EZ Turbo 1394 digital camera (Photometrics) mounted on a Nikon Eclipse 80i microscope (Nikon Instruments) using NIS Elements acquisition software (Nikon). Images for proliferative markers were taken using Nikon Ti inverted fluorescence microscope with a CSU-W1 large field of view confocal microscope that had 20X and 60X oil objectives to visualize marker colocalization. Brightness and contrast were adjusted, and images merged using FIJI software.
2. Sholl analysis and excitatory synapse images were taken using the Nikon Ti inverted fluorescence microscope with CSU-W1 large field of view confocal. Images for Sholl analysis were taken using 40X oil objective while images for excitatory synapse quantification were taken using a 60X oil objective. Open source micromanager 2.0 beta was used to acquire images. Brightness/contrast adjustment, z-stack image and binary image processing and Sholl analysis were all conducted using the image calculator and Sholl analysis plugins in FIJI software.

### **Single Cell RNA-seq sample and library preparation.**

For single cell dissociation, primary neocortex tissues were dissected, and incubated with a pre-warmed solution of Papain (BrainBits) prepared according to manufacturer's instructions for 15 min at 37°C. After incubation, tissues were washed with DMEM/10% FBS (Thermo Fisher) solution multiple times, followed by gentle trituration. Samples were diluted to approximately 2,000 cells per microliter. Cell concentration was confirmed using CountessII automatic hemocytometer before loading onto 10X genomics single cell preparation following manufacturer's instruction to target 10,000 cell recovery per sample. Library preparation was performed by UCSF Institute of Human Genetics Core (IHG), using 10X Chromium Single 3' Reagent Kits Version 2 (10X Genomics). The library length and concentration were quantified using Bioanalyzer (Agilent) according to manufacturer's protocol. Paired-end sequencing was performed on the Illumina NovaSeq.

### **Processing of sequencing reads**

Raw base call (BCL) files were converted into FASTQ files and demultiplexed to align cells with their own barcodes using Cell Ranger V.2. Transcriptome alignment (mm10), cell filtering, barcode counting, UMI counting as well as matrix data output for downstream clustering and differential expression analyses were also performed using Cell Ranger V.2 following manufacturer's manual. Up to this point, the pipeline was all run by UCSF IHG computational core.

### **Cell clustering, *t*-SNE visualization and marker-gene identification**

A digital gene expression matrix was constructed from the raw sequencing data as described using Cell Ranger. Cells with fewer than 500 UMIs or over 20,000 UMIs were discarded. Downstream analyses were performed with Seurat v.2 (Ref) and the R package (Ref). In brief, genes with very few counts or with high mitochondrial genes were filtered out and the data were log-transformed, and scaled to unit variance and zero mean following Seurat pipeline manual. The top ~1,000 genes with

the highest variance were selected to perform principal component analysis (PCA) for dimensionality reduction. 20 PC components were used to perform Louvain clustering with resolution=1.0 to generate t-SNE plot for cluster visualization. 23 clusters were identified. We then performed FindAllMarker function from Seurat to identify markers for each cluster. Clusters were assigned to known cell types based upon cluster-specific markers. Differentially expressed (DE) genes between WT and cDKO were performed per cluster basis using MarkerComp function. DE genes with adjusted p-value less than 0.05 and  $|\text{LogFC}| > 0.3$  were selected to perform ISH for validation and functional studies.

## **Electrophysiology**

**Slice preparation:** Mice were euthanized with 4% isoflurane, perfused with ice-cold sucrose cutting solution containing 234 mM sucrose, 2.5 mM KCl, 1.25 mM  $\text{NaH}_2\text{PO}_4$ , 10 mM  $\text{MgSO}_4$ , 0.5 mM  $\text{CaCl}_2$ , 26 mM  $\text{NaHCO}_3$ , and 11 mM glucose, equilibrated with 95%  $\text{O}_2$  and 5%  $\text{CO}_2$ , pH 7.4, and decapitated. We prepared 250  $\mu\text{m}$ -thick horizontal thalamic slices containing Somatosensory Barrel Cortex with a Leica VT1200 microtome (Leica Microsystems). We incubated the slices, initially at 32 °C for 1 h and then at 24–26 °C, in artificial cerebro-spinal fluid (ACSF) containing 126 mM NaCl, 2.5 mM KCl, 1.25 mM  $\text{NaH}_2\text{PO}_4$ , 2 mM  $\text{MgCl}_2$ , 2 mM  $\text{CaCl}_2$ , 26 mM  $\text{NaHCO}_3$ , and 10 mM glucose, equilibrated with 95%  $\text{O}_2$  and 5%  $\text{CO}_2$ , pH 7.4 as described in (Clemente-Perez et al., 2017; Paz et al., 2011, 2013).

**Whole-cell patch-clamp electrophysiology:** Recordings were performed as previously described (Clemente-Perez et al., 2017; Paz et al., 2011, 2013). We visually identified interneurons originating from the MGE based on their expression of tdTomato. Neurons were identified by differential contrast optics with a Zeiss (Oberkochen) Axioskop microscope and an infrared video camera. Recording electrodes made of borosilicate glass had a resistance of 2.5–4 M $\Omega$  when filled with intracellular solution. Access resistance was monitored in all the recordings, and cells were included for analysis only if the access resistance was <25 M $\Omega$ . The access resistance was similar in all recordings ( $p > 0.5$ ), suggesting that differences between

genotypes were not due to the quality of the whole-cell patch-clamp recording. Spontaneous excitatory post-synaptic currents (sEPSCs) were recorded in the presence of picrotoxin (50  $\mu$ M, Tocris). For sEPSCs and current-clamp recordings, the internal solution contained 120 mM potassium gluconate, 11 mM KCl, 1 mM  $MgCl_2$ , 1 mM  $CaCl_2$ , 10 mM HEPES, and 1 mM EGTA, pH adjusted to 7.4 with KOH (290 mOsm). Tetrodotoxin 1  $\mu$ M was added to the extracellular solution for miniature EPSC (mEPSC) recordings. The experiments were performed by blinded observers. To test for differences in the sEPSC/mEPSC amplitude, frequency and decay tau data set across genotypes (comparison between group means), we performed a One Way ANOVA Kruskal-Wallis followed by Dunn's multiple comparisons test. Differences were regarded significant if  $p < 0.05$ .

*F-I* plots were generated using a custom MATLAB code. To test for differences in the F-I data set across genotypes (comparison between group means), we performed a regular two-way ANOVA followed by Tukey's post-hoc test for multiple comparisons. Differences were regarded significant if  $p < 0.05$ . For statistical analysis, we included only the current pulses that were presented to all genotypes (within cell type). In addition, we only included cells which were recorded at at least two of the included current pulses. For FS cells, we analyzed responses at current pulses of 20, 60, 100, 140, 180, 220, and 260 pA. For RS cells, we analyzed responses at current pulses of 20, 60, and 100 pA.

**Extracellular cortical local field potential recordings:** Coronal slices (400  $\mu$ m) containing Somatosensory Barrel Cortex were placed in a humidified, oxygenated interface chamber and perfused at a rate of 2 mL/min at 34°C with oxygenated ACSF prepared as described above and supplemented with 300  $\mu$ M glutamine for cellular metabolic support (Clemente-Perez et al., 2017; Paz et al., 2011, 2013). Extracellular LFP recordings were obtained with a 16-channel multi-electrode array (Neuronexus) placed in the Somatosensory Barrel Cortex. The signals were sampled at 24.414 kHz. Signals were amplified at 10,000x and band-pass filtered between 100 Hz and 6 kHz using the RZ5 from Tucker-Davis Technologies (TDT). We delivered electrical stimuli to the internal capsule with a concentric bipolar tungsten electrode (50–100 k $\Omega$ , FHC) and recorded the evoked local field potential (LFP) responses. Stimulations were

repeated 10–30 times in a single recording and an average LFP was calculated. To assess the cortical network excitability, electrical stimulation was delivered in the internal capsule in increasing amplitudes starting from 10  $\mu$ A to 500  $\mu$ A. The experiments were performed by blinded observers.

## QUANTIFICATION AND STATISTICAL ANALYSIS

All bar graphs were shown as mean  $\pm$  SEM. All statistical analyses were performed using Graphpad Prism (version 7) or R-Project 3.1, and a p value of  $< 0.05$  was considered significant. The specific n for each experiment as well as the post-hoc test corrected p-values, can be found in the Results section, in the Figure legends or in supplementary tables.

1. For all cell counts performed for immunohistochemistry and *in situ* hybridization, we used the cell counter plug-in in FIJI software. For statistical analyses, we used two methods depending on whether data were parametric or nonparametric in distribution. For parametric data, we utilized a two-tailed T-test or one-way ANOVA, followed by a Tukey's post-hoc test, depending on the number of samples being compared. For any data that was normalized (i.e. cell transplants normalized to total cells transplanted or cell fate analyses where proportions were calculated) we used the non-parametric Chi-square test.

2. For LFP analysis: From an average of responses for each slice and intensity, we calculated line length L as the sum of the absolute differences between successive points in a 30 ms signal s just after the stimulation as  $L = \sum_{i=1}^N |s[i-1] - s[i]|$ , similar to (Esteller et al., 2001). The average amplitude was calculated as the absolute difference between the minimum and maximum of the signal as  $|\max(s) - \min(s)|$  from a similar window. Current source densities (CSDs) were computed as the negative of the second difference across channels divided by the square of a nominal spatial differentiation grid g as:  $CSD = -d(d(S))/g$ , where S is a matrix with each row a signal for an individual channel like,

$S = ( \begin{matrix} s_{1,1} & s_{1,2} & s_{1,3} & \dots & s_{1,N} & s_{2,1} & s_{2,2} & s_{2,3} & \dots & s_{2,N} & \dots & s_{16,1} & s_{16,2} & s_{16,3} & \dots & s_{16,N} \end{matrix} )$ , and  $d(\cdot)$  is the first difference operator computed by column. For more theory see (Hodgkin and Huxley, 1952).

Numerical values are given as mean  $\pm$  SEM unless stated otherwise. 6 Controls, 7 *Mafb* cKOs, 6 *c-Maf* cKOs and 3 cDKOs were used. For statistical analyses, we used parametric and nonparametric tests. We assessed statistical significance, as appropriate, by performing two-way ANOVA and the Kolmogoroff-Smirnoff test using R-Project 3.1.

## **Appendix II: References**

- Anderson, S.A., Eisenstat, D.D., Shi, L., and Rubenstein, J.L.R. (1997). Interneuron migration from basal forebrain to neocortex. *Science* (80-. ). 278, 474–476.
- Blanchi, B., Kelly, L.M., Viemari, J.-C., Lafon, I., Burnet, H., Bévengut, M., Tillmanns, S., Daniel, L., Graf, T., Hilaire, G., et al. (2003). MafB deficiency causes defective respiratory rhythmogenesis and fatal central apnea at birth. *Nat. Neurosci.* 6, 1091–1100.
- Blank, V., and Andrews, N.C. (1997). The Maf transcription factors: Regulators of differentiation. *Trends Biochem. Sci.* 22, 437–441.
- Cavanagh, M.E., and Parnavelas, J.G. (1988). Development of somatostatin immunoreactive neurons in the rat occipital cortex: A combined immunocytochemical autoradiographic study. *J. Comp. Neurol.* 268, 1–12.
- Chao, H.-T., Chen, H., Samaco, R.C., Xue, M., Chahrour, M., Yoo, J., Neul, J.L., Gong, S., Lu, H.-C., Heintz, N., et al. (2010). Dysfunction in GABA signalling mediates autism-like stereotypies and Rett syndrome phenotypes. *Nature* 468, 263–269.
- Chen, Y.-J.J., Friedman, B.A., Ha, C., Durinck, S., Liu, J., Rubenstein, J.L., Seshagiri, S., and Modrusan, Z. (2017). Single-cell RNA sequencing identifies distinct mouse medial ganglionic eminence cell types. *Sci. Rep.* 7, 45656.
- Clemente-Perez, A., Makinson, S.R., Higashikubo, B., Brovarney, S., Cho, F.S., Urry, A., Holden, S.S., Wimer, M., Dávid, C., Fenno, L.E., et al. (2017). Distinct Thalamic Reticular Cell Types Differentially Modulate Normal and Pathological Cortical Rhythms. *Cell Rep.*
- Cobos, I., Long, J.E., Thwin, M.T., and Rubenstein, J.L. (2006). Cellular patterns of transcription factor expression in developing cortical interneurons. *Cereb.Cortex* 16 Suppl 1, i82–i88.
- Cordes, S.P., and Barsh, G.S. (1994). The mouse segmentation gene *kr* encodes a novel basic domain-



leucine zipper transcription factor. *Cell* 79, 1025–1034.

Esteller, R., Echauz, J., Tchong, T., Litt, B., and Pless, B. (2001). Line length: An efficient feature for seizure onset detection. *Annu. Int. Conf. IEEE Eng. Med. Biol.*

Ferreira, T.A., Blackman, A. V., Oyrer, J., Jayabal, S., Chung, A.J., Watt, A.J., Sjöström, P.J., and Van Meyel, D.J. (2014). Neuronal morphometry directly from bitmap images. *Nat. Methods*.

Gelman, D., Griveau, A., Dehorter, N., Teissier, A., Varela, C., Pla, R., Pierani, A., and Marin, O. (2011). A wide diversity of cortical GABAergic interneurons derives from the embryonic preoptic area. *J Neurosci* 31, 16570–16580.

Han, S., Tai, C., Westenbroek, R.E., Yu, F.H., Cheah, C.S., Potter, G.B., Rubenstein, J.L., Scheuer, T., de la Iglesia, H.O., and Catterall, W.A. (2012). Autistic-like behaviour in *Scn1a*<sup>+/-</sup> mice and rescue by enhanced GABA-mediated neurotransmission. *Nature* 489, 385–390.

Hodgkin, A.L., and Huxley, A.F. (1952). A Quantitative Description of Membrane Current and its Application to Conduction and Excitation in Nerves. *J. Physiol.*

Houenou, J., Boisgontier, J., Henrion, A., d’Albis, M.-A., Dumaine, A., Linke, J., Wessa, M., Daban, C., Hamdani, N., Delavest, M., et al. (2017). A Multilevel Functional Study of a SNAP25 At-Risk Variant for Bipolar Disorder and Schizophrenia . *J. Neurosci.*

Hu, J.S., Vogt, D., Sandberg, M., and Rubenstein, J.L. (2017). Cortical interneuron development: a tale of time and space. *Development* 144, 3867–3878.

Huang, Z.J., Di Cristo, G., and Ango, F. (2007). Development of GABA innervation in the cerebral and cerebellar cortices. *Nat. Rev. Neurosci.* 8, 673–686.

Inan, M., Welagen, J., and Anderson, S.A. (2012). Spatial and temporal bias in the mitotic origins of somatostatin- and parvalbumin-expressing interneuron subgroups and the chandelier subtype in the medial ganglionic eminence. *Cereb. Cortex* 22, 820–827.

Kataoka, K. (2007). Multiple mechanisms and functions of Maf transcription factors in the regulation of tissue-specific genes. *J. Biochem.* *141*, 775–781.

Kawauchi, S., Takahashi, S., Nakajima, O., Ogino, H., Morita, M., Nishizawa, M., Yasuda, K., and Yamamoto, M. (1999). Regulation of lens fiber cell differentiation by transcription factor c- Maf. *J. Biol. Chem.* *274*, 19254–19260.

Kepecs, A., and Fishell, G. (2014). Interneuron cell types are fit to function. *Nature* *505*, 318–326.

Kessaris, N., Magno, L., Rubin, A.N., and Oliveira, M.G. (2014). Genetic programs controlling cortical interneuron fate. *Curr. Opin. Neurobiol.* *26*, 79–87.

Li, G., Adesnik, H., Li, J., Long, J., Nicoll, R.A., Rubenstein, J.L.R., and Pleasure, S.J. (2008). Regional distribution of cortical interneurons and development of inhibitory tone are regulated by Cxcl12/Cxcr4 signaling. *J. Neurosci.* *28*, 1085–1098.

Lim, L., Mi, D., Llorca, A., and Marín, O. (2018a). Development and Functional Diversification of Cortical Interneurons. *Neuron*.

Lim, L., Pakan, J.M.P., Selten, M.M., Marques-Smith, A., Llorca, A., Bae, S.E., Rochefort, N.L., and Marín, O. (2018b). Optimization of interneuron function by direct coupling of cell migration and axonal targeting. *Nat. Neurosci.*

Lopez-Pajares, V., Qu, K., Zhang, J., Webster, D.E., Barajas, B.C., Siprashvili, Z., Zarnegar, B.J., Boxer, L.D., Rios, E.J., Tao, S., et al. (2015). A LncRNA-MAF:MAFB transcription factor network regulates epidermal differentiation. *Dev. Cell* *32*, 693–706.

Lu, C.C., Appler, J.M., Houseman, E.A., and Goodrich, L. V. (2011). Developmental Profiling of Spiral Ganglion Neurons Reveals Insights into Auditory Circuit Assembly. *J. Neurosci.* *31*, 10903–10918.

Madisen, L., Zwingman, T.A., Sunkin, S.M., Oh, S.W., Zariwala, H.A., Gu, H., Ng, L.L., Palmiter, R.D., Hawrylycz, M.J., Jones, A.R., et al. (2010). A robust and high-throughput Cre reporting and

characterization system for the whole mouse brain. *Nat. Neurosci.* 13, 133–140.

Martin, P.M., Stanley, R.E., Ross, A.P., Freitas, A.E., Moyer, C.E., Brumback, A.C., Iafrati, J., Stapornwongkul, K.S., Dominguez, S., Kivimäe, S., et al. (2018). DIXDC1 contributes to psychiatric susceptibility by regulating dendritic spine and glutamatergic synapse density via GSK3 and Wnt/ $\beta$ -catenin signaling. *Mol. Psychiatry*.

McKinsey, G.L., Lindtner, S., Trzcinski, B., Visel, A., Pennacchio, L.A., Huylebroeck, D., Higashi, Y., and Rubenstein, J.L.R. (2013). *Dlx1&2-Dependent Expression of Zfhx1b (Sip1, Zeb2) Regulates the Fate Switch between Cortical and Striatal Interneurons.* *Neuron* 77, 83–98.

Mi, D., Li, Z., Lim, L., Li, M., Moissidis, M., Yang, Y., Gao, T., Hu, T.X., Pratt, T., Price, D.J., et al. (2018). Early emergence of cortical interneuron diversity in the mouse embryo. *Science* (80-. ). 1–9.

Miyoshi, G., Butt, S.J.B., Takebayashi, H., and Fishell, G. (2007). Physiologically distinct temporal cohorts of cortical interneurons arise from telencephalic *Olig2*-expressing precursors. *J. Neurosci.* 27, 7786–7798.

Niceta, M., Stellacci, E., Gripp, K.W., Zampino, G., Kousi, M., Anselmi, M., Traversa, A., Ciolfi, A., Stabley, D., Bruselles, A., et al. (2015). Mutations impairing GSK3-mediated MAF phosphorylation cause cataract, deafness, intellectual disability, seizures, and a down syndrome-like facies. *Am. J. Hum. Genet.*

Nishikawa, K., Nakashima, T., Takeda, S., Isogai, M., Hamada, M., Kimura, A., Kodama, T., Yamaguchi, A., Owen, M.J., Takahashi, S., et al. (2010). Maf promotes osteoblast differentiation in mice by mediating the age-related switch in mesenchymal cell differentiation. *J. Clin. Invest.* 120, 3455–3465.

Nishimura, W., Kondo, T., Salameh, T., El Khattabi, I., Dodge, R., Bonner-Weir, S., and Sharma, A. (2006). A switch from MafB to MafA expression accompanies differentiation to pancreatic  $\beta$ -cells. *Dev. Biol.* 293, 526–539.

- Paul, A., Crow, M., Raudales, R., He, M., Gillis, J., and Huang, Z.J. (2017). Transcriptional Architecture of Synaptic Communication Delineates GABAergic Neuron Identity. *Cell* 171, 522-539.e20.
- Paz, J.T., Bryant, A.S., Peng, K., Fenno, L., Yizhar, O., Frankel, W.N., Deisseroth, K., and Huguenard, J.R. (2011). A new mode of corticothalamic transmission revealed in the *Gria4*  $-/-$  model of absence epilepsy. *Nat. Neurosci.*
- Paz, J.T., Davidson, T.J., Frechette, E.S., Delord, B., Parada, I., Peng, K., Deisseroth, K., and Huguenard, J.R. (2013). Closed-loop optogenetic control of thalamus as a tool for interrupting seizures after cortical injury. *Nat. Neurosci.*
- Petros, T.J., Bultje, R.S., Ross, M.E., Fishell, G., and Anderson, S.A. (2015). Apical versus Basal Neurogenesis Directs Cortical Interneuron Subclass Fate. *Cell Rep.* 13, 1090–1095.
- Petryniak, M.A., Potter, G.B., Rowitch, D.H., and Rubenstein, J.L.R. (2007). *Dlx1* and *Dlx2* Control Neuronal versus Oligodendroglial Cell Fate Acquisition in the Developing Forebrain. *Neuron*.
- Pla, R., Borrell, V., Flames, N., and Marín, O. (2006). Layer acquisition by cortical GABAergic interneurons is independent of Reelin signaling. *J. Neurosci.* 26, 6924–6934.
- Rubenstein, J.L.R., and Merzenich, M.M. (2003). Model of autism: increased ratio of excitation/inhibition in key neural systems. *Genes. Brain. Behav.* 2, 255–267.
- Sánchez-Alcañiz, J.A., Haege, S., Mueller, W., Pla, R., Mackay, F., Schulz, S., López-Bendito, G., Stumm, R., and Marín, O. (2011). *Cxcr7* Controls Neuronal Migration by Regulating Chemokine Responsiveness. *Neuron* 69, 77–90.
- Sarrazin, S., Mossadegh-Keller, N., Fukao, T., Aziz, A., Mourcin, F., Vanhille, L., Kelly Modis, L., Kastner, P., Chan, S., Duprez, E., et al. (2009). *MafB* Restricts M-CSF-Dependent Myeloid Commitment Divisions of Hematopoietic Stem Cells. *Cell* 138, 300–313.
- Shekhar, K., Lapan, S.W., Whitney, I.E., Tran, N.M., Macosko, E.Z., Kowalczyk, M., Adiconis, X.,

- Levin, J.Z., Nemesh, J., Goldman, M., et al. (2016). Comprehensive Classification of Retinal Bipolar Neurons by Single-Cell Transcriptomics. *Cell*.
- Silberberg, S.N., Taher, L., Lindtner, S., Sandberg, M., Nord, A.S., Vogt, D., McKinsey, G.L., Hoch, R., Pattabiraman, K., Zhang, D., et al. (2016). Subpallial Enhancer Transgenic Lines: a Data and Tool Resource to Study Transcriptional Regulation of GABAergic Cell Fate. *Neuron* 92, 59–74.
- Sohal, V.S., and Rubenstein, J.L.R. (2019). Excitation-inhibition balance as a framework for investigating mechanisms in neuropsychiatric disorders. *Mol. Psychiatry*.
- Soucie, E.L., Weng, Z., Geirsdottir, L., Molawi, K., Maurizio, J., Fenouil, R., Mossadegh-Keller, N., Gimenez, G., VanHille, L., Beniazza, M., et al. (2016). Lineage-specific enhancers activate self-renewal genes in macrophages and embryonic stem cells. *Science* (80-. ). 351, aad5510.
- Stumm, R.K., Zhou, C., Ara, T., Lazarini, F., Dubois-Dalcq, M., Nagasawa, T., Höllt, V., and Schulz, S. (2003). CXCR4 regulates interneuron migration in the developing neocortex. *J. Neurosci.* 23, 5123–5130.
- Sussel, L., Marin, O., Kimura, S., and Rubenstein, J.L. (1999). Loss of Nkx2.1 homeobox gene function results in a ventral to dorsal molecular respecification within the basal telencephalon: evidence for a transformation of the pallidum into the striatum. *Development* 126, 3359–3370.
- Takahashi, T., Nowakowski, R.S., and Caviness, V.S. (1996). The leaving or Q fraction of the murine cerebral proliferative epithelium: a general model of neocortical neuronogenesis. *J. Neurosci.* 16, 6183–6196.
- Taniguchi, H., He, M., Wu, P., Kim, S., Paik, R., Sugino, K., Kvitsani, D., Fu, Y., Lu, J., Lin, Y., et al. (2011). A Resource of Cre Driver Lines for Genetic Targeting of GABAergic Neurons in Cerebral Cortex. *Neuron* 71, 995–1013.
- Tu, S., Akhtar, M.W., Escorihuela, R.M., Amador-Arjona, A., Swarup, V., Parker, J., Zaremba, J.D., Holland, T., Bansal, N., Holohan, D.R., et al. (2017). NitroSynapsin therapy for a mouse MEF2C

haploinsufficiency model of human autism. *Nat. Commun.*

Vogt, D., Wu, P.-R., Sorrells, S.F., Arnold, C., Alvarez-Buylla, A., and Rubenstein, J.L.R. (2015). Viral-mediated Labeling and Transplantation of Medial Ganglionic Eminence (MGE) Cells for In Vivo Studies. *J. Vis. Exp.* e52740.

Wang, Y., Li, G., Stanco, A., Long, J.E., Crawford, D., Potter, G.B., Pleasure, S.J., Behrens, T., and Rubenstein, J.L.R. (2011). CXCR4 and CXCR7 have distinct functions in regulating interneuron migration. *Neuron* 69, 61–76.

Wende, H., Lechner, S.G., Cheret, C., Bourane, S., Kolanczyk, M.E., Pattyn, A., Reuter, K., Munier, F.L., Carroll, P., Lewin, G.R., et al. (2012). The Transcription Factor c-Maf Controls Touch Receptor Development and Function. *Science* (80-. ). 335, 1373–1376.

Wonders, C.P., and Anderson, S.A. (2006). The origin and specification of cortical interneurons. *Nat. Rev. Neurosci.* 7, 687–696.

Xu, Q., Tam, M., and Anderson, S.A. (2008). Fate mapping Nkx2.1-lineage cells in the mouse telencephalon. *J. Comp. Neurol.* 506, 16–29.

Yizhar, O., Fenno, L.E., Prigge, M., Schneider, F., Davidson, T.J., O’Shea, D.J., Sohal, V.S., Goshen, I., Finkelstein, J., Paz, J.T., et al. (2011). Neocortical excitation/inhibition balance in information processing and social dysfunction. *Nature* 477, 171–178.

Yu, W.M., Appler, J.M., Kim, Y.H., Nishitani, A.M., Holt, J.R., and Goodrich, L. V. (2013). A Gata3-Mafb transcriptional network directs post-synaptic differentiation in synapses specialized for hearing. *Elife* 2, e01341.

Zhao, Y., Flandin, P., Long, J.E., Dela Cuesta, M., Westphal, H., and Rubenstein, J.L.R. (2008). Distinct molecular pathways of development of telencephalic interneuron subtypes revealed through analysis of Lhx6 mutants. *J. Comp. Neurol.* 510, 79–99.

### Appendix III: Compilation of Supplementary tables

**Table S1. Genetic markers for single cell clusters (see separate files)**

**Table S2. Cumulative cell counts of *Nkx2.1-Cre*-lineage cells in the neocortex and hippocampus**

	P35	Control	<i>Mafb</i> cKO	<i>c-Maf</i> cKO	<i>Maf</i> cDKO
	Tissue	Total <i>Nkx2.1-Cre</i> -lineage cells/mm <sup>2</sup> ± SEM			
	Hippocampus	266.1 ± 13.8	250.5 ± 5.2	257.5 ± 14.3	** 195.9 ± 8.2
	Neocortex	260.8 ± 10.1	** 194.5 ± 12.8	*** 176.7 ± 6.9	**** 87.2 ± 6.4
	Striatum	333.7 ± 9.8	* 298.4 ± 3.3	307.1 ± 6.3	*** 269.7 ± 7.0
Marker	Tissue	Total <i>Nkx2.1-Cre</i> -lineage <sup>+</sup> /marker <sup>+</sup> cells/mm <sup>2</sup> ± SEM			
PV	Hippocampus	73.7 ± 3.1	68.1 ± 3.5	73.1 ± 8.3	*** 26.0 ± 3.4
	Neocortex	113.0 ± 9.5	* 76.3 ± 3.7 (32.5% decrease)	* 77.1 ± 6.3 (32% decrease)	*** 24.6 ± 6.5 (78.2% decrease)
	Striatum	73.4 ± 4.7	*** 38.1 ± 3.9	*** 44.0 ± 4.8	**** 7.6 ± 2.2
SST	Hippocampus	46.9 ± 9.5	50.7 ± 4.7	49.4 ± 9.9	26.1 ± 3.4
	Neocortex	101.5 ± 8.8	89.1 ± 7.4 (12% decrease)	* 72.0 ± 5.0 (29% decrease)	*** 31.0 ± 3.4 (69% decrease)
	Striatum	35.9 ± 2.5	32.4 ± 2.2	34.8 ± 2.2	34.2 ± 2.2
Marker	Tissue	% <i>Nkx2.1-Cre</i> -lineage cells that express marker ± SEM			
PV	Hippocampus	28.4 ± 1.6	28.7 ± 0.7	29.5 ± 2.3	*** 14.5 ± 1.4
	Neocortex	41.2 ± 1.7	39.7 ± 1.8	44.5 ± 0.8	*** 25.2 ± 3.4
	Striatum	22.7 ± 1.8	*** 12.6 ± 1.3	** 14.0 ± 1.3	*** 2.8 ± 0.8
SST	Hippocampus	17.9 ± 0.6	23.3 ± 2.3	21.8 ± 4.2	14.2 ± 2.2
	Neocortex	36.2 ± 1.8	41.1 ± 1.9	37.5 ± 0.5	38.1 ± 4.2
	Striatum	10.7 ± 0.9	11.1 ± 0.8	11.5 ± 0.7	12.6 ± 0.3

	Control	<i>Mafb</i> cKO	<i>c-Maf</i> cKO	<i>Maf</i> cDKO
Tissue	Total <i>Nkx2.1-Cre</i> -lineage cells/mm <sup>2</sup> ± SEM			
P7 Hippocampus	369.95 ± 8.16	* 258.88 ± 17.03	349.55 ± 20.1	398.86 ± 26.46
P16 Hippocampus	266.06 ± 13.76	250.48 ± 5.21	257.54 ± 14.31	* 195.86 ± 8.24

*p* value \* < 0.05, \*\* < 0.01, \*\*\* < 0.001, \*\*\*\* < 0.0001 compared to control group

**(Top)** Quantification of the numbers of *Nkx2.1-Cre*<sup>+</sup> cells from all genotypes at P35.

**(Bottom)** Quantification of the numbers of *Nkx2.1-Cre*<sup>+</sup> cells from all genotypes in the hippocampus at P7 and P16. Panels at the top show both proportion and cell density of tdTomato<sup>+</sup> cells that express SST or PV in the somatosensory cortex and hippocampus. Panels at the bottom show the tdTomato<sup>+</sup> cell

density count in the whole hippocampus (including DG, CA1 and CA2/3). Data are expressed as the mean  $\pm$  SEM. \* $p < 0.05$ , \*\* $p < 0.01$ , \*\*\* $p < 0.001$ , \*\*\*\* $p < 0.0001$ .



**Table S3. Passive and Active electric membrane properties of layer V CINs**

Passive electric membrane properties						
Cell Type	Genotype	V <sub>m</sub> (mV)	R <sub>in</sub> (MΩ)	τ <sub>m</sub> (ms)	C <sub>m</sub> (pF)	# of cells
FS	Control	-69.4 ± 1.7 (27)	268.7 ± 33.7 (18)	18.1 ± 1.8 (17)	45.3 ± 4.5 (18)	27
	<i>Maifb</i> cKO	-67.6 ± 1.5 (26)	278.7 ± 25.8 (25)	21.4 ± 1.6 (24)	41.5 ± 2.9 (18)	26
	<i>c-Maf</i> cKO	-70.2 ± 1.1 (41)	252.3 ± 22.2 (38)	19.8 ± 1.1 (37)	36.9 ± 3.6 (37)	41
	cDKO	-71.3 ± 1.8 (8)	225.5 ± 50.4 (9)	19.9 ± 2.4 (9)	33.0 ± 6.3 (10)	8
	Statistics	ns	ns	ns	ns	
RS	Control	-70.1 ± 1.3 (16)	528.6 ± 34.9 (7)	34.0 ± 4.3 (7)	45.1 ± 3.8 (7)	16
	<i>Maifb</i> cKO	-62.4 ± 2.8 (11)	320.2 ± 43.3c(11)	23.2 ± 2.6 (11)	48.1 ± 4.8 (11)	11
	<i>c-Maf</i> cKO	-72.0 ± 1.5 (19)	570.5 ± 108.9 (8)	37.0 ± 8.0 (8)	32.0 ± 4.1 (11)	19
	cDKO	-72.0 ± 3.4 (6)	238.7 ± 46.8 (5)	24.6 ± 4.0 (5)	58.1 ± 9.3 (7)	6
	Statistics	p=0.01 (Control vs <i>Maifb</i> cKO) p= 0.003 ( <i>Maifb</i> cKO vs <i>c-Maf</i> cKO)	p=0.004 (Control vs <i>Maifb</i> cKO) p=0.0005 (Control vs cDKO) p=0.03 ( <i>Maifb</i> cKO vs <i>c-Maf</i> cKO) p=0.04 ( <i>c-Maf</i> cKO vs cDKO)	p=0.036 (Control vs <i>Maifb</i> cKO)	p=0.04 (Control vs <i>c-Maf</i> cKO) p=0.018 ( <i>Maifb</i> cKO vs <i>c-Maf</i> cKO) p=0.01 ( <i>c-Maf</i> cKO vs cDKO)	

Active electric membrane properties						
Cell Type	Genotype	AP threshold (mV)	AP amplitude (mV)	AP Full-duration (ms)	AP Half-duration (ms)	# of cells
FS	Control	-55.8 ± 0.9	58.5 ± 2.3	1.4 ± 0.1	0.7 ± 0.05	19
	<i>Maifb</i> cKO	-57.9 ± 0.8	65.8 ± 2.3	1.6 ± 0.1	0.7 ± 0.03	24
	<i>c-Maf</i> cKO	-54.2 ± 0.7	60.1 ± 1.3	1.4 ± 0.1	0.6 ± 0.03	38
	cDKO	-54.97 ± 1.1	60.8 ± 2.0	1.5 ± 0.1	0.6 ± 0.04	9
	Statistics	p=0.001 ( <i>Maifb</i> cKO vs <i>c-Maf</i> cKO) p=0.049 ( <i>Maifb</i> cKO vs cDKO)	p=0.03 (Control vs <i>Maifb</i> cKO) p=0.025 ( <i>Maifb</i> cKO vs <i>c-Maf</i> cKO)	p=0.04 ( <i>Maifb</i> cKO vs <i>c-Maf</i> cKO)	p=0.02 ( <i>Maifb</i> cKO vs <i>c-Maf</i> cKO) p=0.047 ( <i>Maifb</i> cKO vs cDKO)	
RS	Control	-58.2 ± 0.8	59.7 ± 5.2	2.4 ± 0.3	1.1 ± 0.09	5
	<i>Maifb</i> cKO	-54.9 ± 1.2	56.1 ± 4.4	2.2 ± 0.3	0.9 ± 0.09	8
	<i>c-Maf</i> cKO	-53.9 ± 1.2	49.4 ± 2.7	2.3 ± 0.3	0.9 ± 0.1	8
	cDKO	55.7 ± 4.5	45.7 ± 7.3	2.1 ± 0.1	0.8 ± 0.04	3
	Statistics	p=0.02 (Control vs <i>c-Maf</i> cKO)	ns	ns	ns	

Quantification of the numbers of passive (**Top**) and active (**Bottom**) electric membrane properties of fast-spiking (FS) and regular-spiking (RS) CINs in Control, *Maifb* cKO, *c-Maf* cKO and cDKO. Data are expressed as the mean ± SEM.

**Table S4. Properties of spontaneous excitatory post-synaptic currents (sEPSCs) of layer V CINs for all groups and mEPSCs of layer V CINs for Control and *Mafb* cKO**

sEPSCs					
Cell Type	Genotype	Amplitude (pA)	Decay $\tau$ (ms)	Frequency (Hz)	# of cells
FS	Control	23.9 $\pm$ 1.9	1.2 $\pm$ 0.2	8.4 $\pm$ 1.8	13
	<i>Mafb</i> cKO	17.4 $\pm$ 0.6	1.2 $\pm$ 0.1	6.8 $\pm$ 1.5	24
	<i>c-Maf</i> cKO	20.9 $\pm$ 0.8	1.0 $\pm$ 0.1	16.6 $\pm$ 3.2	33
	cDKO	23.2 $\pm$ 2.5	1.4 $\pm$ 0.2	9.4 $\pm$ 3.4	7
	Statistics	p=0.0004 (Control vs <i>Mafb</i> cKO) p=0.002 ( <i>Mafb</i> cKO vs <i>c-Maf</i> cKO) p=0.002 ( <i>Mafb</i> cKO vs cDKO)	p=0.03 ( <i>c-Maf</i> cKO vs cDKO)	p=0.015 ( <i>Mafb</i> cKO vs <i>c-Maf</i> cKO)	
RS	Control	17.4 $\pm$ 1.2	2.0 $\pm$ 0.4	1.2 $\pm$ 0.7	7
	<i>Mafb</i> cKO	18.1 $\pm$ 1.1	1.7 $\pm$ 0.3	8.6 $\pm$ 2.4	11
	<i>c-Maf</i> cKO	17.7 $\pm$ 1.3	1.4 $\pm$ 0.3	12.2 $\pm$ 4.8	6
	cDKO	16.7 $\pm$ 1.2	2.7 $\pm$ 0.7	0.8 $\pm$ 0.2	4
	Statistics	ns (p>0.1)	ns (p>0.1)	p=0.029 (Control vs <i>Mafb</i> cKO) p=0.03 (Control vs <i>c-Maf</i> cKO)	

mEPSCs				
Measurement	Unit	Control	<i>Mafb</i> cKO	Statistics
Frequency	Hz	3.785 $\pm$ 0.7408	8.789 $\pm$ 2.748	Ns
Amplitude	pA	18.32 $\pm$ 0.963	12.54 $\pm$ 0.4074	P<0.0001
Charge	fC	32.56 $\pm$ 3.667	23.29 $\pm$ 3.299	P<0.01
Tau Decay	ms	1.588 $\pm$ 0.1679	1.973 $\pm$ 0.2371	ns
Rise Time	ms	0.2996 $\pm$ 0.009	0.326 $\pm$ 0.01389	ns
Half-width		1.996 $\pm$ 0.2647	2.252 $\pm$ 0.3733	ns
Number of cells		24	19	
Number of mice		2	2	

**(Top)** Quantification of the numbers of properties of spontaneous excitatory post-synaptic currents (sEPSCs) of fast-spiking (FS) and regular-spiking (RS) CINs in Control, *Mafb* cKO, *c-Maf* cKO and cDKO. One Way ANOVA Kruskal-Wallis followed by Dunn's multiple comparisons test was used for the analysis. **(Bottom)** Quantification of the numbers of properties of mEPSCs of layer V CINs for Control and *Mafb* cKO. Mann-Whitney test was used for the analysis. Data are expressed as the mean  $\pm$  SEM. \*p < 0.05, \*\*p < 0.01, \*\*\*p < 0.001, \*\*\*\*p < 0.0001.

**Table S5. Statistical analysis for local field potential measurement by layers**

Genotypes	From Figure 8D					
	Line length p values			Amplitude p values		
	Layer ii-iii	Layer iv	Layer v-vi	Layer ii-iii	Layer iv	Layer v-vi
Control vs. <i>Mafb</i> cKO	< 0.0001	< 0.0001	< 0.0001	< 0.0001	< 0.0001	< 0.0001
Control vs. <i>c-Maf</i> cKO	0.006	0.02	< 0.0001	< 0.0001	< 0.0001	< 0.0001
Control vs. cDKO	0.0006	0.03	< 0.0001	< 0.0001	< 0.0001	< 0.0001
<i>Mafb</i> cKO vs. cDKO	< 0.0001	< 0.0001	< 0.0001	< 0.0001	< 0.0001	< 0.0001
<i>Mafb</i> cKO vs. <i>c-Maf</i> cKO	< 0.0001	< 0.0001	< 0.0001	< 0.0001	< 0.0001	< 0.0001
<i>c-Maf</i> cKO vs. cDKO	n.s.	0.0006	< 0.0001	< 0.0001	< 0.0001	< 0.0001

Genotypes	From Figure 8E					
	Line length p values			Amplitude p values		
	Layer ii-iii	Layer iv	Layer v-vi	Layer ii-iii	Layer iv	Layer v-vi
Control vs. <i>Mafb</i> cKO	< 0.0001	< 0.0001	< 0.0001	< 0.0001	< 0.0001	< 0.0001
Control vs. <i>c-Maf</i> cKO	n.s.	n.s.	0.02	n.s.	n.s.	n.s.
Control vs. cDKO	n.s.	n.s.	n.s.	n.s.	n.s.	n.s.
<i>Mafb</i> cKO vs. cDKO	< 0.0001	< 0.0001	n.s.	< 0.0001	0.001	< 0.0001
<i>Mafb</i> cKO vs. <i>c-Maf</i> cKO	< 0.0001	< 0.0001	0.03	< 0.0001	< 0.0001	0.01
<i>c-Maf</i> cKO vs. cDKO	n.s.	n.s.	n.s.	n.s.	n.s.	n.s.

Statistical analysis results for the local field potential/ current source density measurement by layers. Data presented here are p-values.

**Table S6. Genotype information regarding the mice used for each analysis**

Figure(s)	Genotype information			
	Control	<i>Mafb</i> cKO	<i>c-Maf</i> cKO	cDKO
Fig. 1 and Fig. S3	WTs	Pure <i>Mafb</i> cKOs	Pure <i>c-Maf</i> cKOs	n.a
Fig. 2 Neocortical analysis	A mixture of WTs and double heterozygous controls	A mixture of pure <i>Mafb</i> cKOs and sensitized <i>Mafb</i> cKOs	<i>c-Maf</i> cKOs	cDKOs
Fig. 3-5, Fig. S4 and S5	A mixture of WTs and double heterozygous controls	n.a	n.a	cDKOs
Fig. 6 synapse analysis, Fig. S2 and S6 morphology analysis	A mixture of WTs and double heterozygous controls	A mixture of pure <i>Mafb</i> cKOs and sensitized <i>Mafb</i> cKOs	A mixture of pure <i>c-Maf</i> cKOs and sensitized <i>c-Mafb</i> cKOs	cDKOs
Fig. 6 and 7 electrophysiology	WTs	Pure <i>Mafb</i> cKOs	Pure <i>c-Maf</i> cKOs	cDKOs
Fig. S1	WTs	Pure <i>Mafb</i> cKO	Pure <i>c-Maf</i> cKO	n.a

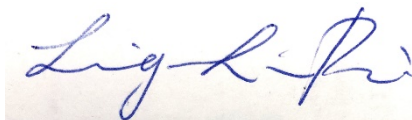
This is a table containing the detailed genotype information for all the animals used for each figure and analysis. Please note that the sensitized single mutants carry a hemizygous allele for the other *Maf* gene.

**Publishing Agreement**

*It is the policy of the University to encourage the distribution of all theses, dissertations, and manuscripts. Copies of all UCSF theses, dissertations, and manuscripts will be routed to the library via the Graduate Division. The library will make all theses, dissertations, and manuscripts accessible to the public and will preserve these to the best of their abilities, in perpetuity.*

***Please sign the following statement:***

*I hereby grant permission to the Graduate Division of the University of California, San Francisco to release copies of my thesis, dissertation, or manuscript to the Campus Library to provide access and preservation, in whole or in part, in perpetuity.*



---

Author Signature

08.12.2019

---

Date